OTTO-VON-GUERICKE-UNIVERSITY OF MAGDEBURG

Construction and Geometric Calibration of A New Robot-Driven Scanning Geometry

Dissertation

zur Erlangung des akademischen Grades

Doktoringenieurin

(Dr.-Ing.)

von Nazila Saeid Nezhad

geb. am 22.04.1987 in Bandarabbas

genehmigt durch die Fakultät für Elektrotechnik und Informationstechnik der Otto-von-Guericke-Universität Magdeburg

Gutachter:

Prof.Dr. Christoph Hoeschen

Prof.Dr. Florian Grüner

Prof.Dr. Martin Skalej

Promotionskolloquium am 21.10.2020

Zusammenfassung

Der zweite Prototyp einer neuentwickelten Roboter-angetriebenen CT-Geometrie "WATCH" (Well Advanced Technique for Comupted Tomography with High Resolution) wurde in einem Röntgen-Strahlungslabor an der Otto-von-Guericke-Universität Magdeburg aufgebaut. Die neue Vorrichtung bietet alle Vorteile der ersten, dritten und vierten Generation des CT-Scanners. In der neuen Geometrie steht die Röntgen-Strahlungsquelle im Zentrum eines 180-Detektorrings. Die Röntgen-Strahlungsquelle dreht sich auf einer Kreisbahn um das Zielobjekt. Der Detektor bewegt sich gleichzeitig und behält seine ursprüngliche Richtung zum Zielobjekt. Die aus dieser Geometrie ermittelten Daten ergeben nicht-abstandsgleiche parallele Strahlen, die für den Rekonstruktionsalgorithmus OPED" (Orthogonal Polynomial Expansion on Disk) Ideal sind.

Der erste Prototyp dieses Systems wurde im Helmholtz-Zentrum in München aufgebaut. Im ersten Modell sind Quelle und Detektor ortsfest und das Objekt bewegt sich um den Mittelpunkt. Im Gegensatz zu erstem Prototyp, ist das Objekt im zweiten Modell ortsfest und das System (Quelle und Detektor) dreht sich mit Hilfe eines KUKA-Roboterarms.Zudem wurde dieses System für die Bildrekonstruktion mit höher Auflösung (durch Anwendung des OPED-Rekonstruktionsalgorithmus verwendet.

Darüber hinaus wurde eine neue Methodik für die geometrische Kalibration des Kegelstrahl-CT in diesem Projekt vorgestellt. Anschließend wurde diese Methode angewandt, um geometrische Parameter für das WATCH-System festzustellen und die Qualität der rekonstruierten Bilder zu verbessern. Außerdem gibt das neue Phantom den Kalibrationspunkt präziser wieder, wodurch die Bestimmung der geometrischen Parameter des Kegelstrahl-CT deutlich verbessert wird.

Schließlich wurde eine Fourier-basierte Methode eingesetzt, um das Auflösungsvermögen des WATCH-Systems zu validieren. Eine Methode zur Bestimmung der vor-gesampleten Modulatiosübertragungsfunktion durch Oversampling der Kantenspreizfunktion wurde angewendet. Die Beurteilung des Rauschverhaltens wurde durch eine Leistungsspektrumanalyse durchgeführt. Aufgrund der variierenden Anzahl von Röntgenphotonen wurde jedoch die Methode der lokalen Leistungsspektrumsanalyse übernommen.

Abstract

The second prototype of a newly developed robot-driven CT geometry, named WATCH (Well Advanced Technique for Computed Tomography with High Resolution), has been constructed in the X-ray laboratory of Magdeburg university. This system offers a potential advantage over the first, third and fourth generations of CT scanners. In the new geometry, an x-ray source is located at the center of a 180-degree detector ring, and the x-ray source rotates around the object in a circular path. The detector arrangement is translated at the same time, but it keeps its initial orientation. The data acquired from this geometry provides non-equally spaced parallel rays which are ideal for the OPED reconstruction algorithm.

The first prototype of this system was constructed at Helmholtz center, Munich. In the first model, the source and the detector system are stationary, and the object moves around the rotation center. In contrary to the first prototype, in the new prototype system, the object is stationary and the source-detector arrangement moves around the object using a KUKA robotic arm. Moreover, this system was used for the high-resolution image reconstruction using the OPED reconstruction algorithm.

Additionally, in this thesis, a novel cone-beam CT geometric calibration method has been developed, and a new calibration phantom has been introduced. This calibration technique was used to determine the geometric parameters of the WATCH system and to improve the quality of reconstructed images. The new phantom more precisely resembles a calibration point which consequently improves the estimation of the geometric parameters in cone-beam CTs.

Finally, a Fourier based method was used to evaluate the image quality of the WATCH system. In this approach, we applied a method of determining the pre-sampled MTF by oversampling the edge spread function. The noise assessment on the reconstructed images was carried out using power spectral analysis, however, due to the variations in detected x-ray photons, a method for determining the local noise power spectrum was adopted.

Contents

List of Figures

List of Tables

Abbreviations

CT	**C**omputed **T**omography
CBCT	**C**one **B**eam **C**omputed **T**omography
WATCH	**W**ell **A**dvanced **T**echnique for **C**T with **H**igh resolution
OPED	**O**rthogonal **P**olynomial **E**xpansion on **D**isk
FBP	**F**iltered **B**ack **P**rojection
EMI	**E**lectrical **M**usical **I**ndustries
SOD	**S**ource **O**bject **D**istance
SDD	**S**ource **D**etector **D**istance
NPS	**N**oise **P**ower **S**pectrum
MTF	**M**odulation **T**ransfer **F**unction
ESF	**E**dge **S**pread **F**unction
FOV	**F**ield **O**f **V**iew
ROI	**R**egion **O**f **I**nterest
IEC	**I**nternational **E**lectronical **C**ommission
OVGU	**O**tto **v**on **G**euricke **U**niversität
PC	**P**ersonal **C**omputer
IQ	**I**mage **Q**uality
IQA	**I**mage **Q**uality **A**ssessment

Dedicated to my beloved parents...

Chapter 1

Introduction

1.1 X-ray Computed Tomography

X-ray imaging technique was discovered more than a century ago by Wilhelm Conrad Roentgen in 1895. Before that time the diagnosis only was possible through invasive procedures which could have high risks for patients. The X-ray was potentially beneficial for non-invasive imaging when it was discovered. Within a month after the discovery of Roentgen, several radiographs were generated in Europe and the United States for medical purposes to guide surgeons in their work. One year after this revolutionary invention, the lack of depth information of the radio-graphs and the need for three-dimensional imaging methods, to precisely localize lesions, was noticed. Therefore, a new scanning technique called computed tomography (CT) was invented in the 1960s, based on the mathematics derived by Radon, which combined many X-ray projections from different angles around the patient to generate a tomographic image by utilizing various image reconstruction algorithms.

CT was first developed in 1967 by Sir Godfrey Hounsfield at Electrical Musical Industries (EMI) research laboratories in the United Kingdom, which was also a record label for the Beatles. Hounsfield and his team determined that results should be presented to a radiologist in the form of a picture that demonstrates three-dimensional representation of the body part under examination. In 1971 Sir Hounsfield and Dr. Ambrose presented the first clinical CT image. A few years later, in 1979 Allan McLeod Cormack and Sir Godfrey Hounsfield were awarded the Nobel Prize in Physiology and Medicine for the invention of CT[Hsi03].

X-ray CT application has tremendously increased in recent years, in terms of both industrial application and medical diagnosis, because of its remarkable properties in high-resolution imaging which have been recognized and developed during the last century.

There are only few adults in industrial countries who have not been exposed to at least one of the imaging procedures at least once in their life. At the simple stage, the radiography is one of these examples.

First generation CT scanners were based on the translation/rotation of the source−detector system. A pencil beam X-ray source and a single detector module were translated in 160 steps in parallel and then, rotated around an object with 1° angle increment. In this way, subsequent sets of parallel data were collected to be used for image reconstruction (see left side of figure 1.1). This procedure took about five minutes for generation of a single slice of a brain which could lead to a severe image artifact such as motion artifact, therefore, in the second generation of CT systems the size of the X-ray beam (3 to 10 degree) and the detector array (linear array of 30 detectors) increased to improve the scanning time (see right side of figure1.1) , however, the scanning system was still based on the translation/rotation of the X-ray source-detector pair, with maximum of 10° increment for each rotation step. This reduced the scanning time to minimum of 18 seconds per slice. The translational motion of the first and second generation was a fundamental impediment to the shorter scan-time, therefore, in the third-generation CT scanners (see left side of figure1.2), a wider fan or cone beam X-ray source moves around the patient body, usually on a circular trajectory, such that the patient is encompassed within the X-ray beam. This consequently allows the collection of fan-beam or parallel-beam geometry data, which can be reconstructed with Filtered backprojection or iterative reconstruction algorithms. [Hsi03]. Different variants of third generation systems have been developed, which include those based on offsetting the centre of rotation and the use of a flying focus X-ray tube to generate images with higher resolution[Bru11].

Fourth-generation CT scanners tried to overcome drawbacks of third generation scanners such as the instability of the detector system, aliasing and ring artifact (see right side of figure1.2). Therefore, they contain a stationary detector ring and the X-ray source rotates on a circular path around the object inside the ring [Hsi03]. This structure increases the size of the detector ring, and unlike the third-generation systems, an anti-scatter grid cannot be used in this generation of scanners. Electron Beam Computed Tomography (EBCT), known as the fifth generation of the CT scanners or ultra−fast scanner, was developed specifically for cardiac imaging and heart structure imaging which never stops moving. Instead of a conventional X-ray tube, it has a large bell-shaped tungsten target which encircles the patient and lies directly opposite to the detector ring. X-rays are emitted from a local focal track, as a high energy electron beam strikes the tungsten target. The generated X-rays travel through the patient chest and are detected by a detector system on the opposite side of the patient. This

generation is expensive, the generated image volume is small and it is specifically used for cardiac imaging.[Hsi03]

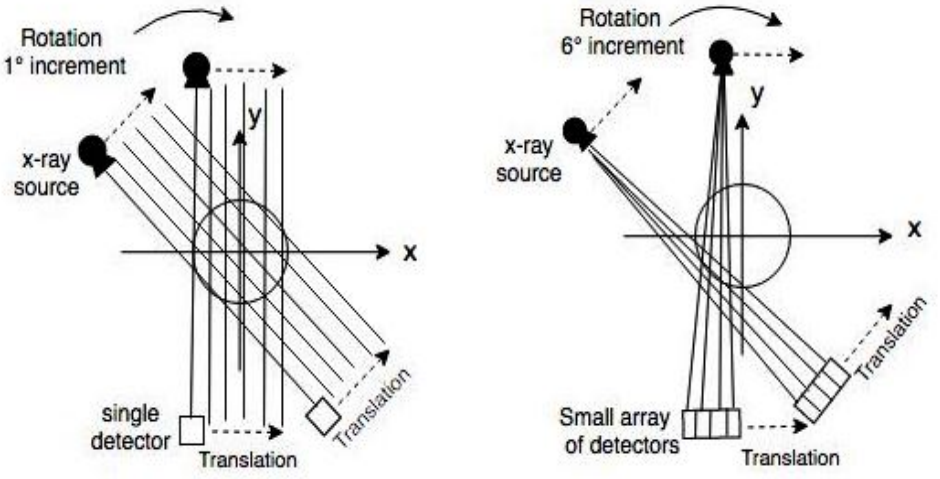

FIGURE 1.1: Left: The first generation CT system. Right: The second generation CT scanner.

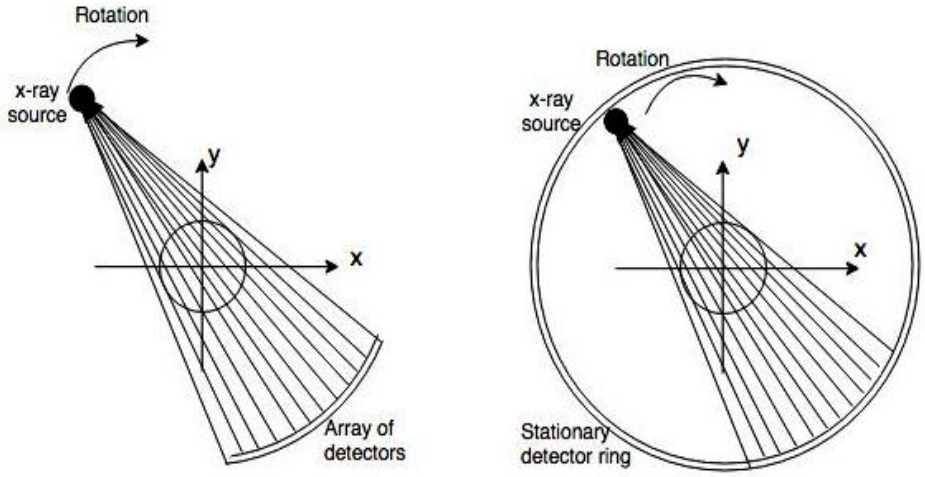

FIGURE 1.2: Left: The third generation CT system. Right: The fourth generation CT scanner.

In the previous works of our group, a new micro scanning system (referred to as WATCH, see figure 1.4), capable of functioning at a lower dose level and a faster reconstruction protocol, has been proposed. This system is capable of collecting parallel X-ray projections from a standard CT source without the requirement of rebinning the tomographic projection data or performing additional interpolation steps.

Radiation exposures related to the diagnostic X-ray examinations have been a primary issue in patient health and safety. The motivation of this work was, therefore, to further develop and calibrate a new CT system that can potentially reduce the X-ray dose for

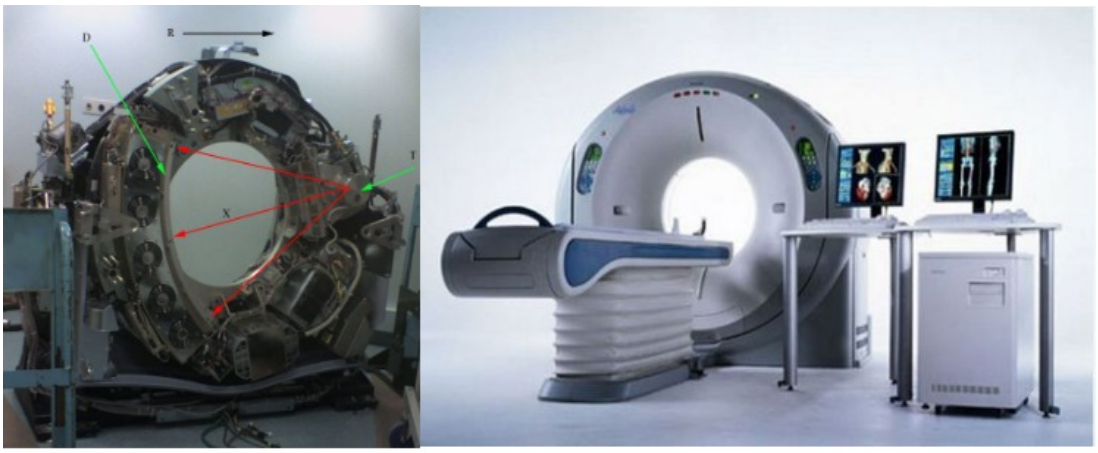

FIGURE 1.3: Modern CT scanner [Wik19]

the same or better image quality. In previous works of our group [KST+13] [TSXH10] [dH08], a new micro scanning system capable of functioning at a lower dose level and a faster reconstruction protocol, referred to as Well Advanced Technique for CT with High Resolution (WATCH) (see figure 1.4), has been proposed that is capable of collecting parallel projections from a standard X-ray source without the requirement to conduct the process of interpolation or rebinning the tomographic projection data. The acquired data are natural for a reconstruction algorithm, referred to as Orthogonal Polynomial Expansion on Disk (OPED) (see section 2.2) [XTH07b][XTH07a]. This system was designed to be a half ring detector array and an X-ray tube placed at the center of the detector arc. The X-ray source moves around the object on a circular trajectory, and the detector ring simultaneously translates with the motion of the X-ray tube, preserving its initial orientation. The unequally-spaced parallel data is then collected and reconstructed ideally using the OPED reconstruction algorithm.

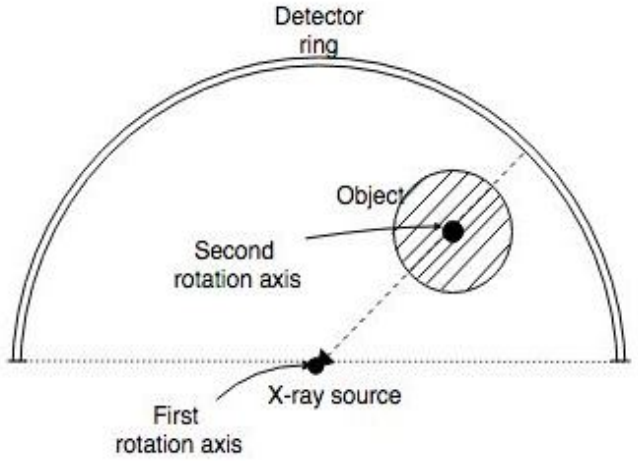

FIGURE 1.4: Schematic of WATCH-CT geometry

1.2 Aim of the Project

The application of CT imaging is growing exceedingly and, therefore, the requirements for dose reduction is becoming increasingly important. Patient exposure in CT imaging can be managed through hardware and software optimizations, however, these approaches are often limited by their cost-effectiveness and technical feasibility. Nevertheless, some novel techniques open up the possibilities to potentially overcome this problem. The WATCH-CT system proposes a new scanning geometry which in conjunction with a new image reconstruction algorithm OPED (Orthogonal Polynomial Expansion on Disk) (see section 2.2) [TSXH10] [KST+13] could potentially reduce the patient exposure for the same image quality.

For higher achievable image quality, it is crucial to know the position of the focus spot and the detector assembly with respect to the system rotation axes. The purpose of this work is to describe a new method for the geometric calibration of WATCH-CT scanner, which is also applicable for calibration of flat-panel CBCT systems. The discussion is limited to the typical case where the cone vertex and planar detector move along a circular trajectory relative to the object. Moreover, it is assumed that the area detector does not have spatial distortions. The accuracy of this method is validated by utilizing Geant4 toolkit based on the Monte-Carlo simulation [GAea03]. The formulation applied in this methodology is similar to that one used by Mennessier et. al. [MCN09]. In their study, geometric parameters such as source position and the detector orientation are determined in the a so-called laboratory reference frame which is fixed based on the phantom i.e. a point of the phantom is the center of the reference frame. In contrary to their technique, in our method the values of all geometric parameters are determined in the system reference frame. Only two projection angles of a simple calibration phantom are required to fully define the scanner geometry [TNH19]. Furthermore, the second prototype of the WATCH-CT was constructed in the X-ray laboratory of Otto-von-Guericke University of Magdeburg. This system was also employed to implement the new calibration technique experimentally and investigate the methodology.

Additionally, most of the methods track a phantom embedded with one or more pellets [NCM+00] [MCN09] [YKMB06], then, they extract the features of the pellet projections using computer vision methods. These features are then employed to solve the optimization problems or non-linear equations to determine the gross geometry parameters. Some studies [YKMB06] try to establish the center of the ball by calculating the mass center of the grey value of the ball projection. The problem with high-density balls, as calibration phantoms, is the complexity in the identification of the ball center due to the inhomogeneity within the ball shadow. Moreover, the shadow of a ball or a pellet is an ellipse, and the center of the ball may not lie on the center of the ellipse nor on its

focus. Additionally, there is a question concerning the size of the ball phantom, with a larger radius, the analysis of the gray value within the ball as well as its shadow becomes increasingly complicated, and if it is exceedingly small, the number of the pixels within the shadow is not sufficient for the determination of its center. [TnH17]. In this research, we propose a new calibration phantom which could be used as a calibration point in the estimation of the geometric parameters. A high-density cone phantom, which enables the utilization of the apex from its projections. The advantage of this phantom is that it can be easily constructed and the likelihood of overlapping points decreases [TnH17]. The properties of the new phantom are discussed in detail in section 3.2.4.

The organization of the thesis is as follows: in chapter 2, we define the geometric calibration parameters of the WATCH-CT and the CBCT; and discuss the principle of geometric calibration methods. In Chapter 3, we describe the simulation and experimental setup for validation of our method. Additionally, the mathematical expressions of the new calibration method are described. Chapter 4 illustrates the data treatment process required to convert the acquired data into an image using the second prototype of the WATCH-CT. In chapter 5, we present the results that have been obtained from the simulation and experimental data of the WATCH-CT scanner. Finally, some theoretical improvement and future perspectives are discussed, with conclusions in chapter 6.

Chapter 2

Theoretical Background

This chapter describes the experimental and simulation part of the work. It illustrates in detail the construction of a prototype of WATCH system. Moreover, the calibration procedure and investigations are explained in detail. The new calibration method of the WATCH-CT and the simulation study which were used to verify the method are described in this chapter.

2.1 WATCH Geometry Parameterization

The isocenter is a point through which the central ray of the radiation beam passes. In conventional computed tomography, the isocenter typically coincides with the mechanical center of the rotation plane i.e. point O in figure 2.1.

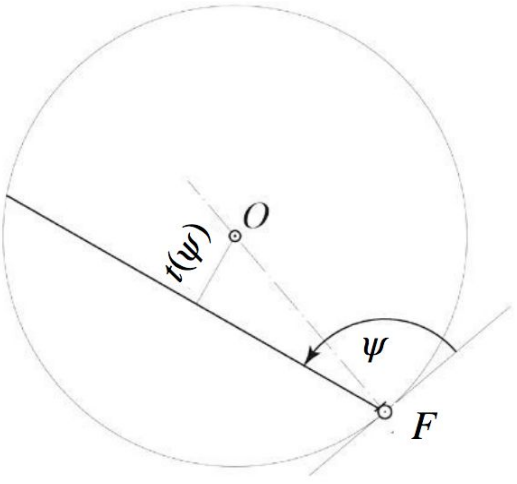

FIGURE 2.1: Rotation of the X-ray source around the isocenter O. F is the X-ray source.

Here, it is considered that the X-ray source F rotates anti-clockwise around the isocenter O , and rays produced by the source are described by the angle ψ as shown in figure 2.1. The radius of the source trajectory is assumed to be 1. Then,

$$t(\psi) = cos\psi \tag{2.1}$$

is the signed distance between the ray ψ and the isocenter. In practice, a ray is defined by a line connecting the source and the detector. In conventional computed tomography, the angle ψ of a given ray i.e. the ray associated with the detector, remains constant during the scanning process.

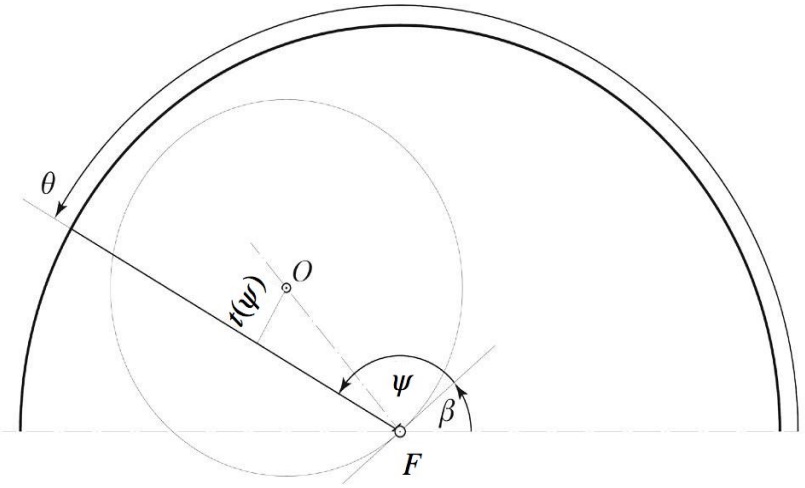

FIGURE 2.2: Idealized scheme of the WATCH Parameters

One distinguishing feature of the WATCH system is that the angle ψ of the ray varies during the scanning. We know that any detector of the WATCH system can be described by the angle θ which is fixed and relates to the angle ψ via:

$$\theta = \psi + \beta \tag{2.2}$$

(see figure 2.2). Values of β are obtained from characteristics of the system such as the frame rate of the detector and the source rotation speed.Therefore, the angle β is assumed to be known. Let:

$$\beta_k = \beta_0 + k\Delta\beta \tag{2.3}$$

where β_k is the value of β at the moment of k-th read-out, that is, $\beta_k = \beta(T_k)$. Substituting equation 2.2 into equation 2.1 yields:

$$\psi_k(\theta) = \theta - \beta_k \tag{2.4}$$

Where the value $\psi_k(\theta)$ depends on both the value of θ and the index k , which points to a moment of read-out, not to a position of the ray!

By considering the idealized WATCH system shown in figure 2.1 and assuming that all detectors (denoted by N) are uniformly distributed on the half circle (bold line), with the help of a single detector θ_v, the system collects the data:

$$R_{v,k} = R(\phi_v, t_{v,k}) \tag{2.5}$$

Which is the Radon transform [XTH07b], ϕ is the projection angle and $t_{v,k}$ is the signed distance between the ray and the isocenter. The index v in equation 2.5 is the index of a detector, and the index k indicates the read-out moment. Moreover, we set $\phi = \theta$ and rewrite equation 2.5 in the form:

$$R_{v,k} = R(\theta_v, cos\psi_{v,k}) \tag{2.6}$$

where,

$$cos\psi_{v,k} = cos(\theta_v - \beta_0 - k\Delta\beta) = cos(\psi_{v,0} + k\Delta\beta) \tag{2.7}$$

with,

$$\psi_{v,0} = \beta_0 - \theta_v. \tag{2.8}$$

Due to the uniform distribution of the detectors on the arc of the size π , $\theta_v = v(\tau\Delta\beta)$, where τ is some arbitrary positive rational number, so that $\theta_0 = 0$ and $\theta_{N-1} = \pi - \tau\Delta\beta$. To simplify the situation we also set the conditions $\beta_0 = 0$ and $\theta_v = v\Delta\theta$ where, $\Delta\theta = n\Delta\beta$.

Under above conditions

$$\psi_k(\theta_v) = (k - vn)\beta \tag{2.9}$$

is valid.

Let the measured data be written into the matrix of the size $N \times M$, where N is the number of detectors and M is the number of read-outs. Due to equation 2.9 the structure of the matrix will be similar to that shown in figure 2.3.

FIGURE 2.3: Matrix of non-equally spaced parallel rays before shifting.

This matrix is not suitable for the input in the reconstruction algorithm. The lines of the matrix must be appropriately shifted. Therefore if $\beta_0 = 0$ we leave the line $R_0 := \{R_{0,k}|k = 0, ..., M - 1\}$ as it is, all other lines have to be shifted. The shift s_v for the line v is determined from the condition $\psi_{k+s}(\theta_v) = \psi_k(\theta_0)$.
Using equation 2.9, one can obtain:

$$s_v = vn. \tag{2.10}$$

As a result the matrix R is transformed to the matrix shown in figure 2.4 which is the input for the OPED reconstruction algorithm (see section 2.2) and it has the geometry illustrated as follows.

Formally, a ray $l(\theta, t)$ is a line described by equation $xcos\theta + ysin\theta = t$, in other words:

$$l(\theta, t) : \big\{(x, y)|xcos\theta + ysin\theta = t\big\}. \tag{2.11}$$

FIGURE 2.4: Matrix of non-equally spaced parallel rays after shifting.

Where the angle θ is referred to as a projection angle of the ray, and t is the signed distance between the line and the origin of the coordinate system xy (see the left side of figure 2.5).

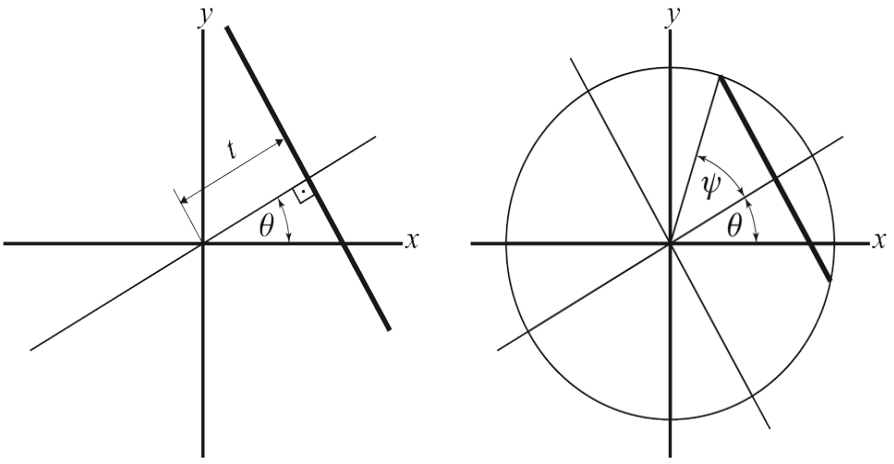

FIGURE 2.5: Two equivalent representations of the same ray (fat line).

The same line can equivalently be described by the angle parameter ψ (see the right side of figure 2.5). Therefore, the relation $t = cos\psi$ is valid.

In tomography, one collects the data in the form of integrals over a discrete set of lines. The configuration of lines is referred to as the data geometry. The data geometry where the set of all lines is represented by the groups of parallel lines is called parallel beam geometry. There are two interesting kinds of the parallel beam geometry:

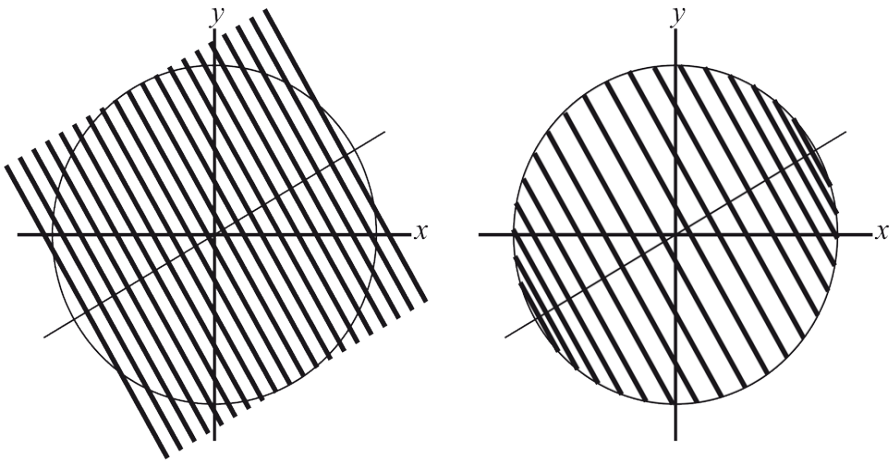

FIGURE 2.6: Left: equispaced rays; right: non-equispaced rays

1) parallel lines are described by t_j,

$$t_j = t_0 + j\frac{R}{M}, j = -M, ..., M \tag{2.12}$$

2) parallel lines are described by the angle parameter ψ_j,

$$\psi_j = \psi_0 + j\frac{\pi}{M}, j = 0, ..., M-1 \tag{2.13}$$

Corresponding distributions of rays are depicted in the left and right sides of figure 2.6 respectively.

The first kind of parallel data is natural for the reconstruction using the FBP algorithm, while the second kind is natural for reconstruction using the OPED algorithm. More information about the FBP algorithm could be found in [Hsi03]. The OPED algorithm is briefly described in the next section.

2.2 OPED Reconstruction Algorithm

In previous work of our group, a reconstruction algorithm called OPED, based on the Orthogonal Polynomial Expansion on a Disc, was introduced. Y. Xu et al.[XTH07b] proposed an advanced form of reconstruction algorithm that requires non-equally spaced parallel projection data (see figure 2.6), in contrary to the equally-distanced parallel data (see figure 2.6) which is suitable for FBP reconstruction algorithm. The OPED algorithm is based on a geometry in which parallel rays follow the distribution of the zeros of Chebyshev polynomials of a given order [XTH07b][dH08]. The parallel rays are

uniformly distributed over the boundary of a disk, represent an example of data which can be re-sampled to fan data and vice versa without loss of information. One of the specific requirements for the reconstruction algorithm OPED is that Radon projections have to be ψ-projections (see section 2.1). This means that fan data can be re-sampled to data required by OPED via some loss-free interpolation. The reconstruction of such data can be performed directly, without any modification of original data. In O. Tischenko et al. [TSXH10] the projections of this geometry are referred to as ψ-projections, and the corresponding parameterization as ψ-parameterization. The algorithm OPED consists of approximating the function $f(x, y)$ that we want to reconstruct as an expansion A_N in N Chebyshev Polynomials U_k of order k = 0,. . . ,N-1 [XTH07b]. The approximation of function $f(x, y)$ can be given as,

$$A_N f(x,y) = \underbrace{\frac{1}{N}}_{1} \sum_{v=0}^{N-1} \sum_{k=0}^{N-1} \underbrace{(k+1)}_{2} \underbrace{U_k(xcos\theta_v + ysin\theta_v)}_{3} \underbrace{\frac{1}{\pi} \int_{-1}^{1} R_f(\theta_v, t) U_k(t) dt}_{4} \tag{2.14}$$

Where, the first part (1) is a normalization factor, the term (2) are weights for the corresponding components in the expansion. The third part (3) is the corresponding basis vector, i.e. a Chebyshev ridge polynomial of the second kind and the part (4) is the corresponding coefficient of the expansion in the basis of the space of polynomials if order less of equal to $N-1$, i.e. the scalar product of the Radon projection $R_f(\cdot, t)$ and the basis vectors $U_k(t)$. The best possible approximation of this integral is provided by the Gaussian quadrature [dH08] [SkKM+18].

In the following paragraph there is a part of the theoretical background that is essential for understanding the OPED-algorithm.

Let function f be defined within the unit disk D, $D := \{(x, y)|x^2 + y^2 \leqslant 1\}$ where, $f(x, y) = 0$ if $(x, y) \notin D$. Then the Radon transform of function f is:

$$R_f(\theta, t) = \int_{D \cap l(\theta,t)} f(x, y) dx dy \tag{2.15}$$

If $R_f(\theta, t)$ is known for all θ then the basic OPED inversion formula is:

$$f(x,y) = \frac{1}{2} \sum_{k=0}^{\infty} (k+1) \int_0^{2\pi} c_k(\theta) U_k(xcos\theta + ysin\theta) d\theta \tag{2.16}$$

where,

$$c_k(\theta) = \frac{1}{\pi}\int_{-1}^{1} R_f(\theta,t)U_k(t)dt \tag{2.17}$$

and

$$U_k(t) = \frac{sin((k+1)\psi)}{sin\psi}, t = cos\psi \tag{2.18}$$

is the Chebyshev polynomial of the second kind. Using the property $R_f(\theta+\pi,t) = R_f(\theta,-t)$, the formula 2.16 can be rewritten in the form of:

$$f(x,y) = \sum_{k=0}^{\infty}(k+1)\int_0^{\pi} c_k(\theta)U_k(xcos\theta + ysin\theta)d\theta \tag{2.19}$$

Truncation of the series in equation 2.19 up to the index M yields the formula:

$$Af(x,y) = \sum_{k=0}^{M-1}(k+1)\int_0^{\pi} c_k(\theta)U_k(xcos\theta + ysin\theta)d\theta \tag{2.20}$$

Where Af is the approximation of f.

Let $t = cos\psi$ then,

$$c_k(\theta) = \frac{1}{\pi}\int_0^{\pi} p(\theta,\psi)sin((1+k)\psi)d\psi \tag{2.21}$$

where,

$$p(\theta,\psi) = R(\theta,cos\psi) \tag{2.22}$$

Recall that in the practice the Radon transform can be measured over the discrete set of lines only. Let available samples of the Radon transform be:

$$p_{v,j} = p(\theta_v,\psi_j) \tag{2.23}$$

where,

$$\theta_v = \frac{v\pi}{N}, \qquad v = 0,...,N-1 \tag{2.24}$$

$$\psi_j = \psi_0 + \frac{j\pi}{M}, \qquad j = 0, ..., M-1 \tag{2.25}$$

Replacing integrals in equations 2.17 and 2.20 by corresponding quadrature formulae, one obtains:

$$c_k(\theta) = \frac{1}{M} \sum_{k=0}^{M-1} p(\theta_v, \psi_j) sin((1+k)\psi_j) \tag{2.26}$$

and

$$Af_N(x,y) = \frac{1}{NM} \sum_{v=0}^{N-1} \sum_{j=0}^{M-1} p_{v,j} \Theta_j(xcos\theta_v + ysin\theta_v) \tag{2.27}$$

where,

$$\Theta_j(s) = \sum_{k=0}^{M-1} (k+1) sin((k+1)\psi_j) U_k(s) \tag{2.28}$$

The formula 2.27 can be used for reconstruction of the data defined in equations 2.24 and 2.25.

2.3 Flat-Panel CBCT Geometric Calibration

Generally, a flat-panel CBCT consists of an X-ray source and a detector system rotating around a rotation axis, in this case, on a circular path. In practice, for geometrically accurate reconstruction of CT images, it is crucial to correctly associate the collected data with rays and it is possible only if the position of the focus spot and the detector with respect to the rotation axis is known, generally known as gross geometry calibration. Different studies [KTE+01] [SHZH06] investigated the effect of the misalignment of the source and the detector on the reconstructed image. On the other hand, for polygonal or multi-channel detector a more detailed knowledge of the system such as the gap between channels and pixels, is required, common as fine geometry calibration [Hol09].

There have been many investigations in the field of gross geometry calibration for fan-beam [JLG+15], [GTCE87] and cone-beam [NCM+00] [CMSJ05] [PBGM08] [MCN09] [BNB+03] CT systems. For calibration of the fan-beam CT system, five geometric parameters need to be established. These parameters are sought: two for the position

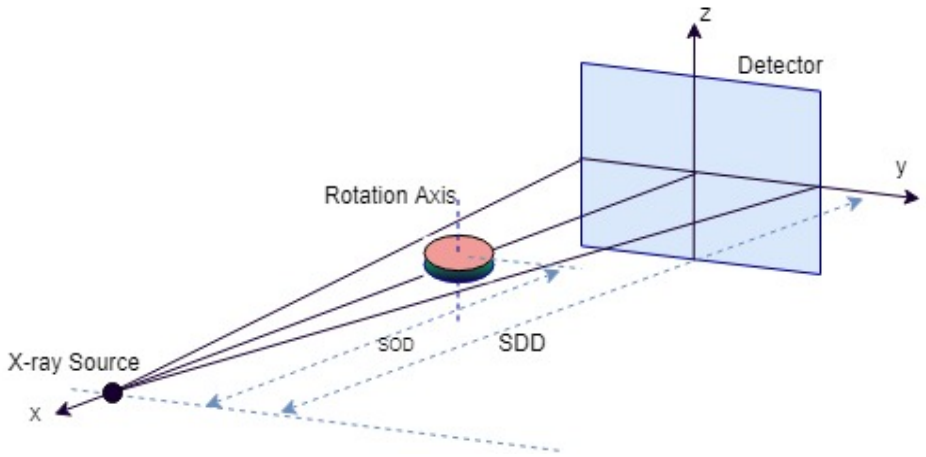

FIGURE 2.7: Geometric parameters in CBCT.

of the focus spot or fan vertex, one for the detector tilt and two for the detector shift. Among them, the most important parameter, which influences the image quality, is the distance between the projection of the iso-center and the center of the detector array, i.e. the transversal shift of the detector [PBGM08]. Similarly, for calibration of a CBCT, nine geometric parameters are established. Three parameters for the location of the detector, three parameters for orientation of the detector, and three parameters for the location of the X-ray focus. [MCN09]. In the case of a circular trajectory of the X-ray source and the detector, due to the freedom of choice for the origin of the z-axis and the gantry angle, two of these parameters are removed. Therefore, a complete geometry of the scanner system can be defined using seven parameters [PBGM08] [BNB+03].

The proposed techniques for geometric calibration are mainly based on the optimization procedures [PBGM08] [MGY13] [FZ14] [BNB+03] [DVN08], or they are analytical methods [NCM+00] [CMSJ05] [FZW11] [Bro99] [MCN09]. Most of the optimization methods are generally carried out in three steps. The first step is measuring the projection coordinates (v,w) of a point object on the detector reference system for N number of positions of the X-ray source. In the second step, the analytical expressions for the projections coordinates ($\tilde{v}_i$,$\tilde{w}_i$) are a set of non-linear equations, where the unknown geometric parameters and unknown position of the point-like object are the solution for these equations. This could be expressed as follows:

$$\begin{cases} v_i(unknowns) = \tilde{v}_i & i = 1, ..., N \\ w_i(unknowns) = \tilde{w}_i \end{cases} \tag{2.29}$$

Where, on the right-hand side are the coordinates of the projected calibration points in the reference system of the detector. Finally, these equations are solved using a least-squares based iterative method such as the Levenberg-Marquard algorithm.[NCM+00]

A drawback of the optimization techniques is that they rely on a highly non-linear parameter estimation equations, as described by the functions above. This formalism presents the numerical difficulties of non-linear optimization routines: the requirement for numerical software packages such as optimization tools [MCN09], proper initial estimates, and the possible need to carefully choose the sequence of parameters to optimize. In addition, there are problems of stability and uniqueness of the solutions. [NCM+00]

Jiang et. al. [JLG+15] proposed a method based on the optimization technique for calibration of fan-beam CT using a thin wire as the calibration phantom, and calculated only the most important parameter.Also, they claim the technique can be simply extended to all the geometric parameters for fan-beam or CBCT scanner. Moreover, they have compared their result with the analytic work done by Noo et. al. [NCM+00].

D. Panetta, et. al. [PBGM08] proposed an optimization-based geometric calibration technique which is nearly independent of the phantom. They were able to measure four out of seven geometric parameters for CBCT system with a circular trajectory. The parameters such as longitudinal shift, detector tilt, and the source to detector distance are kept fixed due to their negligible effect on the quality of the reconstructed image. In their study, they define a cost function dependant on the geometric parameters by analyzing the redundancy in the projections. A trade-off between the computational cost and the calibration accuracy must be considered when choosing the data subset for the computation of the cost function.

Analytical expressions are a more sophisticated way to determine some [YKMB06] or all [ZHZH15] [MCN09] of the geometric parameters. The analytical methods proposed by them are usually based on the analysis of the dedicated phantoms, composed of a specific number of point-like objects, therefore, the precise knowledge of the shape, and the position of the phantom could be necessary. Noo et. al. [NCM+00] have proposed an analytical method which provides exact results for the geometric parameters provided the location of projections are exactly known, and the number of the projections is greater than five. Their methodology is based on the calculation of the parameters of ellipses. Two ellipses are generated using projections of two ball bearings at the top and bottom of the phantom at different angles of the gantry. The analytic expressions relate the nine unknown geometric parameters to the ten known ellipse parameters. This method was shown to be robust and easy to implement. However, it is not a completely generalized method, since it is assumed that the detector is parallel to the rotation axis of the scanner.

Jintao Zhao et. al. [ZHZH15] proposed an iterative method for the geometric calibration of CB micro-CT and determined most of the calibration parameters with high accuracy, i.e. a value close to the pixel size, except for the source-detector distance, which had

a significant deviation from the true value. Their methodology requires mechanical adjustment after each iteration until the detector tilt and slant are less than 0.05 degree.

Chapter 3

Methods and Materials

This chapter describes the experimental and the simulation part of the work. It illustrates the construction of a prototype of the WATCH system in detail. Moreover, the new geometric calibration method which was developed by us and simulation and experimental studies used to verify the method, are described in this chapter. Finally, the geometric calibration protocol of the WATCH system using our method is given.

3.1 WATCH-CT system Construction

One main purpose of this work is to construct the second prototype of the WATCH system which is mounted on a KUKA robotic arm in the X-ray laboratory of Magdeburg University. The first prototype was constructed in the Helmholtz center of Munich (see right side of figure 3.1) where the X-ray source and the detector arc were stationary and the object moved around the rotation axis. In the first prototype, line detectors were used which enabled two dimensional imaging. In contrary to that, in the second model the object is stationary and the X-ray source and the detector arc are moving around the object on a circular path using a KUKA robotic arm (see left side of figure 3.1). In the following sections, different software and hardware parts of this system are described.

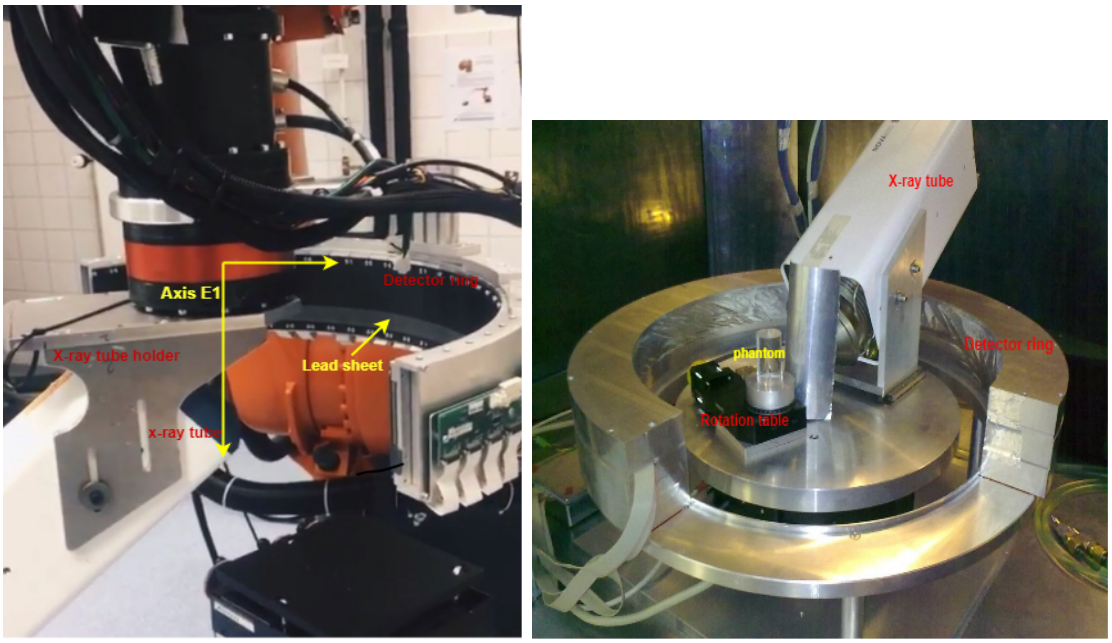

FIGURE 3.1: Left: the second prototype of the WATCH-CT constructed and mounted on a KUKA robotic arm at Magdeburg university. Right: the first prototype of the WATCH-CT constructed in Helmholtz center of Munich.

3.1.1 Experimental Setup Design

The constructed device is a small prototype of the WATCH geometry suitable for a phantom and a dead small animal investigation but not applicable for patient scanning. A water-cooled micro-focus X-ray source was purchased from Oxford instruments as specified in the following sections. The X-ray detector modules were provided by RSF system. In construction of this system 32 detector modules were placed on a half ring with 255 mm inner radius, all looking to the center of the ring where the X-ray source was located (see figure 3.2). The sensor modules were place with a spacing of approximately 0.25°. The sensors cover a half a ring with a size of approximately 182°.

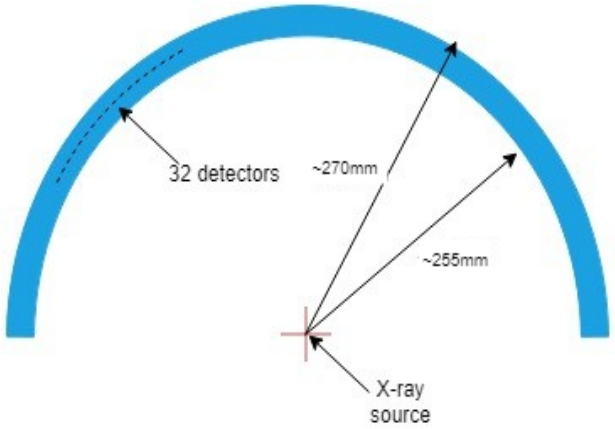

FIGURE 3.2: Scheme of the second prototype of the WATCH system.

3.1.2 The X-ray Tube Hardware

The Nova micro-focus system 96000 series was purchased from Oxford Instrument company in USA. The Micro-focus system has a maximum voltage, power and current of 90kV, 80W and 2.0 mA respectively. It is a water-cooled X-ray source designed for applications where high power, high magnification and small spot size are important. An external high voltage with a smart Controller provides control of the variable voltage and power. The Nova X-ray source delivers exceptional image quality while full control of Brightness is possible. The X-ray micro-focus spot size is continuously adjustable from 14μm to 20μm.[OI19] The information about the applied parameters in our experimental tasks are given in table 3.1.

The standard material of anode target is comprised of Tungsten, however a molybdenum target is also available. The target and the exit window are inclined at an angle of 15 and 30 degrees, respectively, with respect to the electron beam (see bottom of figure 3.3), so that a round X-ray focus spot is projected through the exit window.[OI19]

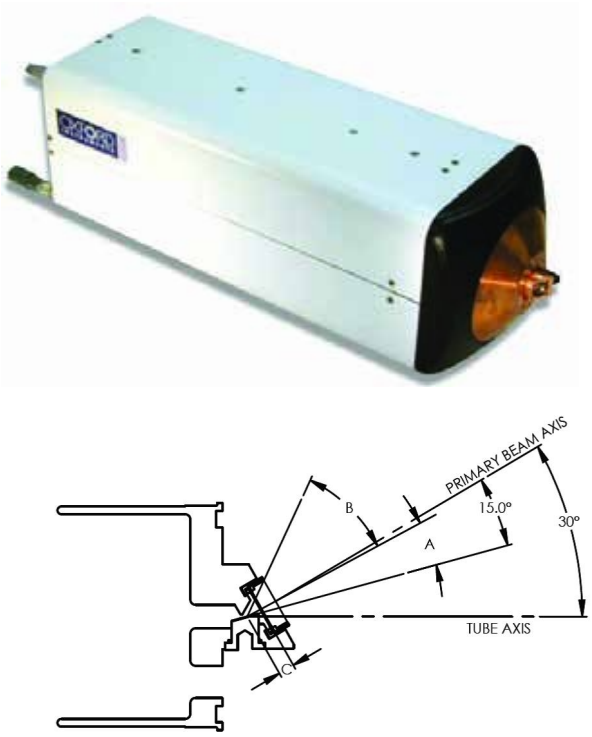

FIGURE 3.3: top: Nova 96000 water-cooled X-ray source.Bottom: the target and the exit window angle[OI19]

3.1.3 X-ray Tube Software

The controlling software runs under LabView RT and MS-Windows. The software package provides remote control of the various functions, such as kV, mA, Brightness, power etc. at the workstation, i.e. outside of the X-ray room. The software is capable of displaying errors produced in the tube functionality. It also includes an RS232 Communication package and an RT version of National Instruments LabView.[OI19]

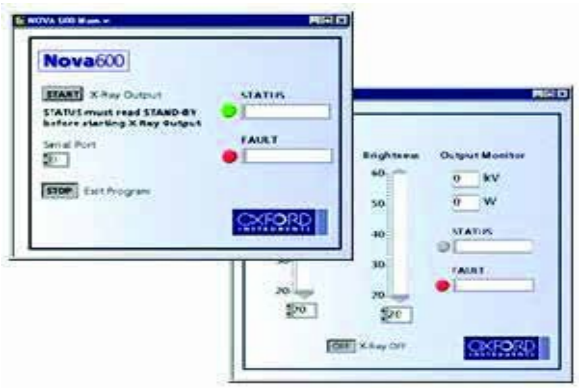

FIGURE 3.4: The X-ray tube software user interface[OI19]

3.1.4 Detector Modules

Four Rad-Eye1 sensors are connected to each other (see the left side of figure 3.5). Eight groups of four Rad-Eye1 detector modules are placed on a half ring detector holder (see figure 3.6), in total thus 32 detector modules. This design were specifically ordered and constructed for the WATCH system.

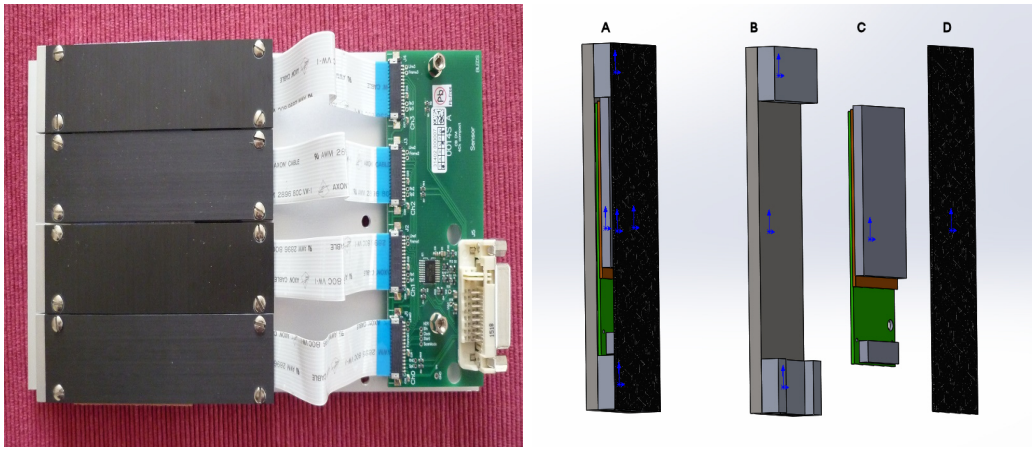

FIGURE 3.5: Left: one set of four Radeye1 connected to the electronic board. Right: schematic of different layers of each detector module

As indicated in figure 3.5 a Rad-Eye1 comprises several layers such as a holder (see the right side of figure 3.5, B) to hold different parts of the sensor from one side and also

to be mounted on the half ring holder (see figure 3.8) from the other side, an electronic circuit (see green plate in the right side of figure 3.5,C) to support the power for photo-diode arrays. A large 24.6 mm by 49.2 mm active area consists of a 512 by 1024 matrix of silicon photo-diodes (see gray plate in the right side of figure 3.5, C) is used to detect visible light, or with a scintillator to detect the X-ray radiations. Also, a carbon fiber (in the right side of the figure 3.5, D) is added to hold the other layers together. This sensor has a standard grade which means it provides the maximum of three defected lines (see Appendix B.4). Additionally, detectors have a variable frame rate from 0.01 to 4.5 Hz. [Dal]

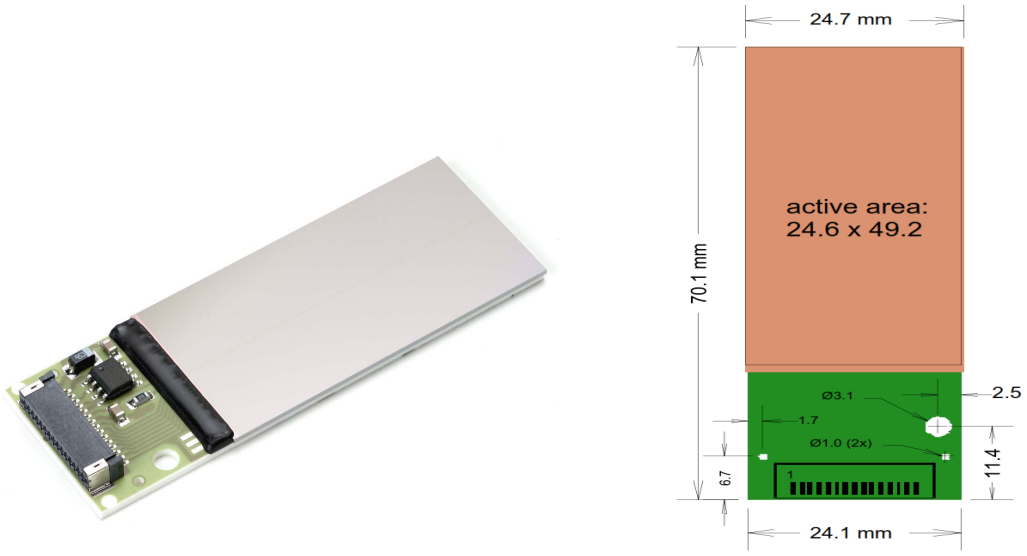

FIGURE 3.6: One Radeye1 and its dimensions.[Dal]

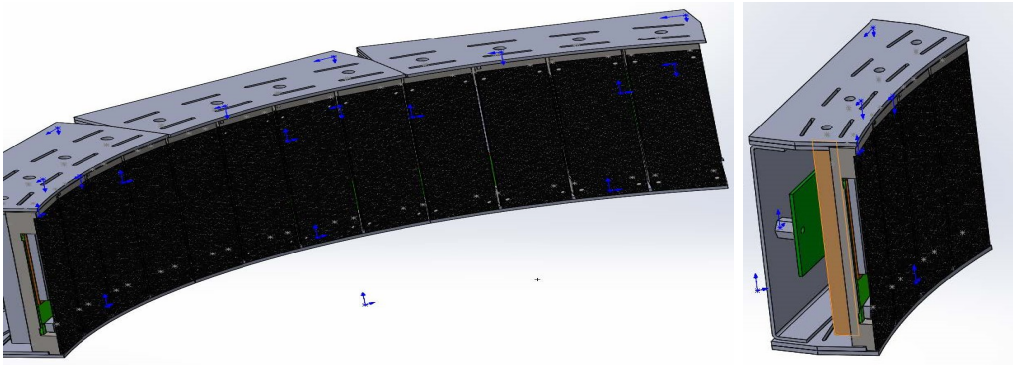

FIGURE 3.7: The WATCH-CT detector house design [Dal]

3.1.5 Detectors Holders

Eight sets of four holders were constructed in the workshop of our faculty in Magdeburg university, as illustrated in figure 3.8. The size of the holder was determined based on the size of the detector itself (see appendix B). Another aluminum plate was constructed to hold the electronic board (see figure 3.8). This board was then placed behind the detector holder (see figure 3.1) to prevent the board from receiving the X-ray radiation which could damage the electronic parts. The small electronic board of the detector was also covered using thin layer of lead to prevent it from the X-ray radiation (see figure 3.1).

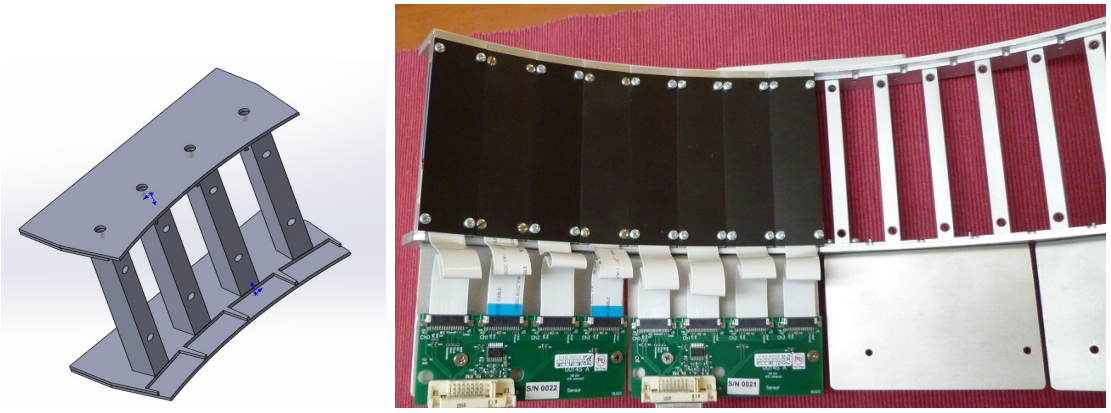

FIGURE 3.8: The WATCH-CT detector holder

3.1.6 The KUKA Robotic Arm

Different parts of the WATCH-CT i.e. the detectors and the X-ray source were mounted on a robotic arm. The robotic arm was provided by KUKA. The system has four different coordinate systems (see the right side of figure 3.9) defined for the implementation of different paths. These coordinate systems are World, Robot, Base and Tool coordinate systems. There are six different axes, named as A1,..,A6, on this robot to implement different movements (see the left side of figure 3.9) [KR05]. For our application an external axis also was connected to axis A6 known as E1 axis (see the left side of figure 3.1). In our constructed system, the external axis was responsible for rotation of the X-ray tube. One program was provided [(1)] to implement the geometry of the WATCH-CT. The program was later adjusted to parameters required for our implementation of the WATCH geometry. KUKA robot has its own programming language. At the moment, implementing the WATCH geometry requires a basic to advance level skill of the robot programming depending on the functionality of the system. In order to only

1. By Monika Kammerer in Helmholtz center of Munich

run the WATCH geometry the basic level is sufficient but for changing parameters of the WATCH-CT geometry skills of the advanced level are required.

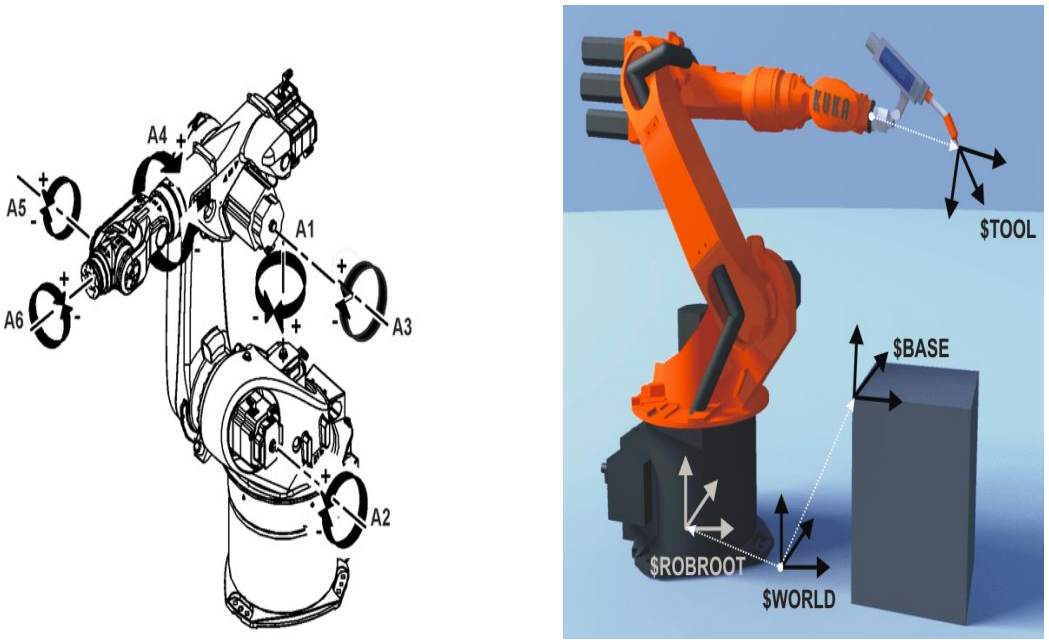

FIGURE 3.9: Left: Six axes of the KUKA robot. Right: Four coordinate systems of the KUKA robot. [KR05]

The conducted robot is a KR 60 HA (High Accuracy). The repeatability of the path and the point position using this system is ±0.06 mm.

The system requires a preparation process before application, known as 'mastering' the robot which is the process of identifying the real geometrical parameters in the kinematic structure of the robot and calibrating the relative position of joint links in the robot. This procedure has to be repeated each time that the robot is moved to a new location or when a different load is mounted on the robot [KR05].

3.1.7 Data Acquisition Hardware

The frame grabber used to collect images from WATCH-CT system is p3i-DIG series frame grabber for digital line-scan and area-scan cameras, which supports EIA-644 (Low-voltage differential signaling) as well as EIA-422 differential input and output signals. A data bus width of 32-bit together with seven differential input and seven differential output signals makes this frame grabber a better solution for use with different data modes and camera specific signals. In order to minimize the risk of data loss the on-board SODIMM (Small-Outline Dual Inline Memory Module) buffers high data rates. This is useful especially in cases the PCI bus is busy or data rate exceeds PCI bus bandwidth [EE03]. There is a connector between the Rad-Eye1 imaging sensors and the

frame grabber, called "shado-box" provided by TELEDYNE together with the detector modules. Each frame grabber supports eight Rad-Eye1 sensors, therefore, four frame grabbers were mounted on a PC to collect frames from all the X-ray detectors.

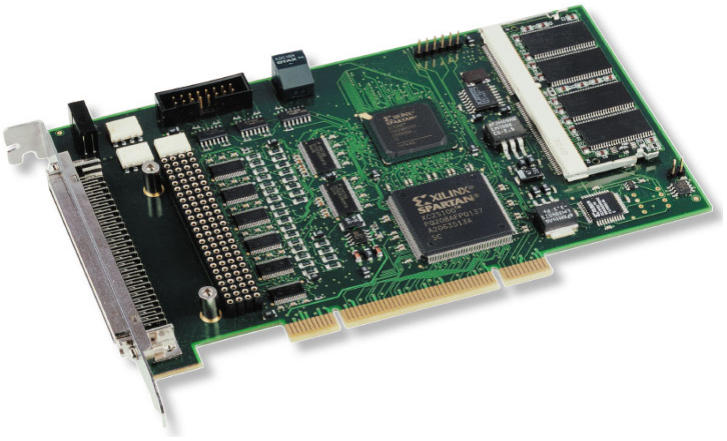

FIGURE 3.10: P3i3 frame grabber board used for collection of the data. [EE03]

3.1.8 Data Acquisition Software

The data from the constructed system were mainly collected by provided software from TELEDYNE , called "shadocam". This software is able to do the offset and gain correction of projections or X-ray images using a gain image and an offset image, respectively. An offset image or dark field is acquired when there is no light or X-rays and the only signal received by the camera is an offset voltage and dark current based signal. This will help correcting small variations in the dark image received from the Shad-o-Box camera. The gain image is acquired for every X-ray source kVp and power while there is no object inside the field of view. Then, collected images are normalized to a corrected image using a gain correction algorithm. This is a highly recommended processing step that corrects the X-ray image for the intensity variations of the X-ray beam and for gain variations in the Shad-o-Box camera (see chapter 4) [Dal16].

In addition, the software is only capable of working with one set of the detector modules, i.e. eight detectors, connected to one frame grabber. Therefore, another software using C programming language has been developed by our group members[(2)] to collect 2D-projections from all detectors, i.e. 32 detector modules connected to four frame grabbers, with selectable frame rate and exposure time. Moreover, the collected projections were interlaced [Dal16], therefore, we provided a MATLAB program to deinterlace the images at the beginning of the data treatment procedure (see section 4.1).

2. B.sc. Sumit Chakrabarty developed the software under my supervision. For more information about software development please refer to his project report.

3.1.9 System Adjustment

After constructing and connecting different hardware and software parts of the WATCH-CT, the system was adjusted to generate the first WATCH-CT image. The adjustment of the system was done using the cone phantom (see figure 3.25) and translation stages (see figure 3.24) using try and error method. This step is essential for the system construction and initial image reconstruction because after this step the small geometric errors, existing in the machine, could be corrected using a calibration technique.

3.1.10 Data Acquisition

Different types of data were acquired to reconstruct the images of the WATCH system. First important data were raw projections which were collected from the X-ray sensors after emitting the object by the X-ray tube at different angles. These data could not be directly reconstructed without being calibrated. Therefore, a procedure of data calibration was applied on the acquired projections (see chapter 4). Table 3.1 indicates parameters considered for the very first data collection and image reconstruction using the WATCH CT. We decided that about 1417 projections would accomplish a reasonable resolution. With try and error we could find out about the best possible voltage and brightness for provided phantoms.

TABLE 3.1: Experimental WATCH system parameters for image reconstruction

Data parameters	Value
Number of projections	1417
X-ray source Voltage[kV]	27
X-ray source power[W]	30
Number of pixels	16384
Time[h]	1:56

For collection of the data the speed of the robot must be set based on the frame rate of the detector system. The X-ray tube emits continuously. The frame rate changes slightly, therefore, for more accurately data collection, the frame rate was calculated few times and the average frame rate was used for calculation of the robot speed using speed equation:

$$V = \frac{s}{\Delta t} \tag{3.1}$$

Where Δt is the scanning time calculated using the number of view and frame rate values. Then, these parameters are multiplied to give the whole scanning time.

$$\Delta t = Numberofviews \times Framerate[s] \tag{3.2}$$

For our scan the parameters are indicated in table 3.1.

Furthermore, s is the path that the X-ray tube takes to complete one scan. This is calculated using parameters set in the robot program i.e. the X-ray tube path in radian and distance from robot coordinate's origin to iso-center. For our constructed WATCH system they are set to 4.45059 rad (255°) and 180 mm, respectively. These parameters are then multiplied as below:

$$s = \theta[Rad] \times R[mm] \tag{3.3}$$

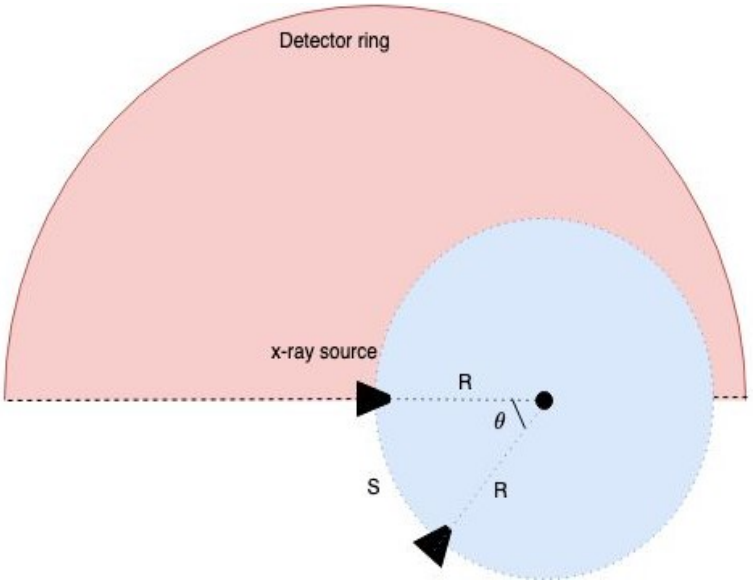

FIGURE 3.11: Parameters for calculation of robot speed

3.1.11 Test Objects

Several phantoms were chosen to accomplish a specific task based on their structure. We used four different phantoms such as one organic phantom, one object with sharp edges for system image quality assessment, A thin tantalum sheet and a micro-CT phantom.

3.1.11.1 Pumpkin Phantom

The first organic phantom was a pumpkin (see figure 3.12). It was chosen because of its organic tissue, its low absorption, its regions of air (for the high contrast), and its

non-circular contour. A pumpkin phantom was used for initial test and reconstruction of an image.

FIGURE 3.12: Pumpkin phantom used for the image reconstruction

3.1.11.2 Cuboid Silicon Phantom

In order to quantitatively characterize the system image quality a silicon phantom with sharp edges was chosen. The sharp edge of the phantom was used for modulation transfer function calculation and the homogeneous part of the object considered for the noise power spectrum evaluation. The size of this phantom is 65*55*30 mm.

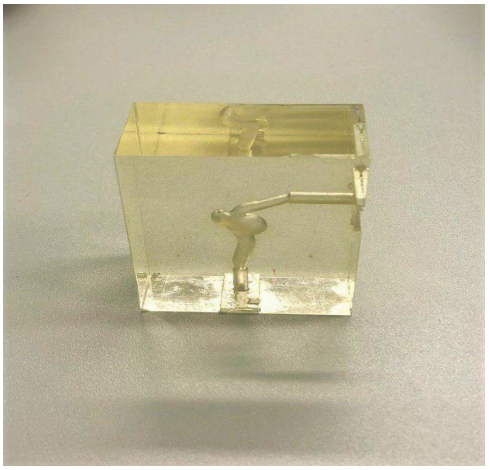

FIGURE 3.13: Silicon cuboid phantom used for the image reconstruction

3.1.11.3 Micro-CT QRM Phantom

The micro-CT QRM phantom with its defined dimensions and different structures was a proper object for visualizing the different contrasts and sizes. The phantom is made

from PMMA and its outer diameter is 50 mm [(3)] . The phantom was provided by Helmholtz center in Munich.

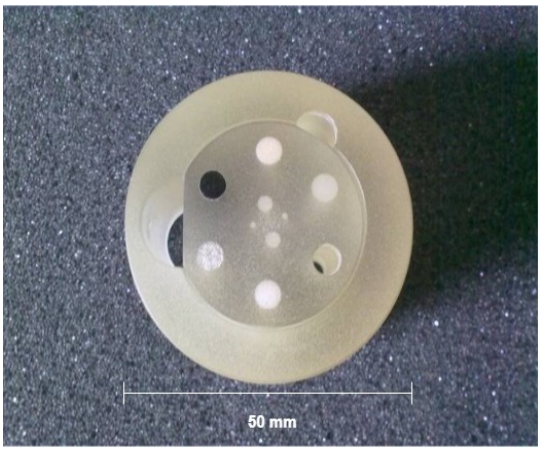

FIGURE 3.14: QRM micro-CT phantom used for the image reconstruction

3.1.11.4 Tantalum Sheet Phantom

A thin tantalum (99.9% Ta, Z = 73, thickness = 0.02 mm) sheet was reconstructed using OPED algorithm. The size of the phantom is 63.5 * 127 mm.

FIGURE 3.15: Tantalum sheet phantom used for image reconstruction

3. http://www.qrm.de/content/products.htm

3.2 New Geometric Calibration Methodology

In this section, a new calibration technique has been introduced for calibration of the CBCT scanners with flat panel detector and circular/spiral source trajectory. The concept of this section has been partially published in one of the IOP journal [TNH19]. In this method, seven geometric parameters are determined using directly formulae applied to coordinates of projected positions of calibration points onto the flat panel detector. Because of the freedom of choice for the origin of the z axis and for the origin of the gantry angle, two of these nine degree of freedom are removed, therefore, seven parameters are required to be determined.

The definition of the same variables used in the previous chapter has changed in this section.

3.2.1 Definition of the Calibration Geometry

Generally, a CBCT consists of a detector and an X-ray tube. Between the detector and the X-ray tube, there is a precision rotation plane designed for putting upon it an imaging object which is supposed to be a point. The table contains the X-ray source which is denoted by F, can rotate around the axis z, and can be shifted along axes x and y. The axes x, y and z are perpendicular to each other, that is, the triple xyz constitutes an orthogonal reference system.

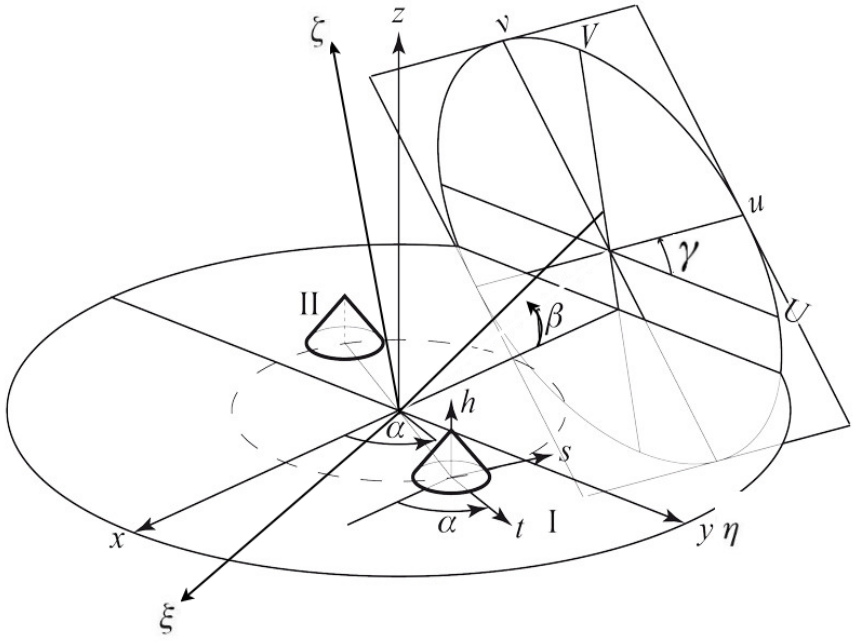

FIGURE 3.16: Geometric calibration initial setup configuration.

Coordinates in the detector plane are U and V. The initial configuration of these coordinate systems is illustrated in figure 3.16. Three coordinate systems are defined:

1) $Oxyz$ is a fixed orthogonal system, such that the plane $Oxyz$ contains the focus of the X-ray source; Oz coincides with the rotation axis of the rotation stage; Oy is parallel to the detector plane; Ox is directed from the detector plane.

2) $O\xi\eta\zeta$ is an orthogonal system, that is obtained from $Oxyz$ coordinate system by means of a rotation at angle β around axis Oy. Angle β is such that, the plane $O\xi$ is a normal to the detector plane. And the plane $O\eta\zeta$ is parallel to the detector plane. Moreover, axes $O\eta$ and $O\zeta$ are parallel to detector's axes u and v respectively.

3) $Otsh$ is an orthogonal system, where axes Ot, Os and Oh are axes of the cross stage.

Schematically, the passage from the system xyz to the system $O\xi\eta\zeta$ can be expressed by the following transition:

$$(x, y, z) \xrightarrow{\beta,\gamma/y,x} (\xi, \eta, \zeta) \tag{3.4}$$

The corresponding transformation matrix is so that:

$$\begin{pmatrix} \xi \\ \eta \\ \zeta \end{pmatrix} = \Gamma B \begin{pmatrix} x \\ y \\ z \end{pmatrix}, \Gamma B = \begin{pmatrix} cos\beta & 0 & -sin\beta \\ 0 & 1 & 0 \\ sin\beta & 0 & cos\beta \end{pmatrix} \begin{pmatrix} 1 & 0 & 0 \\ 0 & cos\gamma & sin\gamma \\ 0 & -sin\gamma & cos\gamma \end{pmatrix} \tag{3.5}$$

Above relation allows us to describe objects both in the system xyz and in the system $\xi\eta\zeta$. For example, the detector plane, if written in $\xi\eta\zeta$, is given by the following simple equation:

$$\xi = d \tag{3.6}$$

Where d is the distance between the detector and the origin O.

For a point p lying between the source and the detector a ray starting from the focus F, passing through a point p and intersecting the detector at a point (u, v) known as projection of p, then the following equations are valid:

$$\xi_p = R_x, \tag{3.7}$$

$$\eta_p = R_y + u, \tag{3.8}$$

$$\zeta_p = R_z + v, \tag{3.9}$$

Where $R = (R_x, R_y, R_z)$ is the vector connecting the origin O to the origin of the detector which can be chosen arbitrarily. If the projection of F onto the detector plane is denoted by P then:

$$D = \xi_f - R_\xi, \tag{3.10}$$

$$P_u = \eta_f - R_\eta, \tag{3.11}$$

$$P_v = \zeta_f - R_\zeta, \tag{3.12}$$

Where (D, P_u, P_v) are the components of the projection of the focus F in the detector plane (u, v) i.e. D is the distance between source and the detector (SDD). $f = (\xi_f, \eta_f, \zeta_f)$ is the coordinate of the focus in $O\xi\eta\zeta$ coordinate system.

The representation of the line that connects the focus F and the point $p = (\xi_p, \eta_p, \zeta_p)$ and intersects the detector plane at a point (u, v) is:

$$0 = D + (\xi_p - \xi_F)T(p) \tag{3.13}$$

$$u = P_u + (\eta_p - \eta_F)T(p) \tag{3.14}$$

$$v = P_v + (\zeta_p - \zeta_F)T(p) \tag{3.15}$$

From equation 3.13 we have:

$$T(p) = \frac{D}{\xi_F - \xi_p} \tag{3.16}$$

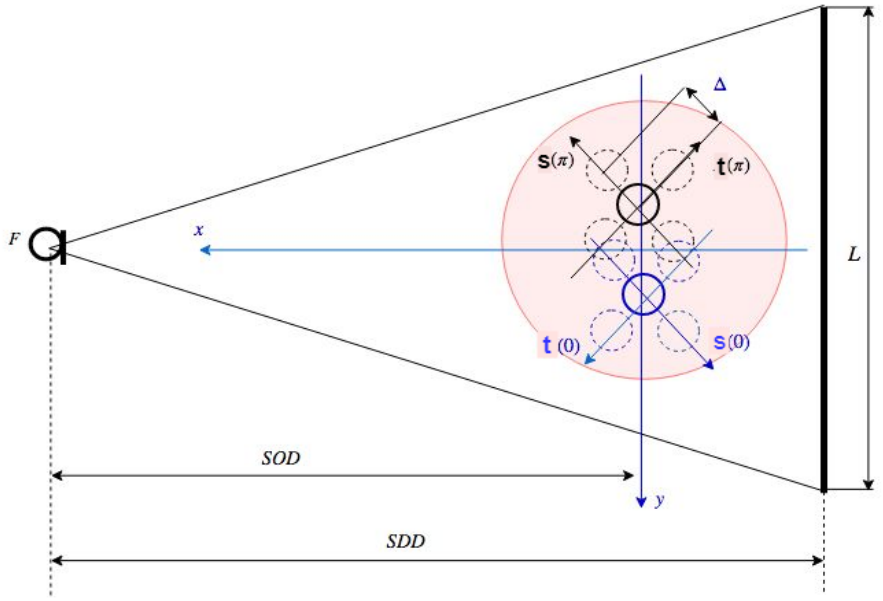

FIGURE 3.17: Geometric calibration initial setup configuration.

The unknown geometric parameters of the scanner are:

$$F(F_x, F_y), D, R(R_x, R_y, R_z), p(x, y, z), \beta, \gamma$$

Which can completely define the geometric arrangement of the system. The task is to recover these parameters.

Further important assumptions are: 1) The focus F lies on the central plane, which means that $F_z = 0$. 2) The axes η and ζ are parallel to the axes of the original reference system of the detector (these are lines and columns of pixels of the digital detector).

The task is to recover the geometric parameters from a set of the calibrating points which are fixed in the scanner reference frame and projections of which can be observed in the detector coordinate system. Moreover, there is a frame that is used for describing mutual arrangement of the calibrating points which are vertices of the octahedron. This reference system is referred as calibrating frame $Otsh$ (see figure 3.18).

Frame $Otsh$ is obtained from the reference frame $O\xi\eta\zeta$ via a shift and three rotations, so that the coordinates of a ponit p in both frames are related to each other as follows:

$$\begin{pmatrix} \xi_p \\ \eta_p \\ \zeta_p \end{pmatrix} = \begin{pmatrix} \xi_{p0} \\ \eta_{p0} \\ \zeta_{p0} \end{pmatrix} + \Omega^0 \begin{pmatrix} \Delta t \\ \Delta s \\ \Delta h \end{pmatrix} \tag{3.17}$$

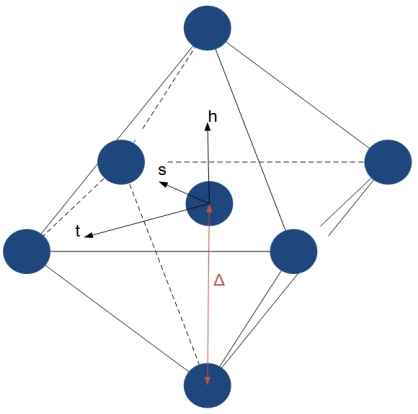

FIGURE 3.18: Shift of the calibration phantom resulted in an Octahedron shaped object.

Where $Ot_0s_0h_0$ is a reference frame in which the components $\Delta t, \Delta s, \Delta h$ of vector $\Delta p = p - p_0$ are known for any point p. And matrix Ω^0 indicates the transformation from $Ot_0s_0h_0$ to $O\xi\eta\zeta$ and it is defied as follow:

$$\Omega^0 = \Gamma B A^0 = \begin{pmatrix} \omega^0_{\xi,t} & \omega^0_{\xi,s} & \omega^0_{\xi,h} \\ \omega^0_{\eta,t} & \omega^0_{\eta,s} & \omega^0_{\eta,h} \\ \omega^0_{\zeta,t} & \omega^0_{\zeta,s} & \omega^0_{\zeta,h} \end{pmatrix} \tag{3.18}$$

where A^0 is the transformation matrix from $Ot_0s_0h_0$ to $Oxyz$ and it is defined as follow:

$$A^0 = \begin{pmatrix} \alpha_{x,t} & \alpha_{x,s} & \alpha_{x,h} \\ \alpha_{y,t} & \alpha_{y,s} & \alpha_{y,h} \\ \alpha_{z,t} & \alpha_{z,s} & \alpha_{z,h} \end{pmatrix} \tag{3.19}$$

Matrix A^0 does not need to be known, consequently no alignment between translation stages i.e. the $Otsh$ coordinate system, and the rotation table i.e. the $Oxyz$ reference system, is required.

The projection of the point p onto the detector plane can be interpreted as the point in which the ray emitted through the point p intersects the detector plane. It is easy to check that coordinates of the point of the intersection in the system $\xi\eta\zeta$ are the functions of $\Delta t, \Delta s, \Delta h$. By substituting equation 3.17 in equations 3.13-3.15 fundamental rational imaging functions are acquired which contain all the geometric parameters.

$$u = \frac{u_0 + a_t\Delta t + a_s\Delta s + a_h\Delta h}{1 + c_t\Delta t + c_s\Delta s + c_h\Delta h} = \frac{u_0 + a.\Delta p}{1 + c.\Delta p} \tag{3.20}$$

$$v = \frac{v_0 + b_t\Delta t + b_s\Delta s + b_h\Delta h}{1 + c_t\Delta t + c_s\Delta s + c_h\Delta h} = \frac{v_0 + b.\Delta p}{1 + c.\Delta p} \tag{3.21}$$

where u_0 and v_0 are the components of the projected coordinates of the initial point p_0 in detector coordinate system. a, b and c are the coefficient vectors and are defined as follow:

$$a = T_0\omega_\eta^0 + P_u c \tag{3.22}$$

$$b = T_0\omega_\zeta^0 + P_v c \tag{3.23}$$

$$c = -\frac{T_0}{D}\omega_\xi^0 \tag{3.24}$$

Where $\omega_\xi^0, \omega_\eta^0$ and ω_ζ^0 are indicating the rows of the matrix Ω^0 and T_0 is equal to $T(p_0)$.

In section 3.2.3, these coefficients are calculated using measured values on the detector but for deriving analytical expressions of geometric parameters these coefficients are assumed to be known.

3.2.2 Determining Geometric Parameters

After calculation of the coefficients of the rational function in section 3.2.3, Considering equations 3.22-3.24, and the fact that dot product of orthogonal vectors is equal to zero and the cross product of orthogonal vectors is equal to their multiplication, one finds the following expressions for the geometric parameters:

$$P_u = \frac{a \cdot c}{c \cdot c} = \frac{A \cdot C}{C \cdot C}, P_v = \frac{B \cdot C}{C \cdot C} \tag{3.25}$$

$$D = \frac{a \times c}{c \cdot c} = \frac{b \times c}{c \cdot c} = \frac{1}{2}\frac{(a+b) \times c}{c \cdot c} \tag{3.26}$$

$$D = \frac{A \times C}{C \cdot C} = \frac{B \times C}{C \cdot C} = \frac{1}{2}\frac{(A+B) \times C}{C \cdot C} \tag{3.27}$$

Where . is the dot product and $\times$ is the cross product of the vectors. Following the section 3.2.3, variables a, b and c denote the coefficients which correspond to the initial

position p_0, and variables A, B and C denote the coefficients which correspond to the second position of the phantom p_1.

Using equations 3.22-3.24 we can rewrite the matrix Ω^0 as follows:

$$\Omega^0 = \frac{1}{T_0}\begin{pmatrix} -Dc_t & -Dc_s & -Dc_h \\ a_t - P_u c_t & a_s - P_u c_s & a_h - P_u c_h \\ b_t - P_v c_t & b_s - P_v c_s & b_h - P_v c_h \end{pmatrix} \tag{3.28}$$

As a result, the geometric parameters D, P_u, P_v and the transformation matrix Ω^0 can be calculated using one projection of the calibration set. One additional projection is required for calculation of geometric parameters β, γ and the position of the focus F and the calibrating point p_0.

The additional projection is acquired after the rotation of the calibration set around the Oz axis at angle π. The new coordinate system is indicated as $Ot_1s_1h_1$ and it is transformed to the $Oxyz$ reference system using the A^1 transformation matrix defined as follows:

$$A^1 = \begin{pmatrix} -\alpha_{x,t} & -\alpha_{x,s} & -\alpha_{x,h} \\ -\alpha_{y,t} & -\alpha_{y,s} & -\alpha_{y,h} \\ \alpha_{z,t} & \alpha_{z,s} & \alpha_{z,h} \end{pmatrix} \tag{3.29}$$

Consequently, the transformation matrix Ω^0 is changed to Ω^1 and it is defined as below:

$$\Omega^1 = \Gamma B A^1 = \frac{1}{T_1}\begin{pmatrix} -DC_t & -DC_s & -DC_h \\ A_t - P_u C_t & A_s - P_u C_s & A_h - P_u C_h \\ B_t - P_v C_t & B_s - P_v C_s & B_h - P_v C_h \end{pmatrix} \tag{3.30}$$

To determine the other geometric parameters we calculate the following values for k=0,1,

$$U_k = (u_k - P_u)cos\gamma - (v_k - P_v)sin\gamma \tag{3.31}$$

$$V_k = (u_k - P_u)sin\gamma + (v_k - P_v)cos\gamma \tag{3.32}$$

and,

$$\|c\| = c_t^2 + c_s^2 + c_h^2 \tag{3.33}$$

$$\|C\| = C_t^2 + C_s^2 + C_h^2 \tag{3.34}$$

These values are then used for determination of angles β and γ which are derived from $\Omega^0 + \Omega^1$. This is explained in detail in appendix A.

$$tan\gamma = \frac{(a_i - P_u c_i)\|C\| + (A_i - P_u C_i)\|c\|}{(b_i - P_u c_i)\|C\| + (B_i - P_u C_i)\|C\|} \tag{3.35}$$

and

$$tan\beta = \frac{c_i T_1 + C_i T_0}{(b_i - P_v c_i)T_1 + (B_i - P_v C_i)T_0} D cos\gamma \tag{3.36}$$

Additionally, other geometric parameters such as coordinates of the calibration point at the initial location $p_0 = (x_0,\, y_0,\, z_0)$ and the focus spot position $F = (F_x,\, F_y,\, F_z = 0)$ are determined as follows. The detailed derivation of these equations is given in the appendix A.

$$x_0 = \frac{1}{2}\left(\frac{1}{\|C\|} - \frac{1}{\|c\|}\right)\frac{1}{cos\beta} \tag{3.37}$$

$$y_0 = \frac{1}{2}\left(\frac{U_0}{\|c\|} - \frac{U_1}{\|C\|}\right) \tag{3.38}$$

$$z_0 = \frac{\Delta}{2}\left[\left(\frac{1}{\|C\|} + \frac{1}{\|c\|}\right)sin\beta - \left(\frac{V_1}{\|C\|} + \frac{V_0}{\|c\|}\right)\frac{cos\beta}{D}\right] \tag{3.39}$$

The values of the focus position are calculated as follow:

$$F_x = \frac{\Delta}{2}\left[\left(\frac{1}{\|C\|} + \frac{1}{\|c\|}\right)cos\beta - \left(\frac{V_1}{\|C\|} + \frac{V_0}{\|c\|}\right)\frac{sin\beta}{D}\right] \tag{3.40}$$

$$F_y = \frac{\Delta}{2}\left(\frac{U_0}{\|C\|} + \frac{U_1}{\|c\|}\right)\frac{1}{cos\beta} \tag{3.41}$$

Where Δ is the shift value (see section 3.2.3). The last but not least important parameter to be determined is the vector $R = (R_x,\, R_y,\, R_z)$ pointing from origin O to the center of the detector. This parameter is calculated by considering equation 3.5 and equation 3.10-3.12.

$$R_x = F_x - Dcos\beta - (P_u sin\gamma + P_v cos\gamma)sin\beta \tag{3.42}$$

$$R_y = F_y - (P_u cos\gamma - P_v sin\gamma)sin\beta \tag{3.43}$$

$$R_z = Dsin\beta - (P_u sin\gamma + P_v cos\gamma)cos\beta \tag{3.44}$$

3.2.3 Recovering the Coefficients from Calibration Measurements

The phantom i.e. shifts of the translation stage, is defined in the $Otsh$ coordinate system as follows. There are seven points: the initial point p0 and six other points:

$$p_{\pm t} = p_0 \pm (\Delta, 0, 0) \tag{3.45}$$

$$p_{\pm s} = p_0 \pm (0, \Delta, 0) \tag{3.46}$$

$$p_{\pm h} = p_0 \pm (0, 0, \Delta) \tag{3.47}$$

where $\{p_{\pm t}, p_{\pm s}, p_{\pm h}\}$ is a set of points in calibration frame $Otsh$.

The value of Δ is as big as possible for the given configuration, ideally, so that, the projections of the phantom occupies the most part of the detector area. Seven measurements are done with initial point p_0; then rotation of the point p_0, 180° around Oz, and seven measurements with initial point $p1$. For each position of the phantom i.e. p_0 and p_1, nine coefficients have to be calculated. In the following equations, variables a, b and c denote the coefficients which correspond to position p_0, and variables A, B and C denote the coefficients which correspond to p_1.

Denote measured components of the projection of calibrating point $\pm p$ as $(u_{\pm i},\ v_{\pm i})$ where $i = t, s$ and h, and rewrite the expressions in equations 3.20 and 3.21 in the form of:

$$\pm\ \Delta(a_i - u_{\pm i}c_i) = u_{\pm i} - u_0 \tag{3.48}$$

$$\pm\,\Delta(b_i - v_{\pm i}c_i) = v_{\pm i} - v_0 \tag{3.49}$$

After all measurements have been done, one has to carry out the following calculation:

$$c_t = \pm 1 + 2\frac{u_{\pm t} - u_0}{u_{-t} - u_t} = \pm 1 + 2\frac{v_{\pm t} - v_0}{v_{-t} - v_t} \tag{3.50}$$

$$c_s = \pm 1 + 2\frac{u_{\pm s} - u_0}{u_{-s} - u_s} = \pm 1 + 2\frac{v_{\pm s} - v_0}{v_{-s} - v_s} \tag{3.51}$$

$$c_h = \pm 1 + 2\frac{u_{\pm h} - u_0}{u_{-h} - u_h} = \pm 1 + 2\frac{v_{\pm h} - v_0}{v_{-h} - v_h} \tag{3.52}$$

There are several representations. We have to choose the best one in terms of accuracy. As an example consider c_t. If $|u_{-t} - u_t| > |v_{-t} - v_t|$, then we choose:

$$c_t = \pm 1 + 2\frac{u_{\pm t} - u_0}{u_{-t} - u_t} \tag{3.53}$$

as the coefficient with highest accuracy.

The other coefficients are calculated using following equations:

$$a_t = u_t c_t + (u_t - u_0) = u_{-t}c_t - (u_{-t} - u_0) \tag{3.54}$$

$$a_s = u_s c_s + (u_s - u_0) = u_{-s}c_s - (u_{-s} - u_0) \tag{3.55}$$

$$a_h = u_h c_h + (u_h - u_0) = u_{-h}c_h - (u_{-h} - u_0) \tag{3.56}$$

and,

$$b_t = v_t c_t + (v_t - v_0) = v_{-t}c_t - (v_{-t} - v_0) \tag{3.57}$$

$$b_s = v_s c_s + (v_s - v_0) = v_{-s}c_s - (v_{-s} - v_0) \tag{3.58}$$

$$b_h = v_h c_h + (v_h - v_0) = v_{-h}c_h - (v_{-h} - v_0) \tag{3.59}$$

By substituting u_0, v_0, u_i and v_i values at position p_0 by values of u_1, v_1, u_i and v_i at the position p_1, coefficients of rational functions at the second position p_1 of the point set are calculated and they are denoted as A_i, B_i and C_i.

3.2.4 Conic Body as Calibration Phantom

In this project we have introduced a new calibration phantom which is a high density conic body. Since the accuracy of the calculated geometric parameters are directly related to the measurement, therefore, in this study instead of a conventional high density ball a high density cone has been introduced and the apex of the cone projection is considered as the calibration point which can be more precisely estimate resemble a point in comparison to the center of the high density ball phantom. The problem with high density ball as a calibration phantom is that the projection of a ball is an ellipse and the center of the ball may lie neither at the center nor at the focus of the ellipse, therefore, the precision of the detected point decreases. In one study, they measure the center of the mass of the ball as the calibration point which is also problematic due to inhomogeneities in gray values of the ball shadow[TnH17].

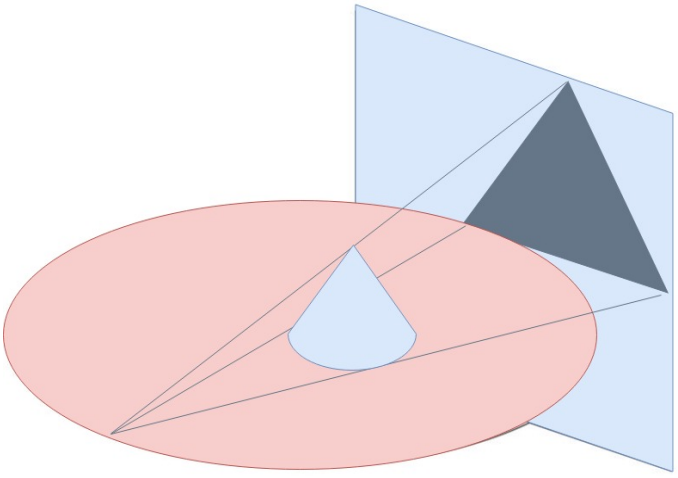

FIGURE 3.19: Schematic of a cone body projection into a detector.

In the procedure of calculation of the point object, first, one projection was generated (see figure 3.20a), then an edge detection method such as the Canny edge detector [MA09], was applied to segment the edges of the cone phantom (see figure 3.20b). Afterwards, two lines are fitted to the segmented pixels of the edges and the intersection point of these two lines is considered as the apex of the cone projection which is the calibration point. This is illustrated in figure 3.20c.

3.3 Geometric Parameters Correction

All needs to be done is to find the position of the source and the sensors in a fixed coordinate system which is the three dimensional coordinate system of the robot $x_r y_r z_r$, i.e. Tool coordinate system (see figure 3.9) which one of its axis goes through the ideal

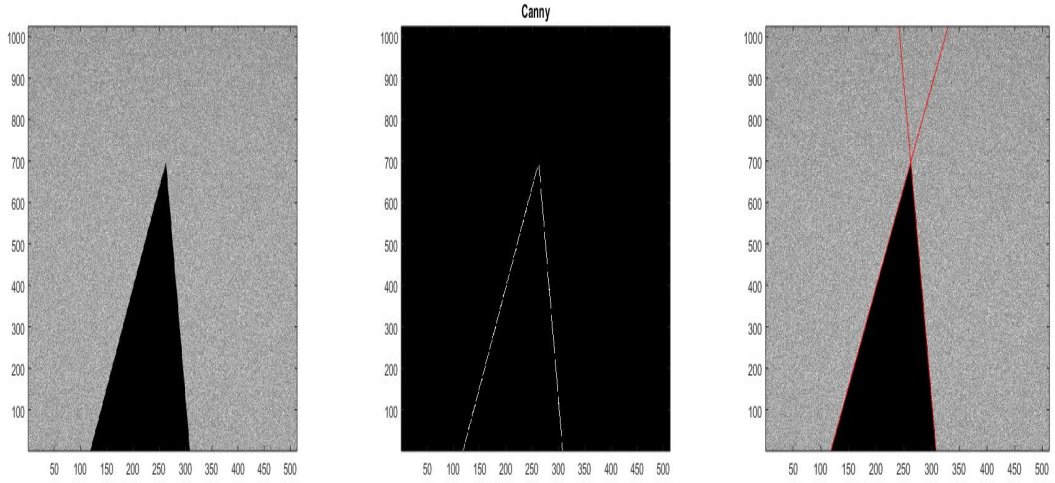

(a) (b) (c)

FIGURE 3.20: (a): A projection of the cone phantom acquired using the simulation. (b): The detected edges of the cone using Canny edge detection method. (c): Red lines are the fitted lines to the sides of the cone projection while the intersection point is the calibration point.

focus spot position, its z_r axis is the same as the rotation axis of the system and the y_r axis is perpendicular to the x_r and z_r axes.

After determination of geometric parameters, first the focus spot was found and the corrections procedure, given in section 3.3, was then applied on the data before reconstruction of an image. Since all the sensors are placed on a same holder with approximately similar geometric parameters (see figure 3.8), therefore, instead of calculating the geometric parameters of every single sensor, several of them are chosen and calculated. Here, these sensor are referred to as selected sensors and the parameters of the other sensor could be calculated based on the parameters of the selected sensors.

3.3.1 Focus Spot Positioning

In figure 3.21, $x_n y_n z_n$, n = 1,..., Sensors Number are the calibration coordinate systems for each selected sensor. The calculated values for F_x and F_y are then used for finding the focus spot. As the distance from the ideal focus spot (red dot) to the z axis is fixed and defined in the robot program. The distance between the measured focus spot (blue dots) and the z axis is found by equation $\sqrt{F_x^2 + F_y^2}$. When given three points (measured positions of the focus) there is a unique circle passing them. Then the focus spot position is the center of the of this circle.

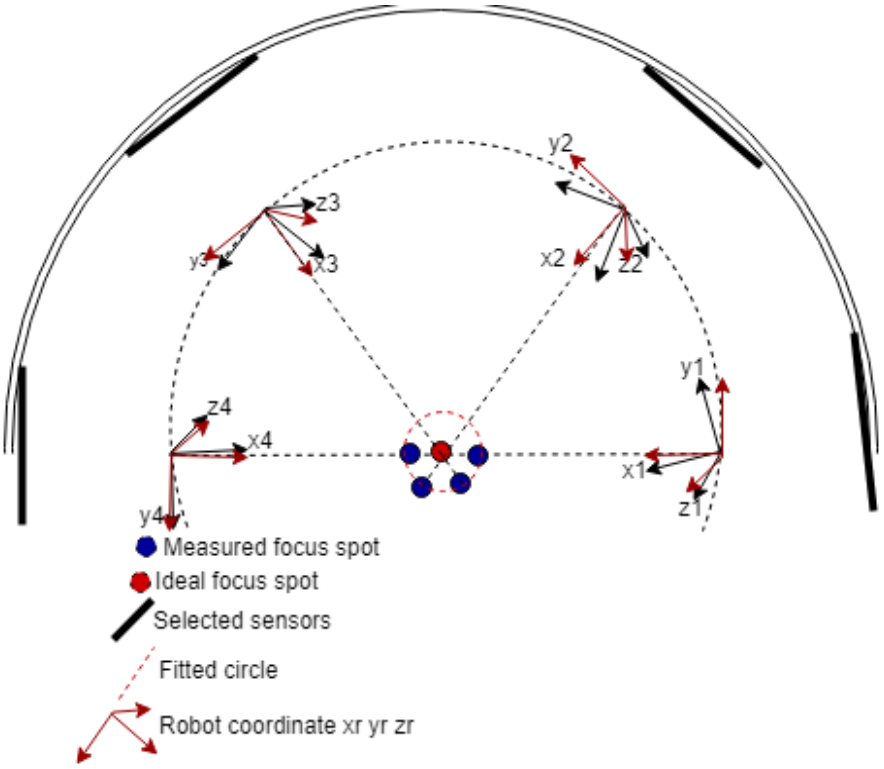

FIGURE 3.21: Schematic of WATCH focus spot calculation mounted on the KUKA robotic arm.

The coordinate of the robot $x_r y_r z_r$ is unknown relative to the detectors and the focus spot but it is known after finding the focus spot and placing it at its ideal position (red dot in figure 3.21). Thus the calibration parameters of each could be simply transformed to the robot coordinate using a rotation matrix around z axis with angle $arctan\frac{F_y}{F_x}$.

3.3.2 Geometric Correction

Unfortunately, it seems impossible to build an ideal device that would provide us with data of desired geometry. However one can appropriately re-sample collected data as described in this section.

The idea of geometry calibration parameters correction is to initially find the location of all detector modules in the fixed coordinate system of the KUKA robotic arm (see black lines in figure 3.22) by employing the geometric parameters and then consider any ideal detector ring which includes the desired rays for OPED reconstruction algorithm (see blue curves in figure 3.22). Using the following equations the proper pixels which collect the parallel rays and angles data of these pixels could be calculated.

Equation of parallel rays which could be used for OPED reconstruction is given by:

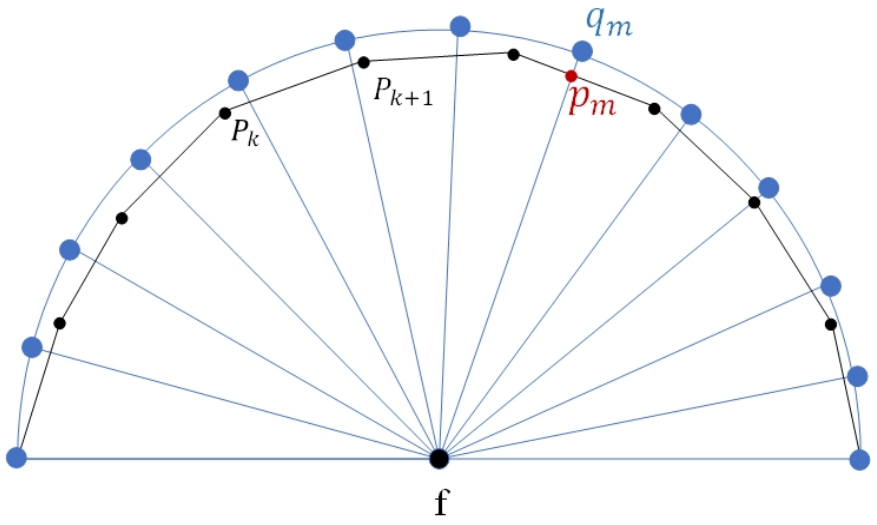

FIGURE 3.22: The correction idea for WATCH images. Blue ring indicate a virtual detector collecting ideal rays for OPED algorithm. Black lines are the actual polygonal detector. The blue lines resemble the rays intersecting proper pixels.

$$r_m = f + \tau_m s, \qquad s \in \Re \tag{3.60}$$

where,

$$\tau_m = \frac{q_m - f}{\|q_m - f\|} \tag{3.61}$$

which is the line connecting points f and q_m. The equation of the line connecting points P_k and P_{k+1} which is indicating an X-ray detector and its pixels is expressed by:

$$R_k = P_k + n_k t, \qquad t \in \Re \tag{3.62}$$

where,

$$n_k = \frac{P_{k+1} - P_k}{\|P_{k+1} - P_k\|} \tag{3.63}$$

Where these two lines encounter is the point or projection pixels which could be used for image reconstruction. This condition is represented as:

$$\begin{aligned} P_{k,x} + n_{k,x}t &= f_x + \tau_{m,x}s \\ P_{k,y} + n_{k,y}t &= f_y + \tau_{m,y}s \end{aligned} \tag{3.64}$$

where the unknown variables t and s needed to be found. If t_0 and s_0 are the solution of these equations, then, the desired pixel is found using:

$$R_k = P_k + n_k t_0 \tag{3.65}$$

Following the section 3.2, expansion of the above method to the actual geometric parameters is as follows. Let τ be a unit vector lying in the central plane, i.e. $\tau_z = 0$. The task is to find a point of intersection of lines.

$$r = F + t\tau \tag{3.66}$$

With the detector plane. Expansion of equation 3.66 is:

$$\begin{cases} \xi = \xi_f + t\tau_\xi \\ \eta = \eta_f + t\tau_\eta \\ \zeta = \zeta_f + t\tau_\zeta \end{cases} \tag{3.67}$$

Since equation of the detector plane in $O\xi\eta\zeta$ is:

$$\xi = R_\xi \tag{3.68}$$

Using equation 3.10 one obtains that:

$$t = -\frac{D}{\tau_\xi} \tag{3.69}$$

and consequently:

$$\begin{cases} \eta = \eta_f - \frac{D}{\tau_\xi}\tau_\eta \\ \zeta = \zeta_f - \frac{D}{\tau_\xi}\tau_\zeta \end{cases} \tag{3.70}$$

Using transformation:

$$\begin{pmatrix} \xi \\ \eta \\ \zeta \end{pmatrix} = \Gamma B \begin{pmatrix} x \\ y \\ z \end{pmatrix} \tag{3.71}$$

Where,

$$\Gamma = \begin{pmatrix} 1 & 0 & 0 \\ 0 & \cos\gamma & \sin\gamma \\ 0 & -\sin\gamma & \cos\gamma \end{pmatrix}, B = \begin{pmatrix} \cos\beta & 0 & -\sin\beta \\ 0 & 1 & 0 \\ \sin\beta & 0 & \cos\beta \end{pmatrix} \tag{3.72}$$

One can rewrite equation 3.67

$$\eta = F_y cos\gamma + F_z sin\gamma - \frac{D(\tau_y cos\gamma + \tau_z sin\gamma)}{\tau_x cos\beta + (\tau_y sin\gamma - \tau_z cos\gamma)sin\beta} \tag{3.73}$$

$$\zeta = F_x sin\beta - (F_y sin\gamma - F_z cos\gamma)cos\beta - \frac{D(\tau_x sin\beta - (\tau_y sin\gamma - \tau_z cos\gamma)cos\beta)}{\tau_x cos\beta + (\tau_y sin\gamma - \tau_z cos\gamma)sin\beta} \tag{3.74}$$

Which after recalling that $F_z = \tau_z = 0$ becomes:

$$\eta = F_y cos\gamma - \frac{D\tau_y cos\gamma}{\tau_x cos\beta + \tau_y sin\gamma sin\beta} \tag{3.75}$$

$$\zeta = F_x sin\beta - F_y sin\gamma cos\beta - \frac{D(\tau_x sin\beta - \tau_y sin\gamma cos\beta)}{\tau_x cos\beta + \tau_y sin\gamma sin\beta} \tag{3.76}$$

Recalling that,

$$\begin{pmatrix} \xi \\ \eta \\ \zeta \end{pmatrix} = R + \begin{pmatrix} 0 \\ u \\ v \end{pmatrix} \tag{3.77}$$

where (u, v) are the coordinates in the detector plane relative to the detector reference point, then we have:

$$u = (F_y - R_y)cos\gamma - \frac{D\tau_y cos\gamma}{\tau_x cos\beta + \tau_y sin\gamma sin\beta} \tag{3.78}$$

$$v = (F_x - R_x)sin\beta - (F_y - R_y)sin\gamma cos\beta - \frac{D(\tau_x sin\beta - \tau_y sin\gamma cos\beta)}{\tau_x cos\beta + \tau_y sin\gamma sin\beta} \tag{3.79}$$

The last two equations give the coordinates of the point of intersection of line equation 3.66 with the detector plane.

The point (u, v) where line equation 3.66 intersects the detector can be represented as

$$\begin{cases} u = (m + \epsilon_u)\delta \\ u = (m + \epsilon_u)\delta \end{cases} \tag{3.80}$$

Where δ is a pixel size, and

$$\begin{cases} m = \frac{u}{\delta} \\ n = \frac{v}{\delta} \end{cases} \tag{3.81}$$

3.4 Geometric Calibration Simulation Study

A simulation study has been conducted to test the proposed geometric calibration technique. This simulation was implemented using the Geant4 Monte-Carlo simulation toolkit [GAea03]. The simulation parameters are illustrated in table 3.2 and 3.3. Based on this study the accuracy and reliability of our proposed method was tested.

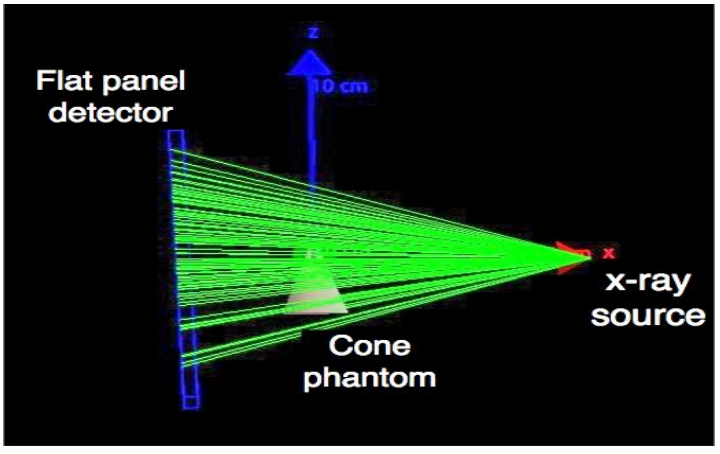

FIGURE 3.23: Standard cone beam micro-CT simulation using Geant4 toolkit for calibration technique study

In this study, a standard CB micro-CTs was simulated using an X-ray source, a rotation table, a flat panel detector and a cone object made of high density material such as

lead alloy. The phantom was placed in fourteen different positions as required for our calibration technique, where the cone apexes resembled a shape illustrated in figure 3.18.

Moreover, a MATLAB program was written to display the cone projections, extract the apexes of the cone projections and calculate the geometric parameters for the CB micro-CT scanner using measured values. The edge method employed in this investigation was the Canny edge method [MA09] (see figure 3.20).

Two simulation studies were conducted to evaluate the proposed calibration technique. First simulation study was done for a system with geometric parameters similar to standards micro-CTs and the second system was simulated based on the geometric parameters of the second prototype of the WATCH system. These parameters are indicated in table 3.2 and 3.3.

TABLE 3.2: Simulation parameters for geometric calibration of the first CB micro-CT

Parameters	Values
SOD [mm]	50
SDD [mm]	150
Fan in °	60
N_{pix}	1600
N_{pix}	1600
$P_x[mm]$	0.1
$P_y[mm]$	0.1

TABLE 3.3: Simulation parameters for geometric calibration of the second micro-CT

Parameters	Values
SOD [mm]	185
SDD [mm]	250
Fan in °	40
N_{pix}	512
N_{pix}	1024
$P_x[mm]$	0.0480
$P_y[mm]$	0.0480

3.5 Geometric Calibration Experimental Study

After obtaining the simulation results, the experimental setup was constructed to assess the geometric calibration parameters in our laboratory using the second prototype of the WATCH system. To realise the calibration procedure a setup, described in the following sections, was prepared.

3.5.1 Translation and Rotation Stages

Three manual translation stages [(4)] were connected to each other to resemble the cross stage i.e. *Otsh* coordinate system (see figure 3.24). The accuracy of this manual stages could reach 1.0 μm. The cross stage was placed on a motorized rotation stage with accuracy of 0.5 μdegree and then on a adjustable DQE measurement tripod to make also the angle adjustment suitable for the calibration phantom. This full adjustment system allow the correct placement of the cone in different positions with a larger shift.

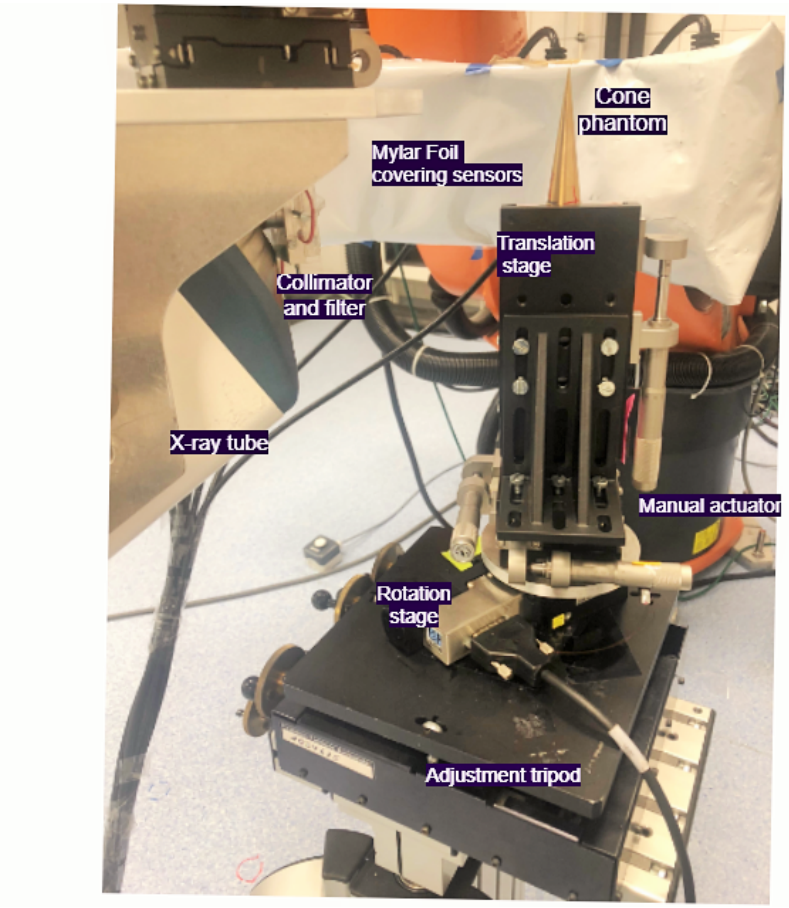

FIGURE 3.24: WATCH-CT calibration test setup

3.5.2 Calibration Phantom

A cone phantom made of brass and lead alloy with the size of 20*70 mm (see figure 3.25) was constructed in the workshop of our faculty and was placed inside the field of view of the WATCH-CT scanner, then the calibration procedure based on the protocol as described in section 3.6, was implemented. The size of the phantom was determined

4. provided by Newport

based on the previous simulation studies done for this system using the Geant4 toolkit [GAea03].

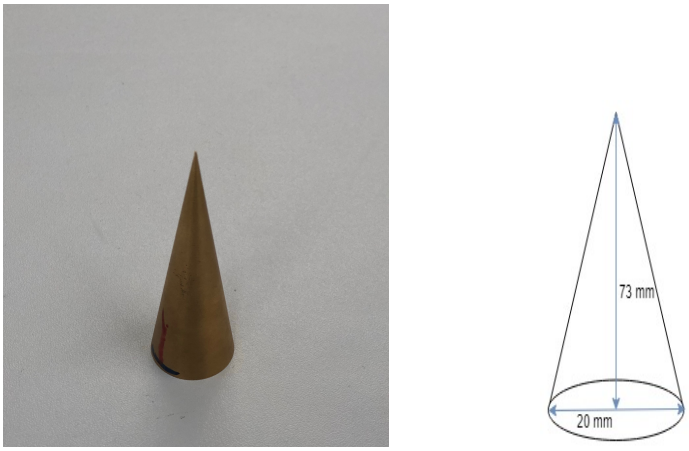

FIGURE 3.25: High density cone-shaped geometric calibration phantom.

3.6 Geometric Calibration Protocol

3.6.1 Determining Focus Position

Place the focus spot at the correct position using the following protocol and the method given in section 3.3.1. The following protocol first is used to find the focus position and then other the geometric parameters.

3.6.2 Determining Geometric Parameters

1. Placing the cone phantom as close as possible to the iso-center to make sure that cone stays inside the field of view for all positions of the calibration phantom.

2. Placing the phantom in seven different positions as described in section 3.2, using three dimensional translation stage and producing the projections (see figure 4.9). At the end, the apexes of the conic body in different positions should resemble an octahedron shape.

3. Rotating the stage (or the CT scanner) 180° around the iso-center and placing the object in seven positions and producing the cone projections.

4. Calculating the coordinates of the apex of the cone projection in different positions using the MATLAB routine, then calculating the geometric parameters (see figure 4.10).

5. Re-sampling the sinogram using calibration parameters and reconstructing the image using the OPED algorithm.

In this protocol the whole procedure should be implemented for each sensor and the geometric parameters are determined for each detector module one after the other.

3.7 Fourier-Based Image Quality Assessment of the WATCH System

3.7.1 Modulation Transfer Function, Noise Power Spectrum

There are several approaches to assess the spatial resolution of an image which has been modified in the image generation process. The image resolution conventionally is calculated using a thin metal wire, however, MTF of an image could be limited by different factors such as detector pitch and displayed pixel pitch. Hence, the resolving capabilities of the WATCH geometry have been evaluated with the consideration to reduce all possible factors that may influence the true response of these systems due to the digital sampling characteristics associated with computed tomography. The applied method for determining the pre-sampled MTF is based on the over sampling of the edge spread function (ESF) [Ill05].

For calculations of the pre-sampled MTF the region of interest (ROI) is applied on reconstructed images for central positions of field of view (FOV). Further steps involve construction of an over-sampled ESF from data points defined by pixels in the ROI. It uses a group of N consecutive lines to construct the over-sampled ESF, where N is determined by the condition that the total shift of the edge transition from the first line to the Nth line should be as close as possible to one pixel in the x direction. The second step of the algorithm is to interlace N consecutive lines to construct the over-sampled edge profile [Ill05](see figure 3.26).

The third step is to assume as an approximation that the data points belonging to the over-sampled edge profile have been sampled on a regular subsampling grid rather than on the true one. The data set describing the over-sampled line spread function (LSF) is derived from the over-sampled ESF by finite-element differentiation using, e.g., a convolution filter with a [-0.5,0,0.5] kernel [ESU03]. The MTF is then finally derived

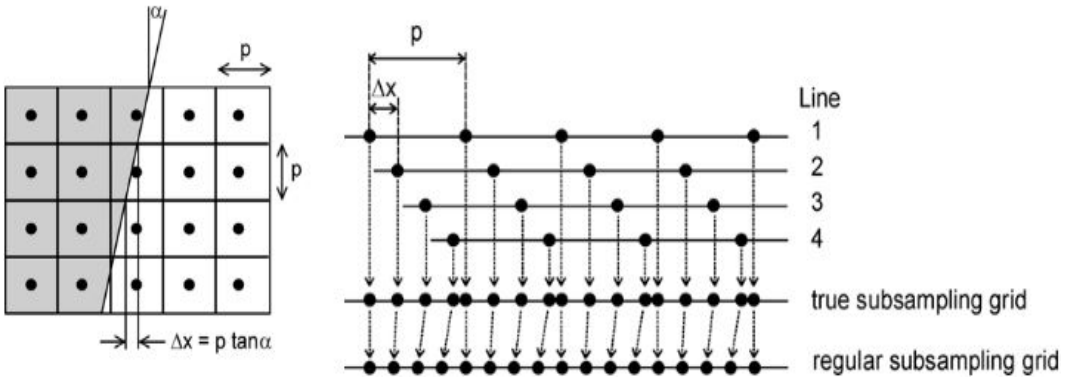

FIGURE 3.26: Orientation of edge relative to the pixel matrix (schematically, edge angle exaggerated). [Ill05]

by using fast Fourier transform of the ESF which is further normalized to 1, by dividing them to the maximum value present in the MTF curve.

For calculations of the pre-sampled MTF, we used a silicon cuboid phantom to utilize its edge properties. The image for the MTF evaluation was reconstructed with a sufficiently small FOV and a large image matrix to prevent aliasing from affecting the MTF curve. Therefore, the FOV size was 229 mm, the image matrix size was 2300*2300 and the ROI size was 227*227 pixel. This gave a sampling interval of 0.0995 mm. Moreover, the phantom was inclined at an angle of 2.5° with the consideration of the effects of the relative error ΔMTF/MTF as indicated by E. Buhr et al.[ESU03], that shows a higher relative error with the increase of edge tilt angle due to decrease in the average number of lines available per edge shift by one pixel. Hence, the edge angle is kept within an acceptable range. Figure 3.26 illustrates the subsampling of the edge as well the effect of the edge angle α. For this analysis we have assumed a linear and space-invariant system. However, these requirements are only locally fulfilled [Bru11].

The next study was to assess the noise behaviour using the power spectrum analysis. However, due to variation in the detected X-ray photon counts, a method of determining local noise power spectrum is adopted. As per the international standard IEC 62220-1 [IEC03], the noise power spectrum is determined using the relation,

$$NPS(u_n, v_k) = \frac{\Delta x.\Delta y}{M.p.q} \sum_{1}^{M} |\sum_{i=1}^{p}\sum_{j=1}^{q}(I(x_i, y_j) - S(x_i, y_j))exp(-2\pi i(u_n x_i + v_k y_j))|^2 \tag{3.82}$$

Where, Δx and Δy are the pixel spacing respectively in the horizontal and in the vertical direction, M is the number of ROIs, $I(x_i, y_j)$is the linearized data,$S(x_i, y_j)$ is the optionally fitted two-dimensional polynomial, $p.q$ is the size of the ROI.

In this study, evaluation was conducted for a FOV sizes of 229 mm. The size of the ROI was 32×32 array with overlap size of 16 pixels. The two dimensional NPS was evaluated for all the ROIs individually. Then, the two dimensional NPS is averaged for all the ROIs to get the noise spectrum which is then used to determine the one dimensional NPS along the frequency axes u [SkKM+18]. As per the international standard IEC 62220-1 [IEC03], seven rows or columns along both axes of the two-dimensional NPS, but not the axis itself, are omitted.

To assess the image quality of our constructed system we collected two set of data. The acquisition parameters presented in table 3.4 were used to collect the data utilizing the second prototype of the WATCH system. The process of reconstructing the required images for evaluation of the MTF and the NPS is presented in the next chapter, section 4.3.

TABLE 3.4: Experimental WATCH system parameters for MTF and NPS evaluation.

Data parameters	Value
Number of projections	1417
X-ray source Voltage[kV]	30
X-ray source power[W]	30
Number of pixels	16384
Phantom	Silicon cuboid
Time per Frame[s]	∼6

Chapter 4

Data Treatment

This chapter explains the conversion of the data from raw projections data into a sinogram and then a reconstructed image using the OPED algorithm. Each step of data treatment, i.e. data acquisition, correction of projections and processing of the data, were carried out using different softwares, i.e. MATLAB program and ELTEC p3I3 software (see section 3.1.8).

Section 4.1 presents the data treatment for the WATCH system in preparation of the image reconstruction. In section 4.2, the data treatment required during the calibration procedure is presented. Moreover, in this section, the data treatment method, required for analysing calibration parameters, for reconstructing a suitable image is proposed. Finally, section 4.3 presents the process of image reconstruction for images required for quality assessment.

4.1 Data Treatment for Image Reconstruction

An overview of this section is exemplified in flowchart 4.1. The data collected from the WATCH system requires several steps of data processing to acquire the final image as it is shown in figure 4.1. Different data are collected and merged into a final sinogram of non-equally spaced parallel rays which was then reconstructed using the OPED algorithm (1)

First, three types of data were collected as described in previous section (section 3.1.8) using parameters illustrated in table 3.1. These data are object projection, offset or dark current and gain or air scan projections. Collected projections uisng the software were interlaced, therefore, a de-interlacing procedure was required to decoded the images. A

1. Author: Martin.Lingenheil, Created on: 11.01.2010

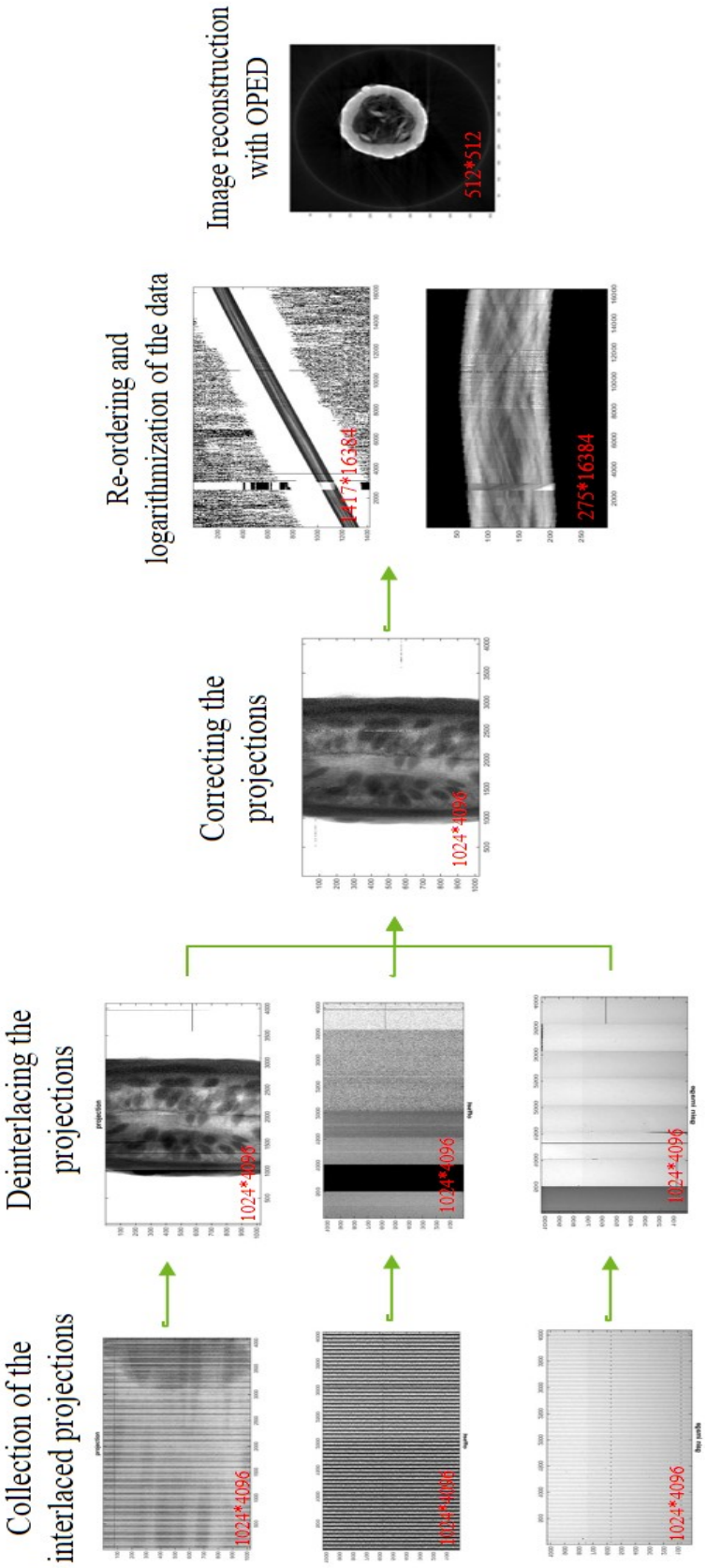

FIGURE 4.1: Flowchart of image reconstruction in experimental WATCH-CT system. Here the pumpkin phantom has been exemplified.

MATLAB routine was developed for deinterlacing the data. Furthermore, these three types of data were combined to produce the final corrected projections (see equation 4.2). Sufficient number of these projections were generated (see table 3.1) and re-ordered to create the sinogram of non-equally spaced parallel rays. Then, the sinogram was used as an input for the OPED reconstruction algorithm. In following sections, each part is discussed more in detail.

4.1.1 Raw Data Collection

Raw projections were produced using parameters indicated in table 3.1. The produced data were interlaced after collection using the shado-cam library [(2)] , therefore a MATLAB program was written to de-interlace the images. Images originally produced and after the process of deinterlacing are illustrated in figure 4.2. The size of the illustrated projection is 1024 * 4096 which indicates eight Radeye1 sensors (each with the size of 1024 * 512) collected with one frame grabber as explained in section 3.1.4.

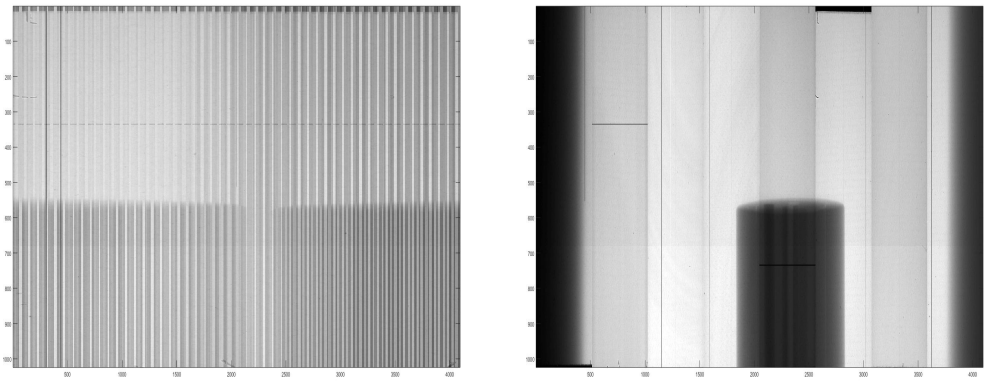

FIGURE 4.2: Raw data collected Left: the interlaced projection.Right: the same projection after de-interlacing

4.1.2 Gain and Offset Data Collection

Gain (or air) and offset correction is needed to take into account the intensity differences in pixels, the dark or offset signals of the X-ray sensors and variations in external electronics signals. The gain image was acquired without any object in the field of view. The correction was achieved through air scan correction and offset subtraction (see equation 4.2). The gain data were collected without an object in the field of view with X-ray tube on with the same power and voltage as used for raw data collection, while offset data were collected without X-ray exposure. The gain and offset data were interlaced after

2. Provided by ELTEC company

collection, therefore, the de-interlacing program was utilized to de-interlace images. The offset and gain projections before and after de-interlacing process are illustrate in figure 4.3 and 4.4 respectively. In the left side of the figure 4.3 and 4.4 the interlaced image and in the right side of this figure the decoded image are illustrated respectively.

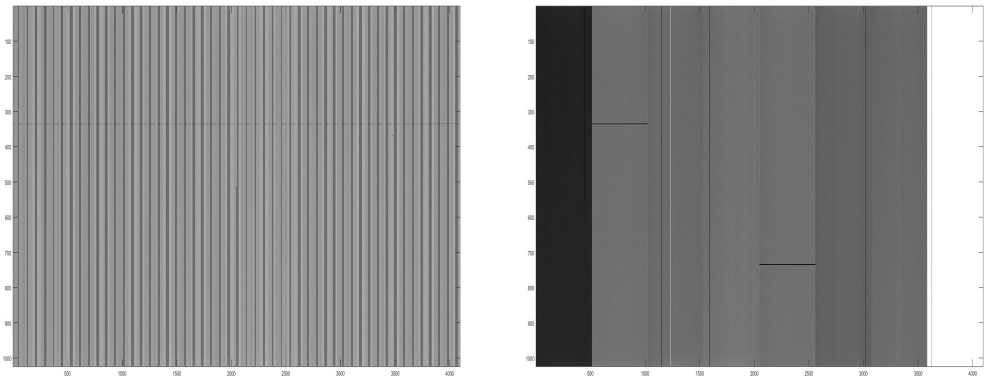

FIGURE 4.3: Offset data collected before and after de-interlacing

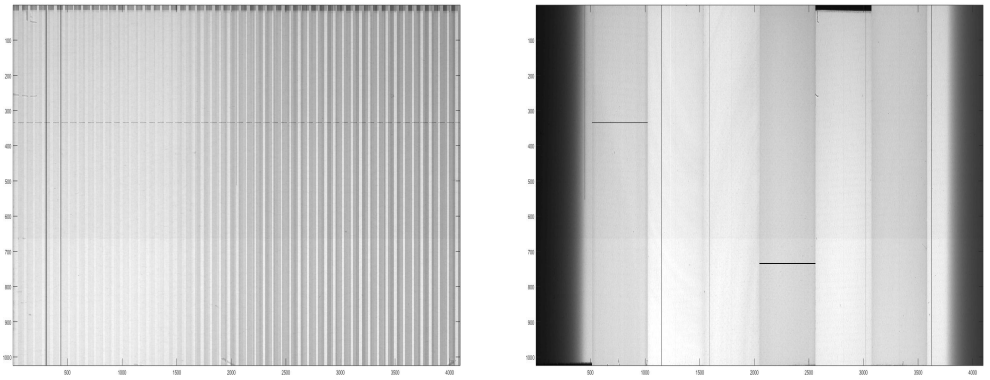

FIGURE 4.4: Gain data collected before and after de-interlacing

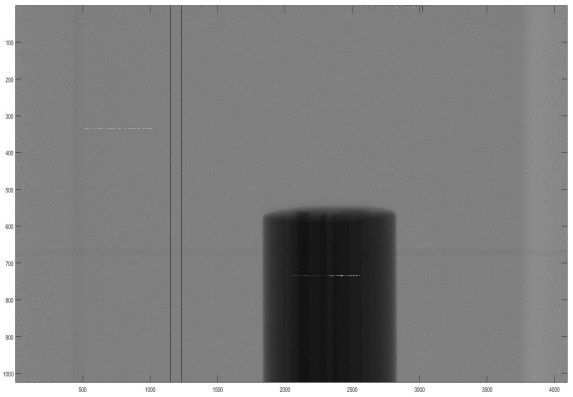

FIGURE 4.5: Corrected projection using gain and offset projections

To correct the raw projections the following formula was used.

$$Corrected\ image = \frac{Raw\ image - Offset\ image}{Gain\ image - Offset\ image} \tag{4.1}$$

To improve the image correction and reduce the statistical noise, several gain data were generated and an average image was derived as the gain image. The offset correction was applied by subtracting the corresponding offset image from the raw image and from gain projections respectively as in equation 4.2.

4.1.3 Image Processing

4.1.3.1 Faulty Pixels Interpolation

Based on our experiment and information provided by the company (see Appendix B.4) there are several rows and columns of sensors which showed a response that was not in concordance with other sensors i.e. they are faulty pixels or they produce lower signal than the rest. These faulty pixels and lines were substituted by interpolation. In our case we used a spline interpolation for replacing defected pixels and lines in the sensors. A MATLAB routine was written for this purpose which corrects all the faulty line and pixels in all 32 detector modules. An example of correction of defected lines is illustrated in figure 4.9. However, there are some noise in the data produced occasionally by the electronic problems and can be fixed electronically. Generally the reason for this error is unknown for us, however, based on our experiments this electronic error is generated by the 5 cm flat cables connecting each single sensor to the electronic board (see white cables in figure 3.5). These cables are soft and fragile which could be easily broken or bent and create inappropriate connection. This type of noise is exemplified in the middle image in figure 4.14. And as it is shown it does not appear in the acquired data of QRM sinogram 4.6.

4.1.3.2 Reordering Data into Sinogram

After collection of a set of projections, the data are then re-ordered in a sinogram matrix of size of M $\times$ N where M is the number of readouts and N is the number of the detectors following the theory of WATCH (see section 2.1). The resulting matrix is the sinogram of non-equal distanced parallel data suitable for the OPED reconstruction algorithm (see bottom of the figure 4.6).

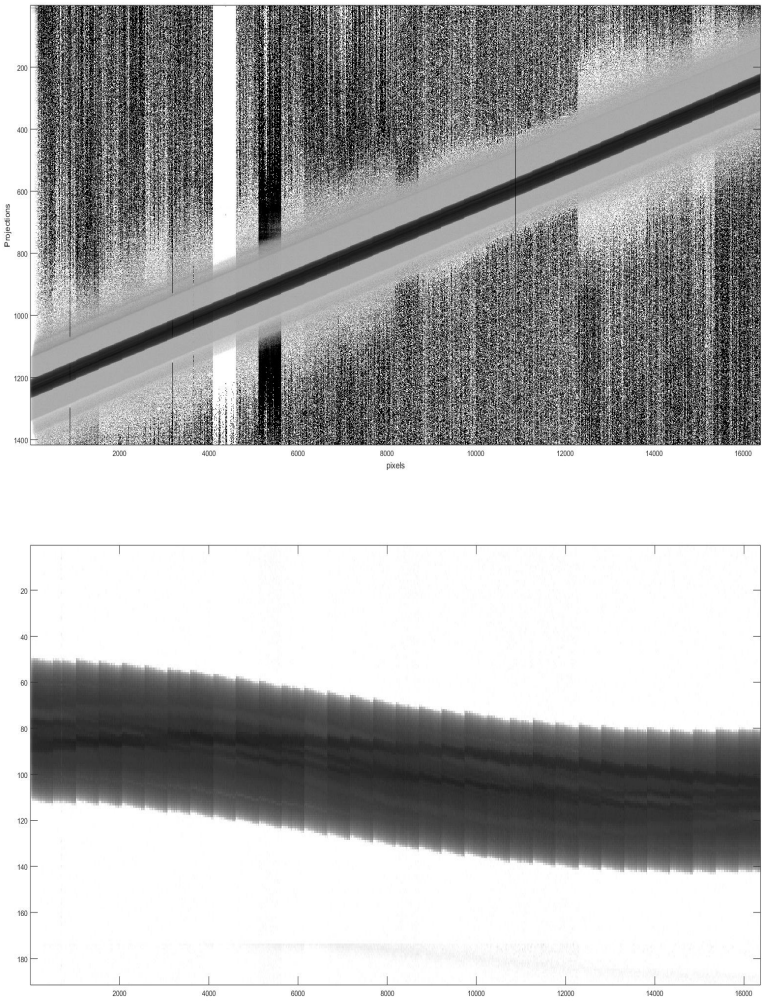

FIGURE 4.6: Top: Data matrix before reordering. Bottom: Sinogram after shifting the data

4.1.3.3 Logarithmation

For reconstruction purposes Radon data R_i are needed to be obtained as the logarithm of the maximum intensity of the source at the detector, divided by the intensity of each pixel:

$$R_i = log(\frac{max(I_i)}{I_i}) \tag{4.2}$$

Where $max(I_i)$ is the maximum intensity received at the detector. It could be calculated either using the data from gain images or the maximum intensity in the obtained sinogram. All these image processing steps are carried out using a MATLAB routine provided for this task.

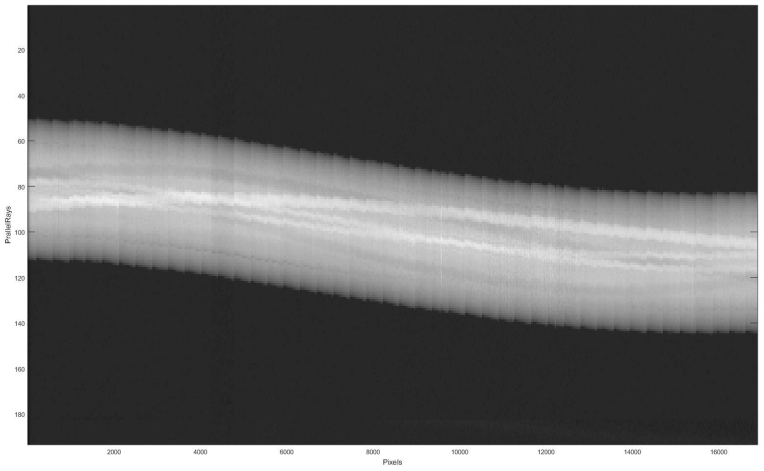

FIGURE 4.7: The obtained sinogram after logarithmation.

4.1.3.4 Image Reconstruction

The prepared sinogram (see figure 4.7) was used as the input for the OPED algorithm [(3)] to reconstruct the image. This program requires the user to provide the sinogram and angle data files which in our case were generated using our MATLAB routine in section 4.2.2.

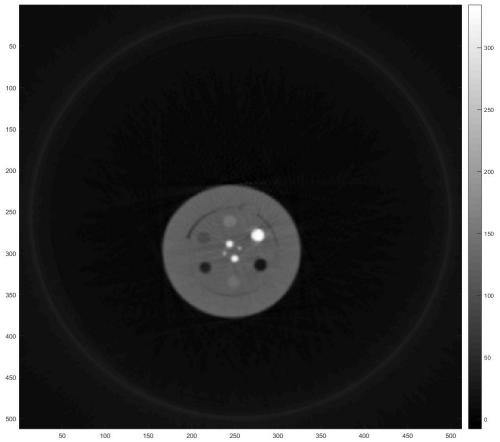

FIGURE 4.8: The reconstructed QRM image using the OPED algorithm.

3. Created on: 11.01.2010, Author: Martin.Lingenheil

4.2 Data Treatment for WATCH System Calibration

4.2.1 Preparing the Calibration Data

To calibrate the WATCH-CT we acquired projections of the conic body at different positioning of the phantom, then, analyzed projections to calculate the apex of cone projection. As an instant, one collected projection is illustrated in figure 4.9. Since each frame grabber was connected to eight X-ray sensors, the data of eight sensors are illustrated in one figure. Afterwards, the projection of the desired sensor was extracted from this data. This is illustrated in the right side of the figure 4.9. But as it is shown, this projection contains defected lines and pixels. This defected lines and pixels could interfere in the edge detection procedure and apex calculation (see figure 4.10), therefore they were fixed using linear interpolation. Later on, the Canny edge detection method was used for evaluation of the cone projection edges.

After properly detection of edges (see the right side of figure 4.10), two lines are fitted to these segments. These lines are shown in red in figure 4.11. The intersection of these lines was considered as the cone projection apex which was indeed the calibration point. This procedure was done for every single position of the cone. Then, collected calibration points were used in the calibration algorithm and evaluation of geometric parameters of the WATCH system.

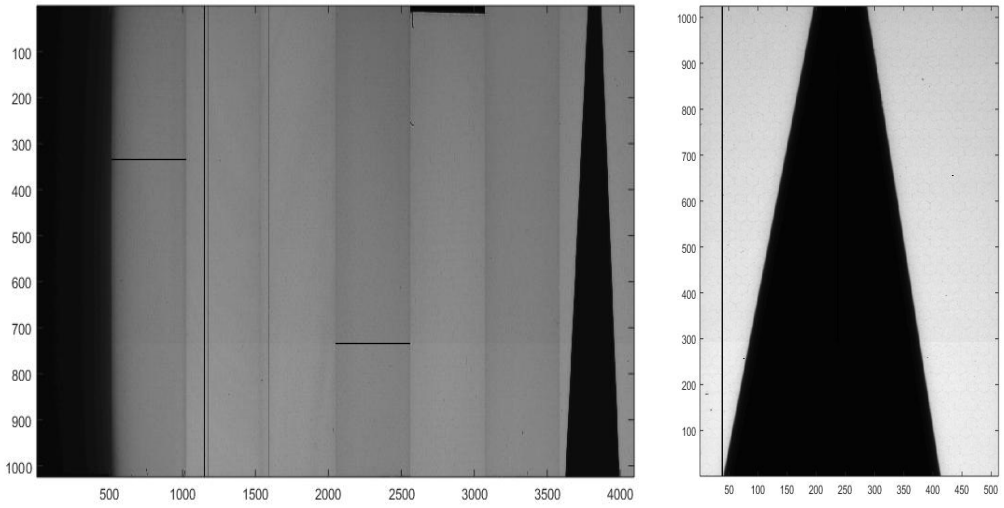

FIGURE 4.9: Left: one frame of the collected projections. Right: the selected senor for calibration which contains the cone projection.

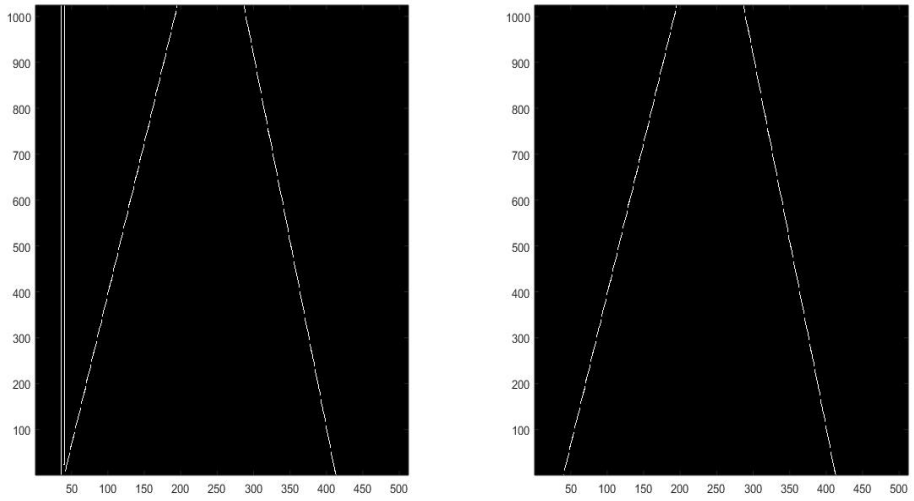

FIGURE 4.10: detected edges of the cone phantom projection, left: before correcting the faulty lines, right: after correction

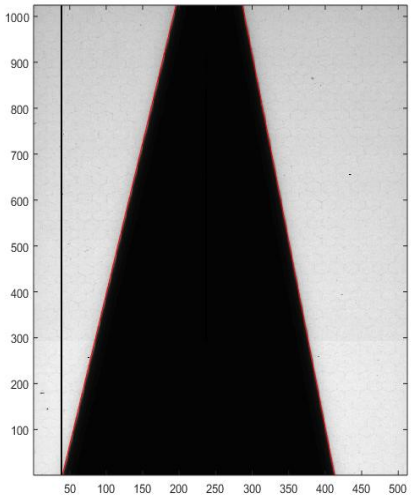

FIGURE 4.11: the edges are plotted in red over the original projection of the cone.

4.2.2 The Geometric Parameters Correction

Following the section 3.3, the detector modules were plotted in the coordinate system of the KUKA robotic arm with some assumptions i.e. the focus is considered to be placed at the center of its rotation axis and the detectors have the same distance from the center of detector ring. Moreover, since all the detector modules are mounted on a same holder then the geometric parameters of several of the sensors were chosen (see table 5.3) for evaluation and parameters of other sensors were calculated based on the chosen measured sensors. Additionally, the calculated angle Gamma for selected detectors is

less than 1° (see table 5.3) therefore, the influence of this angle in image formation was ignored in the geometric correction.

In figure 4.12, the correction idea developed in section 3.3 is illustrated. Black lines indicate misaligned detectors rows which contain the central plane of the system [4] [5] . Blue lines in this figure illustrate the vectors passing through the focus and pixels of an ideally aligned WATCH-CT system. Furthermore, small red circles indicate the intersection point between misaligned and ideal systems. Based on this blue lines we could select the proper pixels i.e. pixels collecting non-equally spaced parallel rays, on the misaligned detectors.

Figure 4.14 shows the sinogram after properly selecting the pixels. This sinogram has smaller size than the original sinogram and consequently shorter reconstruction time. It looks smoother and results in a seemingly same image quality as the one before correction.

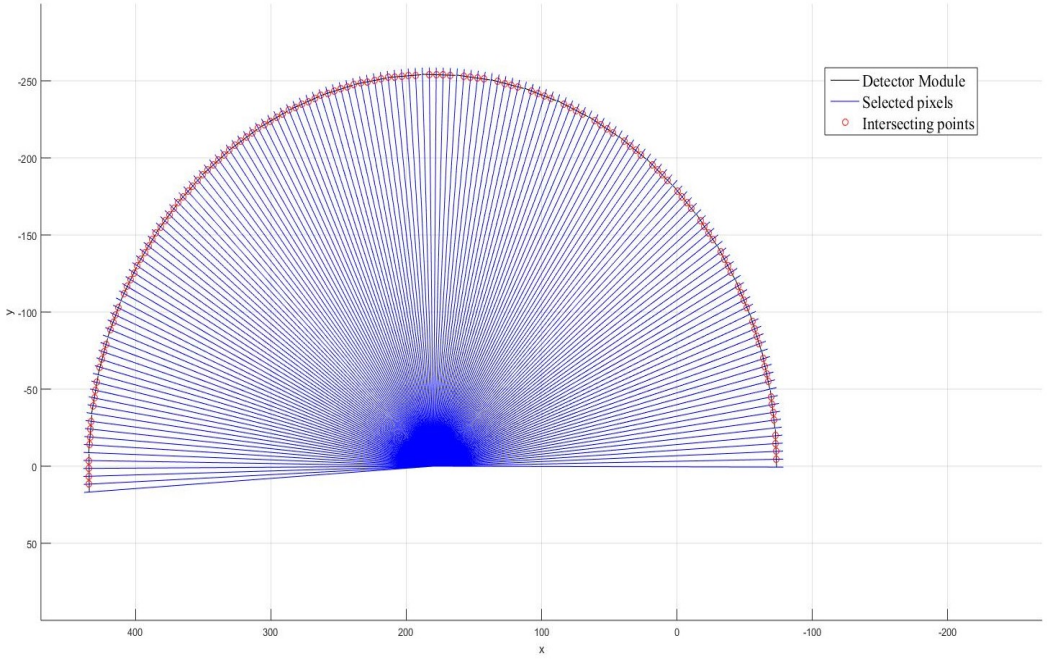

FIGURE 4.12: Simulated detector modules in experimental WATCH system and selected rays.

To summarize the steps followed in the correction procedure after collecting and reordering the data consider the steps below:

- Use the MATLAB program to extract the intersecting points and the angle file.
- Use the information of intersecting points to extract the desired pixels and the new sinogram.

4. Is a plane which contains the focus and it is orthogonal to the rotation axis of the system.
5. This is determined using calibration parameters.

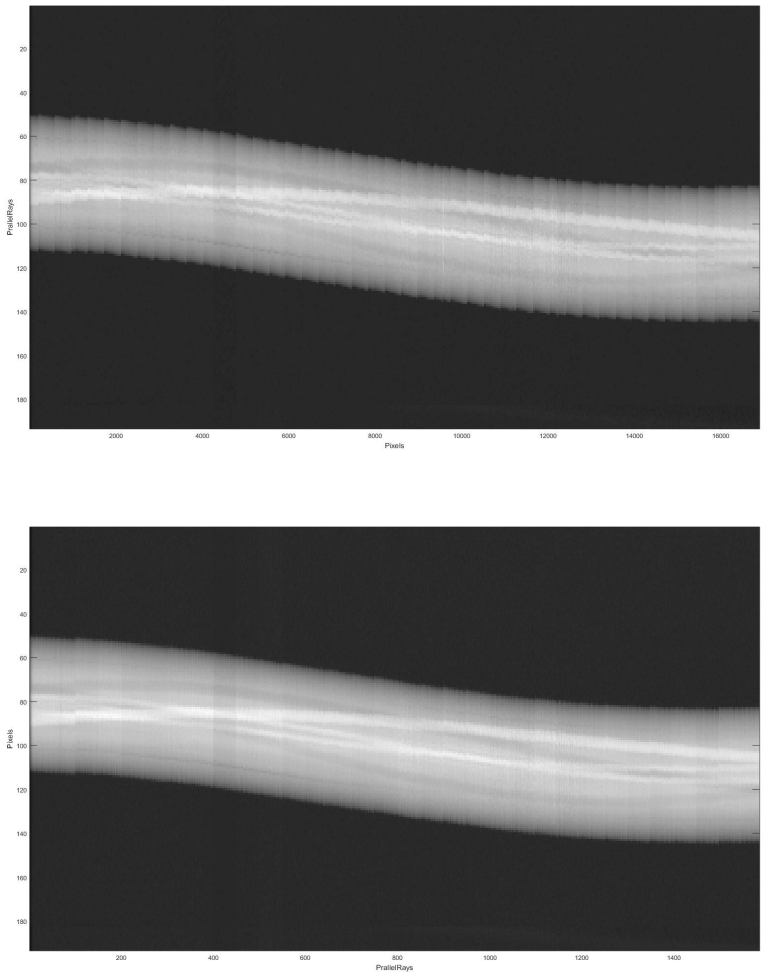

FIGURE 4.13: Top: a full sinogram including all detector pixels. Bottom: sinogram after selecting pixels.

- Give the new sinogram and the angle file as an input to the OPED reconstruction algorithm to reconstruct an image.

4.3 Image Quality Assessment

Two different images of one silicon phantom (see figure 3.14) were employed for the purpose of image quality assessment of the constructed WATCH system. The process of image reconstruction is illustrated in figures 4.15 and 4.16. First, the data matrices were acquired from the system, then the data were shifted, re-ordered and logarithmized to generate the sinogram of the non-equally spaced parallel rays accordingly. Finally, the sinogram was used as the input for the OPED reconstruction algorithm.

The silicon phantom was positioned inside X-ray beam from different sides. You could observe in the right side of the figure 4.14, that the phantom provides a larger homogeneous area for noise power spectrum evaluation.

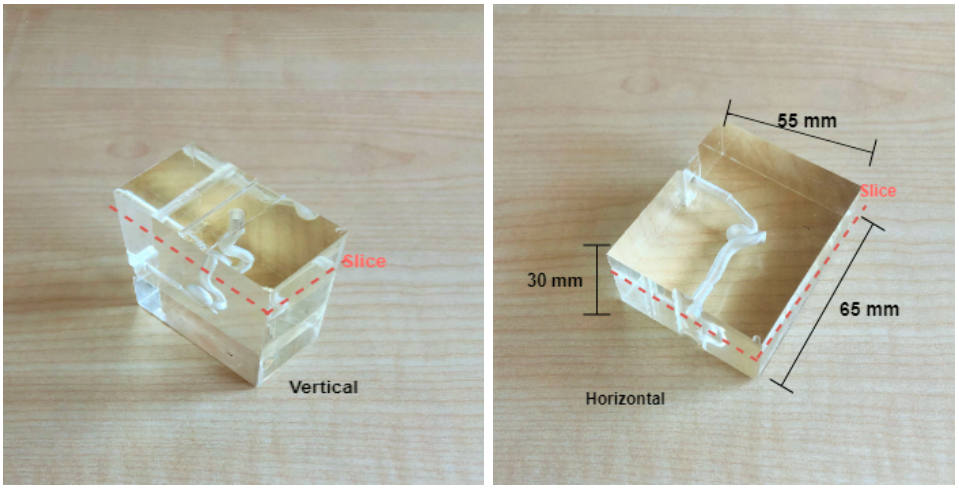

FIGURE 4.14: Left: the phantom positioning used for NPS calculation. Right: the phantom positioning used for MTF calculation. The dashed red lines on the left silicon photos shows the height of the slice that was reconstructed.

Figure 4.16 displays steps of the cuboid image reconstruction required for noise power spectrum calculations. The red square indicates the ROI selected for this evaluation. Additionally, figure 4.15 shows the process of image reconstruction for modulation transfer function evaluation. Following the method described in section 3.7, the edge of the cuboid image was used for ESF and MTF assessment. The result of this evaluation is presented in section 5.4.

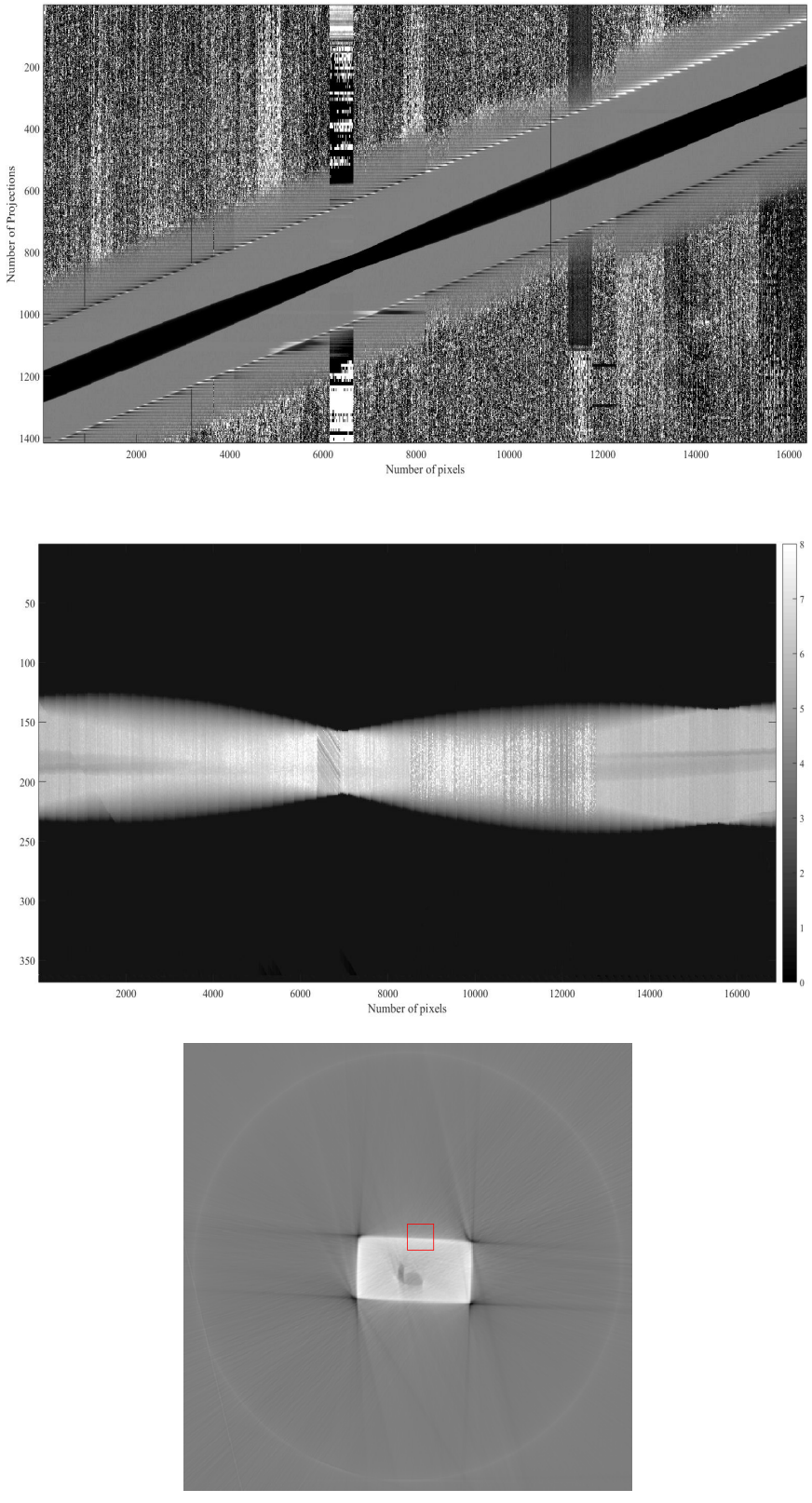

FIGURE 4.15: Top: the data matrix collected for cuboid image reconstruction. Middle: the sinogram after reordering and logarithmation. Bottom: the reconstructed cuboid image using the OPED reconstruction algorithm

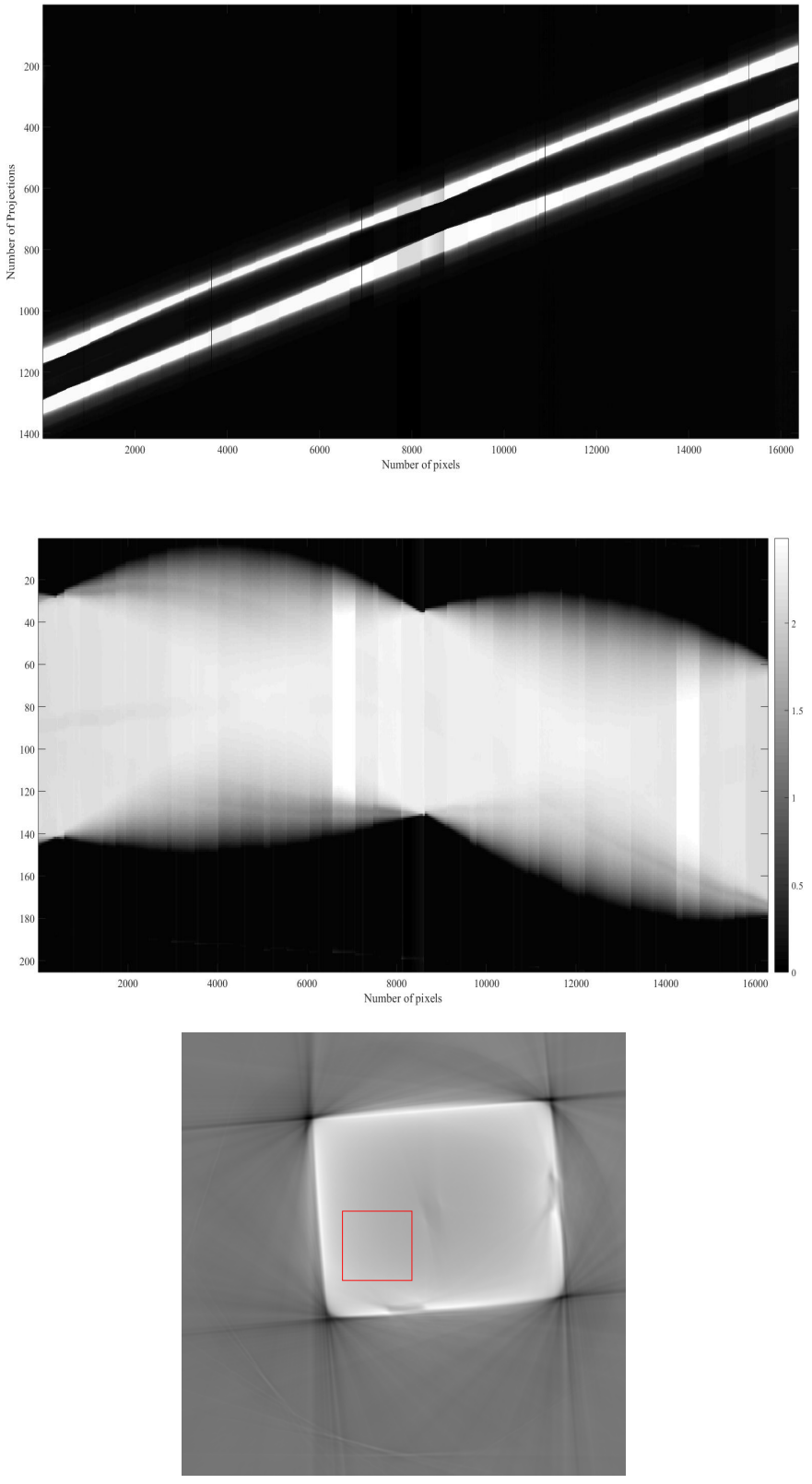

FIGURE 4.16: Top: the data matrix collected for cuboid image reconstruction. Middle: sinogram after reordering and logarithmation. Bottom: the reconstructed cuboid image using the OPED reconstruction algorithm

Chapter 5

Results

In this chapter, the main results of this project are presented, which includes the simulation and experimental results of the second prototype of the WATCH system and a new geometric calibration method. This technique is proposed to calibrate the WATCH imaging system as well as any other scanner system based on the CBCT geometry. The results include:

- Reconstructed images of a robot-driven WATCH-CT. These are presented for both the Mote-Carlo simulation and the constructed prototype system in the X-ray laboratory of OVGU.
- The second part of this chapter presents the results of the verification of the geometric calibration method proposed in this thesis, involving experimental and simulation tasks.
- The last part of this chapter shows the results of the Fourier based image quality assessment on the images reconstructed using the WATCH prototype system and corrected using our proposed calibration method. For this purpose, MTF and NPS were evaluated, based on the method described in section 3.7, using the reconstructed images of a silicon phantom (see figure 4.14).

5.1 The WATCH system Construction Results

One main result of this project is that the second prototype of the newly developed WATCH system is constructed and mounted on a KUKA robotic arm. Moreover, a visually good image has been obtained by utilizing this system. The geometry of the system is based on the collection of the non-equally spaced parallel rays which are ideal

for OPED reconstruction algorithm. Additionally, in contrast to the first prototype system, the object in this prototype is stationary while the X-ray source and the detector system are mounted on a KUKA robotic arm, moving around the object on a circular path.

On the one hand, utilising a robotic arm enables flexible movements of the scanner around the patient, which provides better accessibility to the patient during a medical procedure, but on the other hand, there is a disadvantage of using the robot because it could increase the instability of the system and consequently introduce severe geometric artefact in the reconstructed image. The robotic arm and the micro-CT were adjusted in several steps to finally produce a visually high quality image. The reconstructed slice of the micro-CT phantom is shown in figure 5.1. In this image, the cylindrical inserts of radius 0.5 mm are sufficiently resolved, showing that a good visual image-quality can be reconstructed using the second prototype.

In the reconstruction of these images, several steps were considered. As described in section 4.1, all acquired projections were calibrated using offset and gain images. In the sinogram of pumpkin (see figure 5.2), it is visible that a few of the sensors did not show proper response even after intensity calibration. However, the detector response improved (see section 4.1.3.1) during data acquisition of other phantoms i.e. the micro-CT phantom. The corresponding sinogram is shown in figure 5.1, where all the pixels are properly calibrated in terms of the intensity.

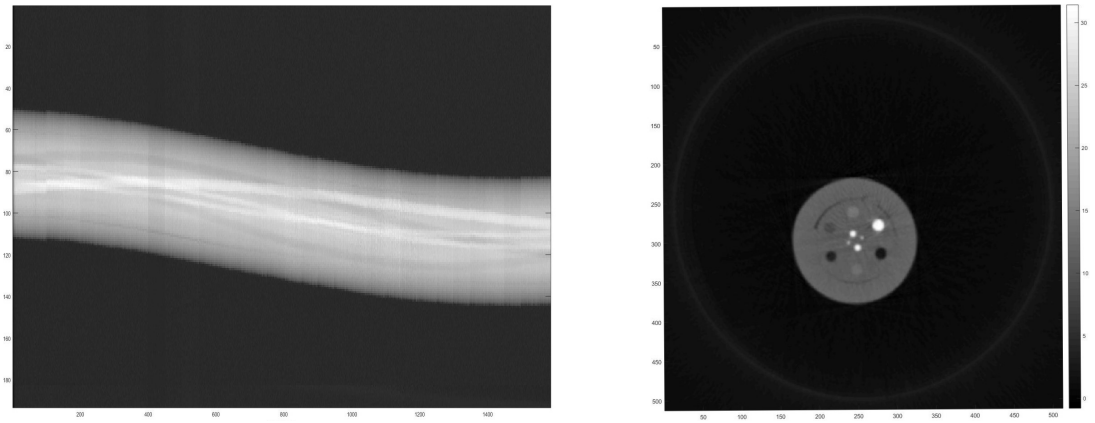

FIGURE 5.1: Left: the sinogram of the QRM micro-CT phantom after applying the correction step. Right: the reconstructed image of the micro-CT phantom.

5.1.1 The Image Reconstruction of Other Phantoms

Following the process described in section 4.1, we carried out scans of an organic phantom (see the left side of figure 5.3), a tantalum sheet (see the right side of figure 5.3), and a cuboid silicon phantom. We then constructed the sinogram and carried out the

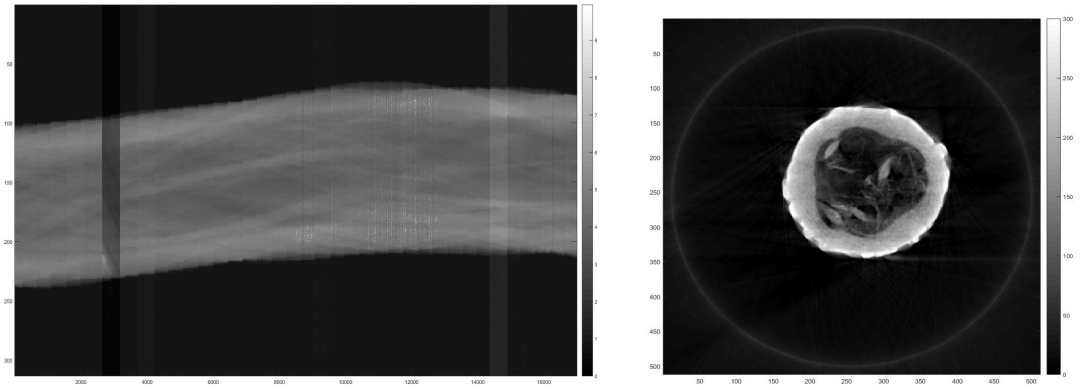

FIGURE 5.2: Left: sinogram of a pumpkin phantom obtained from 1D pixel data. Right: reconstructed image of a pumpkin phantom.

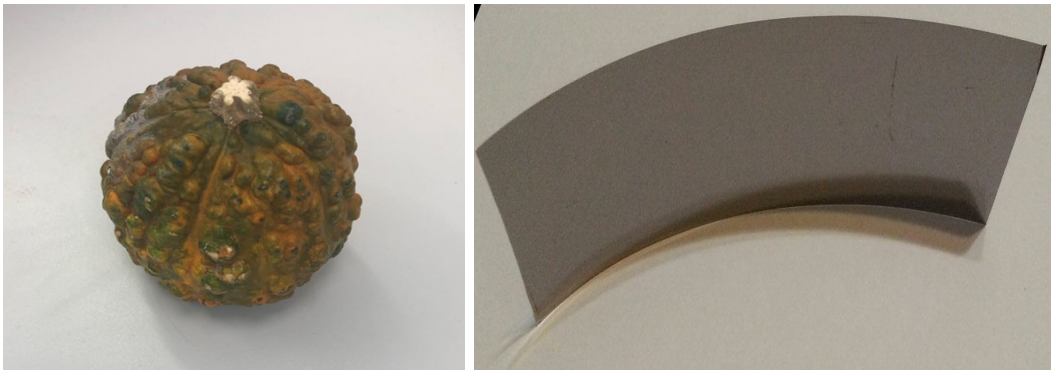

FIGURE 5.3: Left: Pumpkin phantom used in this study. Right: 0.02 mm tantalum sheet.

image reconstruction using the OPED algorithm. In figure 5.2, the obtained sinogram and reconstructed image of the organic phantom are illustrated. Figure 5.3 shows the reconstructed image of the tantalum sheet. A slit image is more likely to introduce streaks which worsen the uniformity of the image. Therefore, optimal reconstruction

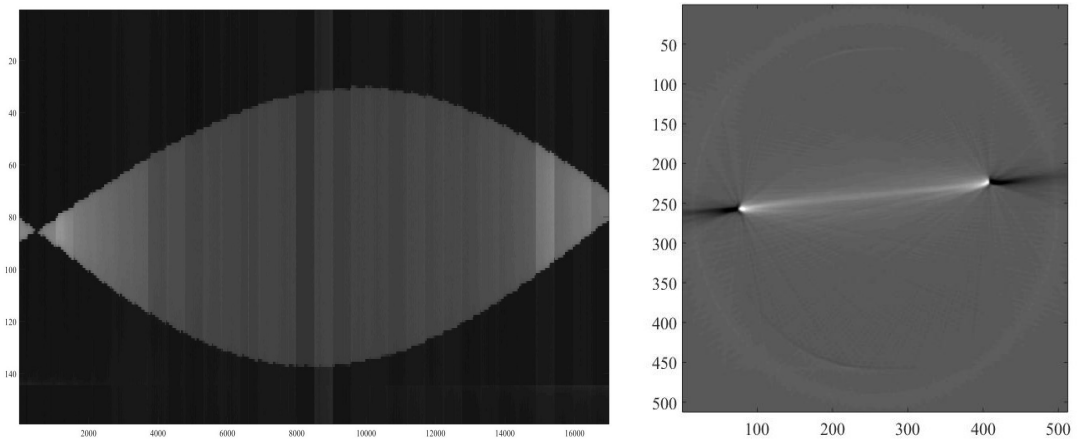

FIGURE 5.4: Left: sinogram of a 0.02 mm tantalum sheet obtained from 1D pixel data. Right: reconstructed image of a slice of a 0.02 mm tantalum sheet.

parameters are required to keep a balance between uniformity, resolution and artefacts. All the images are reconstructed with a size of 512*512 using the OPED algorithm. The geometry correction, as described in section 4.2.2, was applied for the generation of these images. Reconstructed images can be seen to show the ability of the prototype system to produce images with high and low absorption coefficients.

5.2 Calibration Simulation Results

In this study, two micro-CT systems with different parameters were simulated. The first system is simulated with parameters of a micro-CT with a larger detector area to evaluate the accuracy of the method without the limitation of the detector size, which could affect the Δ value i.e. the distance between calibration points. The second scanner system is simulated based on the parameters of the WATCH-CT constructed in our X-ray laboratory. The initial parameters and results of the system calibration, using the calibration method developed in our group, are given in table 5.1 and 5.2. In these simulations, we have assumed a fixed detector setup while the X-ray source and the calibration setup are placed on a rotation table. In this setup first, a reference coordinate system was defined as $Oxyz$ with the z-axis coinciding with the rotation axis and the x-axis was assumed to be perpendicular to the detector, located at the centre of the detector. Afterwards, the displacement in detector and focus spot position in which the center of detector and focus spot where translated to $R = (R_x, R_y, R_z)$ and $F = (F_x, F_y, 0)$ respectively. Finally, the detector was tilted around u-axis and its center with angle β and γ respectively.

In this investigation, a novel calibration phantom was used instead of a conventional phantom, i.e. high-density balls. The apex of a high-density cone object's projection resembles a calibration point. The problem with a ball phantom is that its shadow is an ellipse and the center of the ball lies neither at the focus nor at the center of the ellipse, which reduces the evaluation precision of the calibration point. Unlike the ball phantom, a cone object could project a triangle area with its defined boundaries (see section 3.2.4), which results in a more precise point object.

The focus of this project was on the calibration protocol described in section 3.6. Therefore, a cone-shaped high-density lead phantom was simulated and placed at seven different positions using the Geant4 toolkit [GAea03] and seven projection of the cone were generated. The distance between points, i.e. Δ, was 40 mm. Table 5.1 shows calibration results of the simulated micro-CT with large detector system, as described in section 3.4. Residual values in table 5.1 indicate that for a typical CBCT scanner, the parameters are evaluated with a good accuracy, i.e. within a pixel size which was 100 μm.

TABLE 5.1: Geometric parameters and calibration results for a simulated micro-CT

Parameters	$F_x[mm]$	$F_y[mm]$	$\beta[°]$	$\gamma[°]$	D[mm]
Actual	101	1	-5	4	150.4254
Measured	100.9906	0.9993	-4.9942	4.0090	150.425
Residual	-0.0094	0.000	0.0057	0.009	-0.0045

Parameters	$x_0[mm]$	$y_0[mm]$	$R_x[mm]$	$R_y[mm]$	$R_z[mm]$
Actual	1.0	0.0	-50.0	1.0	0.0
Measured	1.004	0.0	-50.0142	1.0856	0.113
Residual	0.0044	0.0	-0.0142	0.0856	0.113

The results for smaller micro-CT calibration was repeated and the averaged value was calculated. Due to the reduction of the detector size and, consequently, the size (50x25 mm) of the conic body used as a calibration phantom, the accuracy of the calibration method also decreases.

Table 5.2 presents calibration results of the simulated micro-CT, which has similar parameters to that of the WATCH system constructed in our X-ray laboratory. Even with the small size of the detector modules, the calibration method exhibits reasonably good results. The main source of the error in this calculation is the smaller detector size, which result in less information of the projected phantom and thus a shorter Δ (see section 3.2). The influence of measurement errors is discussed in detail in [TNH19].

TABLE 5.2: Geometric parameters and calibration results for a simulated micro-CT similar to WATCH system

Parameters	$F_x[mm]$	$F_y[mm]$	$\beta[°]$	$\gamma[°]$	D[mm]
Actual	186	1	-5	4	250.0448
Measured	185.9037	0.4772	-4.5999	3.8732	249.9452
Residual	-0.0963	-0.522	0.400	-0.1267	-0.1048

Parameters	$x_0[mm]$	$y_0[mm]$	$R_x[mm]$	$R_y[mm]$	$R_z[mm]$
Actual	-4	0	-65.0	0.0	0.0
Measured	-3.9431	0.0107	-64.9580	0.1644	0.3730
Residual	0.0568	0.0107	0.0419	0.1644	0.373

5.3 Calibration Experimental Results

Our calibration method was implemented on the second prototype of the WATCH-CT system mounted on a KUKA robotic arm, and is described in the following paragraphs.

The calibration procedure described in section 3.2 was implemented for eight sensors out of thirty-two. Accordingly, first, a reference coordinate system was defined as $Oxyz$ for each detector where its z-axis coincides with rotation axis and its x-axis was assumed to be perpendicular to the detector, located at the center of the detector ideally. The calibration setup was then placed between the source and the detector. The calibration setup contains three-axis translation stages mounted on a rotation stage which resembles the $Otsh$ coordinate system. The whole setup was then placed on a tripod (see figure 3.24). Projections of a high-density cone phantom (see figure 3.25) were generated at different positions of the cone body for each detector and apexes of cone projections were evaluated, which were used for the geometric parameter calculation using a MATLAB routine. The distance between calibration points Δ was set to 7 mm, and the size of the pixel was about 0.04804 mm. Results of this experimental work are given in table 5.3.

TABLE 5.3: Geometric parameters and calibration results for selected sensors, calculated experimentally using the second prototype of the WATCH-CT

Sensor No.	$F_x[mm]$	$F_y[mm]$	$\beta[^\circ]$	$\gamma[^\circ]$	D[mm]	$P_u[mm]$	$P_v[mm]$
1	183.6559	6.482	-7.2972	-0.337	264.832	-8.2769	-61.9079
3	187.2167	12.77268	-7.4554	0.519	266.354	16.7396	-40.5078
4	183.5774	9.0152	-4.87972	0.6637	262.2397	12.5329	-40.98608
5	185.61728	19.16986	-5.574142	0.48502	265.832	26.9749	-41.82016
6	184.4887	7.7362	-7.84127	0.5037	264.832	10.1036	-36.9632
20	186.3515	-25.6518	-4.4627	-0.4162	262.8973	-35.5828	-37.2637
25	183.8469	-17.3236	-5.7958	-0.83559	265.8558	-25.2989	-34.8014
32	187.3717	-7.9015	-4.6943	-0.3027	264.28	–10.32118	-38.9986

Sensor No.	$x_0[mm]$	$y_0[mm]$	$z_0[mm]$	$R_x[mm]$	$R_y[mm]$	$R_z[mm]$
1	11.835	-0.4546	44.2837	-89.94278	3.047	27.7313
3	-0.4221	0.2295	28.2262	-82.1217	-4.3333	5.4523
4	5.064	-0.3195	40.2493	-81.1856	-3.9916	18.3828
5	1.3012	-0.3252	30.12231	-81.0355	-7.9633	6.6413
6	1.15688	-0.9673	23.7377	-77.6881	-2.7796	-2.4843
20	-2.2011	-0.5262	41.3291	-78.6281	10.2008	16.4357
25	0.9363	0.4888	31.7115	-84.1266	8.4801	7.4055
32	-0.4741	0.0074	37.729	-79.2089	2.6254	17.1844

In table 5.3, $\sqrt{F_x^2 + F_y^2}$ is the distance from the iso-center to the focus spot, β and γ are the rotation around the y and x-axis, respectively, D is the source to detector distance, P_u and P_v are the coordinates of the projection of the focus onto the detector in the detector coordinate system, R_x, R_y and R_z are the coordinates of the detector center in the reference coordinate system and x_0,y_0 and z_0 are the coordinates of the calibration point in the reference system. The values in table 5.3 and the correction method, proposed in section 3.3, were employed to select the pixels. Since the value of the measured angle γ was less than 1°, we ignored the influence of this angle tilt on reconstructed images. Moreover, we assumed that the focus spot is located at its ideal position (see figure 3.21). In the robot program the radius R is set to 180 mm, which indicates the distance from the X-ray source rotation axis E1 (see figure 3.1), of the robot to the iso-center, which is in fact $\sqrt{F_x^2 + F_y^2}$ in the calibration parameters. Using these values, one can evaluate the correct position of the focus spot (see section 3.3). In addition, the values of x_0,y_0 and z_0 could be utilized for the fine geometry calibration, i.e. gaps between modules and pixels, as given in [Hol09].

Figure 5.5 shows two images of the pumpkin phantom, before and after the geometric correction. Two images are reconstructed with the same size of 512×512 and they are displayed with the same gray values. This indicates that taking into account the calibration parameters, presented in table 5.3, improves the visual image quality and demonstrate that the calibrated method proposed in this paper is efficient.

5.4 Image Quality Assessment Results

The modulation transfer function and the noise power spectrum were determined for the second prototype of the new scanning geometry, under the calculation parameters setup as discussed in section 3.7. Two images of the cuboid phantom (see figure 4.14) were reconstructed for the quantitative image quality assessment of the second prototype.

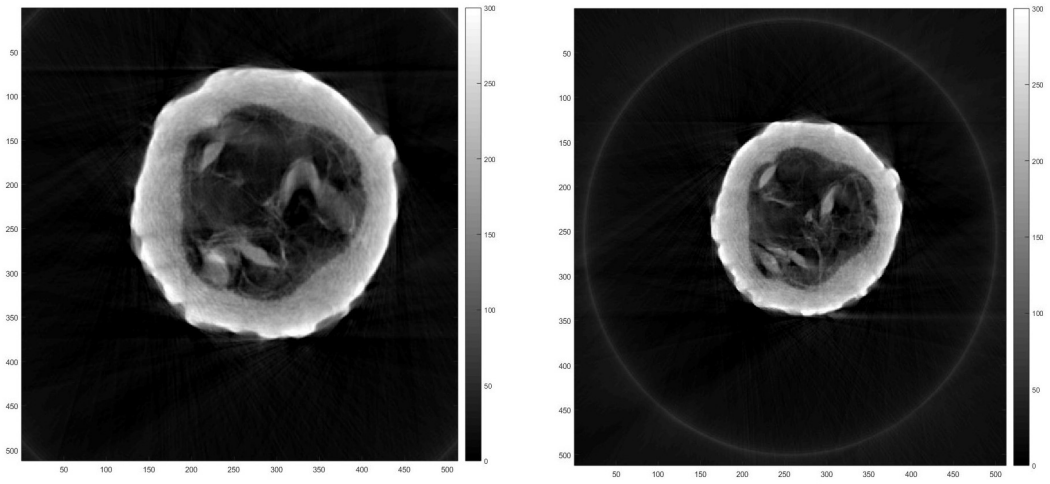

FIGURE 5.5: Pumpkin image reconstruction. Left: Before geometric correction. Right: after geometric correction.

The MTF was evaluated based on the work of [FTT+92] and [ESU03] as discussed in section 3.7. For this purpose an IDL program was written. (1) This program calculated the average ESF which is an advantage for noisy images. As a result, figure 5.6 shows the estimated spatial resolution of the second prototype. Red squares indicate measured values of the MTF and red lines are joining the points. The nyquist limit was determined using the reconstruction pixel size. Noise characteristics of the second prototype have been assessed using an IDL program (2) and based on the methodology described in section 3.7. The noise power spectrum results are shown in figure 5.7. The uncertainties of results are discussed in the next chapter.

1. MTF-Kante Version 5.1, E. Buhr, (H. Illers, modified by M.Greiter,HMGU) PTB, 2003-04-24/2008-04-08'

2. This IDL program (HEAD-NPS-V5) is the heading program designed for NPS evaluation of images according to the latest revision of IEC62220-1 (2002-08-21) [ESU03] [Ill05]

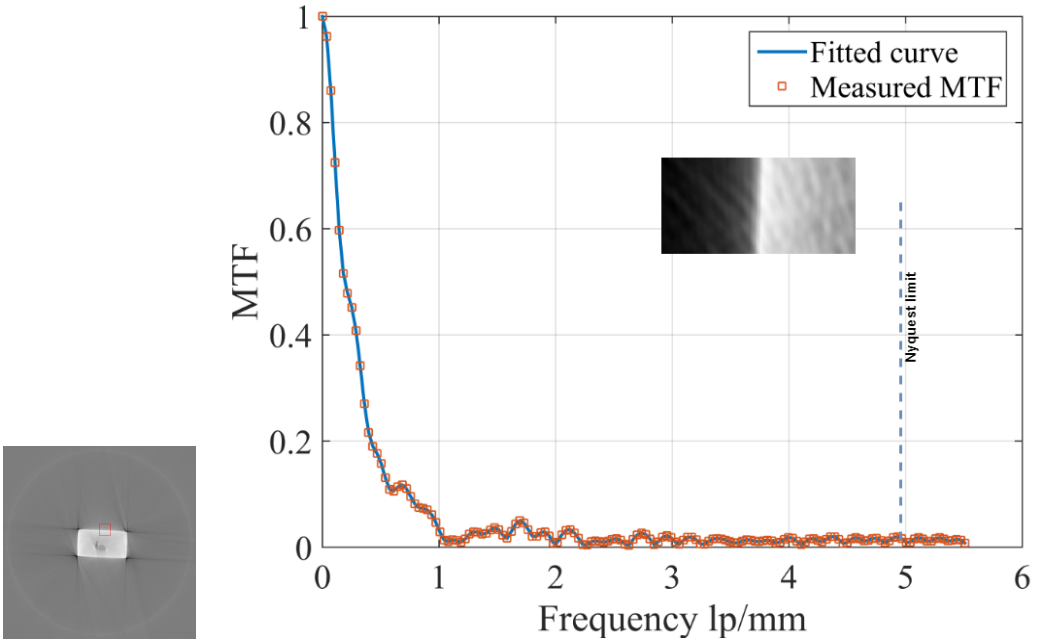

FIGURE 5.6: Modulation transfer function calculated for the experimental WATCH system, using the region (Red ROI box) from the reconstructed image of the cuboid phantom.

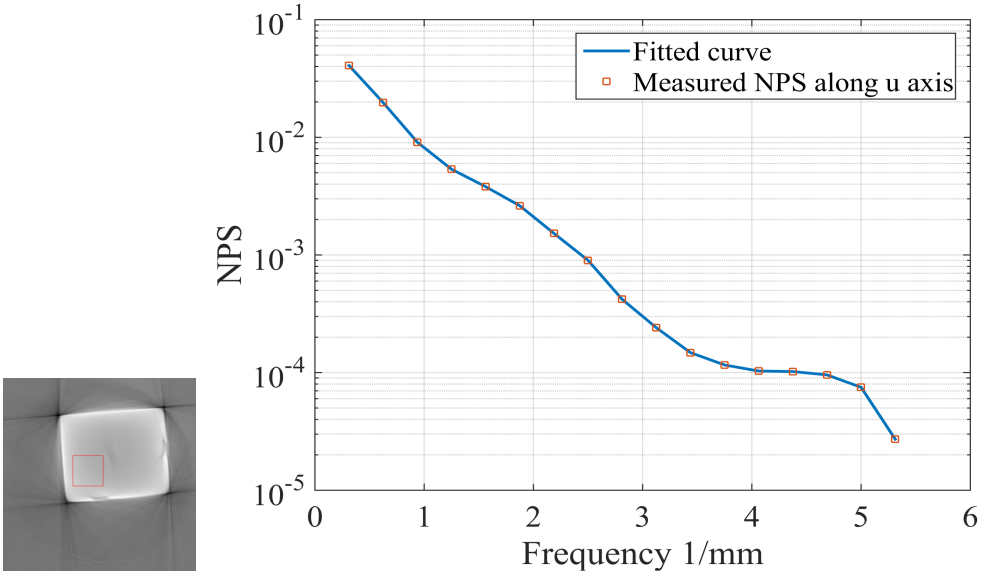

FIGURE 5.7: Noise power spectrum calculated for experimental WATCH system, using the region (Red ROI box) from the reconstructed image of the cuboid phantom.

Chapter 6

Discussion and Outlook

In this chapter, we discuss the results obtained in this project and recommend suggestions for improvement of the system.

We have demonstrated the imaging capabilities of the second prototype of the WATCH-CT. This newly developed robot-driven geometry can collect the non-equally spaced parallel data, which are ideal for the OPED reconstruction algorithm. The WATCH scanning geometry enables an efficient data collection which potentially could reduce the patient exposure.

Moreover, we have proposed a new geometric calibration method which could be used to calculate the geometric parameters of the WATCH-CT as well as a cone-beam micro-CT. This has been proven by simulation and experimental results, as shown in the previous chapter (see section 5.3).

6.1 Suggestions for an Improved Prototype

6.1.1 The WATCH System Construction

The second prototype of the WATCH system, constructed in our X-ray laboratory, has advantages and disadvantages in comparison to the first prototype, and there are some aspects which can be improved in the second prototype.

Advantages of the new prototype are mainly due to the construction of the system. The prototype system is mounted on a robotic arm and enables the movement of the detector and the X-ray source around the object, while the object is stationary. The scanning construct of the new prototype is, therefore, opposite of the first prototype where the

object moves while the X-ray source and the detector remain stationary. Consequently, the new configuration could reduce the motion artefact [(1)] in the image. At the same time, this configuration results in a disadvantage due to the increment of the geometric instability in the system which, consequently, results in more geometric artefacts in the reconstructed image. The robotic arm enables different implementation of geometries i.e. WATCH and conventional-CT geometries, as well as more flexible positioning of the system which is essential for interventional radiology [(2)] .

The robotic arm enables different implementations of the scanning geometries, i.e., the WATCH and the conventional-CT geometries. Moreover, it offers enhanced flexibility in the positioning of the system, which is essential for interventional radiology.

One major benefit of the newly constructed prototype system is that it also enables three-dimensional imaging by employing small flat panel detectors installed along the detector ring (see figure 3.7), which was not possible with the first prototype.

6.1.2 Design of the Ring

In the construction of the detector ring, there are several parts which are connected using screws. Despite great care, adjusting all pieces to form one uniform detector ring was not possible and, therefore, we suggest building the whole detector structure in one piece. [(3)] . It should be noted that only the outer holder structure (see left side of figure 3.8) could be changed and the sensors holders (see figure 3.5) could remain as they are.

6.1.3 Read-out Design

The speed of the system is slow at the moment which is mainly due to the limited frame rate of the detector system, i.e., about 1.6 sec per frame grabber, and also due to the acquisition system used for the frame grabbers.Parallel data collection, i.e., calling four frame grabbers simultaneously, is not possible using the actual system and only series data collection is enabled, both in the PC and the provided software.

Note: It should be noted that for parallel data acquisition, both hardware and software need to be developed otherwise, the frame grabber is overwritten and results in hardware crashes.

1. Motion artifact is a patient-based artifact that occurs with voluntary or involuntary patient movement during image acquisition. Misregistration artifacts, which appear as blurring, streaking, or shading, are caused by patient movement during a CT scan [Hsi03].
2. Is a type of minimally-invasive diagnosis and treatment which employs the radiology images during the surgery to minimize the patient risk [Internet]
3. This was not possible in our workshop because the whole ring did not fit into the cut machine.

6.2 Image Reconstruction

Phantoms representing high and low X-ray absorption were imaged to investigate the visual contrast differentiation ability the constructed system. In the reconstructed images the geometric artefact is still visible, due to the approximations carried out during the correction process.

The reconstructed images show good contrast resolution. Black streaks at sharp object edges (shown in figure 5.3 and 4.16) are mainly due to the beam hardening [(4)] and high absorbing artifacts [(5)] . Aliasing artefact [(6)] also appear in reconstructed images due to the under sampling of the object.

6.3 Micro-CT Geometric Calibration Method

This thesis addresses a new "mathematically exact" method to calibrate the gross geometric parameters of a cone-beam micro-CT with high accuracy. This technique can calculate all geometric parameters necessary for geometric calibration by acquiring only two projections at angles 0° and 180°. The proposed method is theoretically exact, accurate, compact i.e. only projections of seven balls are required, no adjustment between the phantom and the rotation table is needed.

Moreover, a novel calibration object was introduced and tested in this project which could, in general, improve the geometric calibration method and substitute the phantoms with small balls [TnH17] (see section 3.2.4).

This method provides precise information about the point object position in space within a pixel size accuracy. Using this information, gaps between the pixels and detector modules could be calculated, employing the idea proposed by [Hol09]. This information is important for the calibration of polygonal detector systems.

The calibration method, specifically for WATCH system mounted on a robotic arm, requires some robotic programming background. Moreover, for the first calibration of the system, the calibration angle for each detector modules needs to be found and saved in the robot software. This information could be used later for repeating the calibration of the same system. Therefore, the calibration time will be reduced significantly.

4. Beam hardening artefact is produced when polychromatic X-ray beam passes through an object, lower energy photons are attenuated more readily than higher energy photons, causing the edges of the object to appear brighter than the center, even if it is made of a homogeneous material [JN04]

5. Streak artifact which occurs in highly attenuating areas such as edges.

6. An insufficiency of data may occur either through under-sampling of projection data or due to insufficient number of collected projections. The inadequacy of data usually results in distortions known as the aliasing artefact [KS01].

The experimental calibration results, as given in table 5.3 could be affected by different factors such as human error while using the translation stages. In addition, the accuracy of the translation stages and repeatability of the KUKA robot path are limited to 0.010 mm and 0.060 mm, respectively. Furthermore, the focus spot size could influence the cone projections and, therefore, the accuracy of the cone projection apex. Nevertheless, by repeating the geometric calibration for each detector and averaging the results, we can improve the results of the geometric parameters.

6.4 Image Quality Assessment

The visual quality of the reconstructed images is reasonably good given that they are obtained with about 1100 projections and 193 rays per view, in the case of the QRM micro-CT phantom. The optimization of the system is a no-end task. The image quality could be improved by increasing the number of projections, careful geometric adjustments, and optimization of the system.

Pixel inhomogeneities appearing in the image (bright and dark regions in figure 4.16) are due to the beam hardening effects since no filter was applied during the data acquisition of this image. This was investigated by our previous simulation study [SkKM+18]. Beam hardening influences the NPS curve as it has been compared for no-filter and filtered situations in [JN04]. The uncertainties associated with MTF includes conversion of irregular to regular over-sampling grid (see section 3.7), the penumbra area produced by scatter radiation, the effect of using an inadequate ESF, and the influence due to the assumption of a linear system. The uncertainties observed in NPS mainly include statistical uncertainties which could be calculated using pixels values and the parameter settings employed for evaluation. [Ill05].

Appendix A

A.1 Deriving analytical expressions for F_x, F_y, x_0, y_0 and z_0.

For derivation of parameters F_x and F_y and the point $p_0 = (x_0, y_0, z_0)$ one can use rewrite the equations 3.13 - 3.15 in $Oxyz$ reference coordinate system.

$$\begin{pmatrix} F_x - x_0 \\ F_y - y_0 \\ -z_0 \end{pmatrix} = \frac{1}{T_0}(\Gamma B)^T \begin{pmatrix} D \\ P_u - u_0 \\ P_v - v_0 \end{pmatrix} \tag{A.1}$$

This could be extended to the point $p_1 = (-x_0, -y_0, z_0)$ which is symmetric to the point p_0 with respect to axis Oz. Then also following equation is valid:

$$\begin{pmatrix} F_x + x_0 \\ F_y + y_0 \\ -z_0 \end{pmatrix} = \frac{1}{T_1}(\Gamma B)^T \begin{pmatrix} D \\ P_u - u_1 \\ P_v - v_1 \end{pmatrix} \tag{A.2}$$

By subtraction of equations A.1 and A.2 following expression are obtained:

$$2x_0 = \frac{Dcos(\beta)}{T1} - \frac{Dcos(\beta)}{T0} - \frac{cos\gamma sin(\beta)(P_v - v_0)}{T0} + \frac{cos\gamma sin(\beta)(P_v - v_0)}{T1} - \frac{sin(\beta)sin(\gamma)(P_u - u_0)}{T_0} + \frac{sin(\beta)sin(\gamma)(P_u - u_0)}{T_1} \tag{A.3}$$

$$2y_0 = \frac{cos\gamma(P_u - u_0)}{T_1} - \frac{cos\gamma(p_u - u_0)}{T_0} + \frac{sin\gamma(P_v - v_0)}{T_0} - \frac{sin\gamma(P_v - v_0)}{T1} \tag{A.4}$$

$$0 = \frac{Dsin\beta}{T_0} - \frac{Dsin\beta}{T_1} - \frac{cos\beta cos\gamma(P_v - v_0)}{T_0} + \frac{cos\beta cos\gamma(P_v - v_0)}{T_1} - \frac{cos\beta sin\gamma(P_u - u_0)}{T_0} + \frac{cos\beta sin\gamma(p_u - u_0)}{T_1} \tag{A.5}$$

and by summation of equations A.1 and A.2 we yield in:

$$2F_x = \frac{Dcos\beta}{T_0} + \frac{Dcos\beta}{T_1} + \frac{cos\gamma sin\beta(P_v - v_0)}{T_0} + \frac{cos\gamma sin\beta(P_v - v_0)}{T_1} + \frac{sin\beta sin\gamma(P_u - u_0)}{T_0} + \frac{sin\beta sin\gamma(P_u - u_0)}{T_1} \tag{A.6}$$

$$2F_y = \frac{cos\gamma(P_u - u_0)}{T_0} + \frac{cos\gamma(P_u - u_0)}{T_1} - \frac{sin\gamma(P_v - v_0)}{T_0} - \frac{sin\gamma(P_v - v_0)}{T_1} \tag{A.7}$$

$$-2z_0 = \frac{cos\beta cos\gamma(P_v - v_0)}{T_0}\frac{Dsin\beta}{T_1} - \frac{Dsin\beta}{T_1} - \frac{Dsin\beta}{T_0} + \frac{cos\beta cos\gamma(P_v - v_0)}{T1} + \frac{cos\beta sin\gamma(P_u - u_0)}{T_0} \tag{A.8}$$

Also, using equations 3.31 - 3.34 leads in geometric parameters calculation expressions:

$$x_0 = \frac{1}{2}(\frac{1}{\|C\|} - \frac{1}{\|c\|})\frac{1}{cos\beta} \tag{A.9}$$

$$y_0 = \frac{1}{2}(\frac{U_0}{\|c\|} - \frac{U_1}{\|C\|}) \tag{A.10}$$

$$z_0 = \frac{\Delta}{2}[(\frac{1}{\|C\|} + \frac{1}{\|c\|})sin\beta - (\frac{V_1}{\|C\|} + \frac{V_0}{\|c\|})\frac{cos\beta}{D}] \tag{A.11}$$

$$F_x = \frac{\Delta}{2}[(\frac{1}{\|C\|} + \frac{1}{\|c\|})cos\beta - (\frac{V_1}{\|C\|} + \frac{V_0}{\|c\|})\frac{sin\beta}{D}] \tag{A.12}$$

$$F_y = \frac{\Delta}{2}(\frac{U_0}{\|C\|} + \frac{U_1}{\|c\|})\frac{1}{cos\beta} \tag{A.13}$$

A.2 Derivation of γ and β angles

Two matrices Ω_0 and Ω_1 could be written as follow:

$$\Omega^0 = \begin{pmatrix} \alpha_{x,t}cos\beta - \alpha_{z,t}sin\beta & \alpha_{x,s}cos\beta - \alpha_{z,s}sin\beta \\ \alpha_{y,t}cos\gamma + \alpha_{z,t}cos\beta sin\gamma + \alpha_{x,t}sin\beta sin\gamma & \alpha_{y,s}cos\gamma + \alpha_{z,s}cos\beta sin\gamma + \alpha_{x,s}sin\beta sin\gamma \\ \alpha_{z,t}cos\beta cos\gamma - \alpha_{y,t}sin\gamma + \alpha_{x,t}cos\gamma sin\beta & \alpha_{z,s}cos\beta cos\gamma - \alpha_{y,s}sin\gamma + \alpha_{x,s}cos\gamma sin\beta \end{pmatrix}$$

$$\begin{pmatrix} \alpha_{x,h}cos\beta - \alpha_{z,h}sin\beta \\ \alpha_{y,h}cos\gamma + \alpha_{z,h}cos\beta sin\gamma + \alpha_{x,h}sin\beta sin\gamma \\ \alpha_{z,h}cos\beta cos\gamma - \alpha_{y,h}sin\gamma + \alpha_{x,h}cos\gamma sin\beta \end{pmatrix}$$

and

$$\Omega^1 = \begin{pmatrix} -\alpha_{x,t}cos\beta - \alpha_{z,t}sin\beta & -\alpha_{x,s}cos\beta - \alpha_{z,s}sin\beta \\ \alpha_{y,t}cos\gamma - \alpha_{z,t}cos\beta sin\gamma - \alpha_{x,t}sin\beta sin\gamma & \alpha_{y,s}cos\gamma - \alpha_{z,s}cos\beta sin\gamma - \alpha_{x,s}sin\beta sin\gamma \\ \alpha_{z,t}cos\beta cos\gamma + \alpha_{y,t}sin\gamma - \alpha_{x,t}cos\gamma sin\beta & \alpha_{z,s}cos\beta cos\gamma + \alpha_{y,s}sin\gamma - \alpha_{x,s}cos\gamma sin\beta \end{pmatrix}$$

$$\begin{pmatrix} -\alpha_{x,h}cos\beta - \alpha_{z,h}sin\beta \\ \alpha_{y,h}cos\gamma - \alpha_{z,h}cos\beta sin\gamma - \alpha_{x,h}sin\beta sin\gamma \\ \alpha_{z,h}cos\beta cos\gamma + \alpha_{y,h}sin\gamma - \alpha_{x,h}cos\gamma sin\beta \end{pmatrix}$$

$$\Omega^0 + \Omega^1 = \begin{pmatrix} -2\alpha_z;_t\, sin\beta & -2\alpha_{z,s}sin\beta & -2\alpha_{z,h}sin\beta \\ 2\alpha_{z,s}cos\beta sin\gamma & 2\alpha_{z,s}cos\beta sin\gamma & 2\alpha_{z,s}cos\beta sin\gamma \\ 2\alpha_{z,s}cos\beta cos\gamma & 2\alpha_{z,s}cos\beta cos\gamma & 2\alpha_{z,s}cos\beta cos\gamma \end{pmatrix} \tag{A.14}$$

Then expressions :

$$tan\gamma = \frac{\omega^0_{\eta,i} + \omega^1_{\eta,i}}{\omega^0_{\zeta,i} + \omega^1_{\zeta,i}} \tag{A.15}$$

$$tan\beta = -\frac{\omega^0_{\xi,i} + \omega^1_{\xi,i}}{\omega^0_{\zeta,i} + \omega^1_{\zeta,i}} cos\gamma \tag{A.16}$$

are valid.

Appendix B

B.1 Detector holder

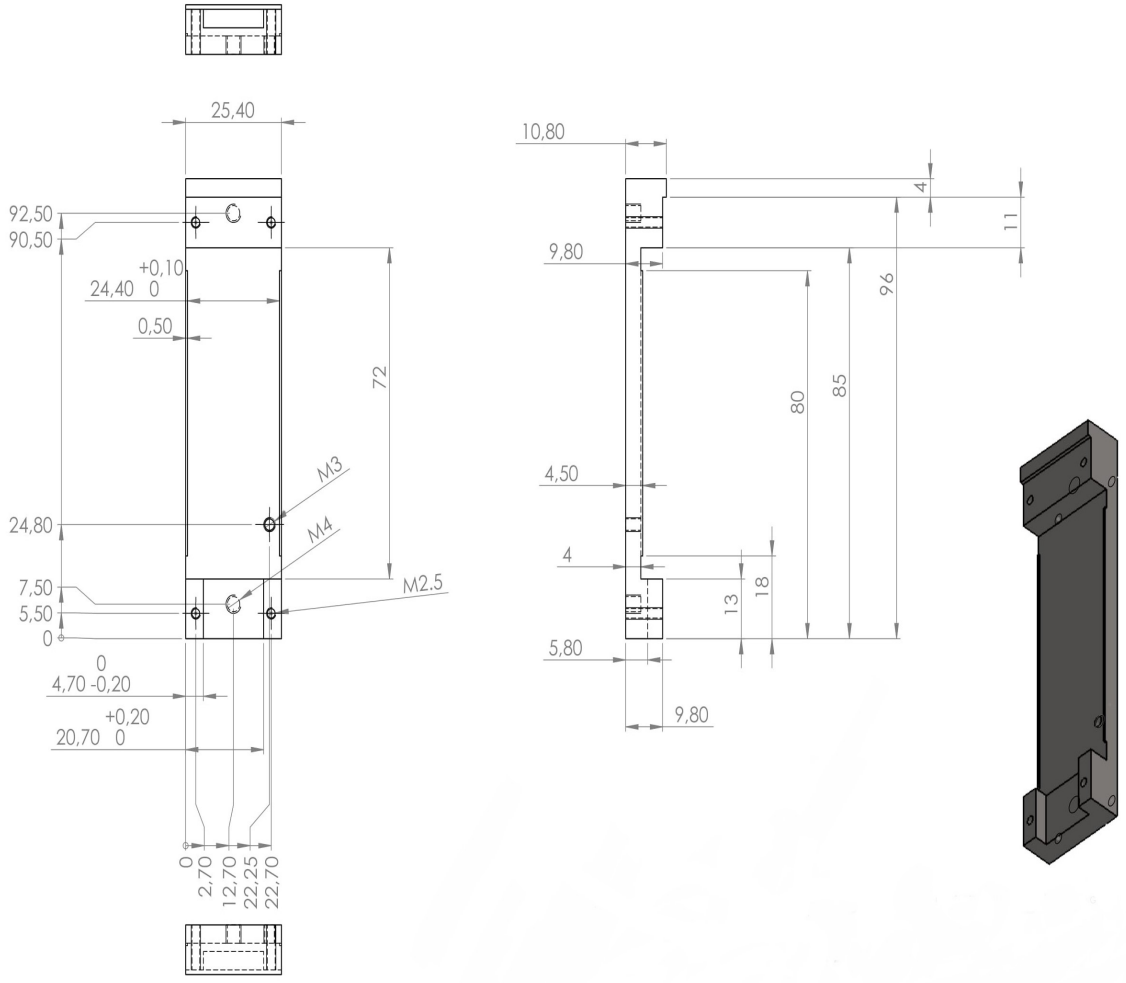

FIGURE B.1: WATCH-CT sensor holder design

B.2 Translation stage

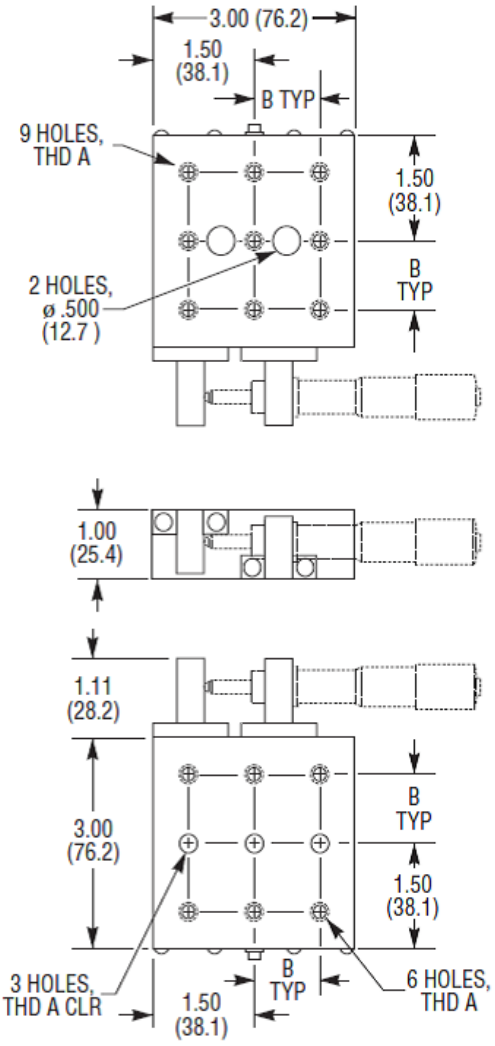

Thread Model (Metric)	A	Dimensions [(mm)] B	C
423	1/4-20 (M6)	1.0 (25.0)	
433	1/4-20 (M6)	1.0 (25.0)	0.50 (13.3)
443	1/4-20 (M6)	1.0 (25.0)	

Newport

FIGURE B.2: Translation stage used for phantom adjustment

B.3 Actuator

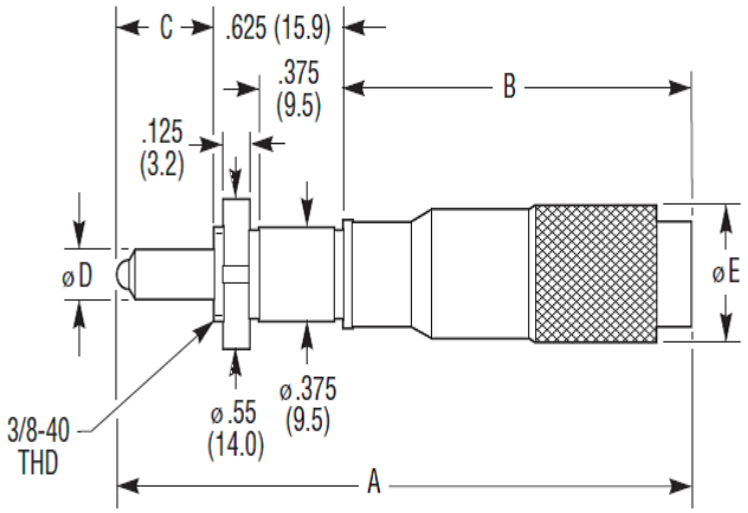

Model	Dimensions [in. (mm)] A	B Min	B Max	C Min	C Max	D	E
SM-13 & SM-13LH	2.36 (59.9)	1.18 (30)	1.69 (43)	0.05 (1.3)	0.56 (14.2)	0.157 (4.0)	0.51 (12.9)
SM-25	3.83 (97.3)	1.98 (50.2)	2.96 (75.2)	0.26 (6.6)	1.23 (31.2)	0.276 (7.0)	0.625 (15.9)
SM-50	5.70 (144.8)	2.95 (74.9)	4.92 (125)	0.157 (4.0)	2.13 (54.1)	0.276 (7.0)	0.625 (15.9)

Newport

FIGURE B.3: Manual actuator used for phantom adjustment

B.4 Defect and Image Quality Specification

TELEDYNE RAD-ICON IMAGING
A Teledyne Technologies Company

Defect and Image Quality Specification (for all Rad-icon sensors)

Basic Definitions:

A **defective pixel** is defined as a pixel whose dark signal, at room temperature (23°C), for a 1000 ms exposure exceeds **3%** of the saturation signal (i.e. ~125 ADU *above offset* for a 12-bit system), or whose light response is **less than 50%** or **greater than 150%** of the average light response of all functional pixels in the sensor.

A **line defect** is defined as any row or column in which **8 or more** contiguous pixels are defective. Adjacent defective lines count as a single defect. The maximum allowable width of any line defect (i.e. the maximum number of adjacent defective lines) depends on the quality grade (see tables). The minimum spacing between line defects is **four** pixels.

A line is also defective if its average value varies by more than **5%** from the local average of the nearest **10** adjacent lines (5 in each direction, excluding known defective lines), as determined by the *Line Check Test*.

A **cluster defect** is defined as any group of **five or more** adjacent (touching in horizontal or vertical direction) defective pixels (excluding line or partial line defects). The maximum allowable size of a cluster defect is **N** pixels wide across its narrowest dimension and **M** pixels along its longest dimension (see tables).

Table1: Image Quality Definitions for RadEye1 and RadEye100 sensors:

Five image quality grades; definitions apply to single sensors only (tiled panels have additional defect allowances):

	G1 (prem.)	G2 (std+)	G3 (std)	G4 (std-)	G5 (eng.)
max. number of line defects	0	3	3	3	10
max. width of line defect	n/a	1	2	3	4
max. number of cluster defects	3	3	4	5	10
max. size of cluster defect	2x7	2x7	3x8	4x10	7x10
max. number of pixel defects	100	200	300	400	500

Note: The number of single pixel defects in a device should be very small («100).

Bibliography

[BNB+03] D. Beque, J. Nuyts, G. Bormans, P. Suetens, and P. Dupont. Characterization of pinhole spect acquisition geometry. *IEEE Transactions on Medical Imaging*, 22(5):599–612, 2003.

[Bro99] A. V. Bronnikov. Virtual alignment of x-ray cone-beam tomography system using two calibration aperture measurements. *Optical Engineering*, page 381–386, 1999.

[Bru11] C. C. Brunner. Development and experimental implementation of a physical concept for quality assurance of new ct methods. *Ph.D. Thesis*, Technical university of Munich, 2011.

[CMSJ05] Y. Cho, Douglas J. Moseley, Jeffrey H. Siewerdsen, and David A. Jaffray. Accurate technique for complete geometric calibration of cone-beam computed tomography systems. *Med. Phys.*, 32(4), 2005.

[Dal] Teledyne Dalsa. Rad-icon imaging corp., radeye1, large area imager user manual.

[Dal16] Teledyne Dalsa. Shadocam imaging library, 2001-2016.

[dH08] Hugo dela Heras. Development and test of a new scanning geometry for computed tomography. 2008.

[DVN08] M. Defrise, C. Vanhove, and J. Nuyts. Characterization of pinhole spect acquisition geometry. *IEEE Transactions on Medical Imaging*, 27(2):204–214, 2008.

[EE03] ELTEC-Elektronik. P3i3 frame grabber family, 2002-2003.

[ESU03] Buhr E., Günther-Kohfahl S., and Neitzel U. Accuracy of a simple method for deriving the pre-sampled mtf of a digital radiographic system from an edge image. *Med. Phys.*, 30:2323–2331, 2003.

[FTT+92] H. Fujita, Y. Tsai, T.Itoh, J. Morishita K.Doi, K. Ueda, and A. Ohtsuka. A simple method for determining the modulation transfer function in digital radiography. *IEEE Trans Med Img.*, 11:34–9, 1992.

[FZ14] Hua Jiang Lei Li Min Guan Bin Yan F. Zhang, Jianping Du. Iterative geometric calibration in circular cone-beam computed tomography. *Optik*, 125:2509–2514, 2014.

[FZW11] JC. Ford, DD. Zheng, and JF. Williamson. Estimation of ct cone-beam geometry using a novel method insensitive to phantom fabrication inaccuracy: Implications for isocenter localization accuracy. *Medical Physics*, 38:2829–2840, 2011.

[GAea03] GEANT4, Agostinelli, and S. et al. Geant4: A simulation toolkit. *Nucl.Instrum.Meth.*, A506:250–303, 2003.

[GTCE87] G. T Gullberg, B. M. W. Tsui, C. R. Crawford, and E. R. Edgerton. Estimation of geometrical parameters for fan beam tomography. *Phys. Med. Biol.*, 32:1581–1594, 1987.

[Hol09] K. M. Holt. Geometric calibration of detectors with discrete irregularities for compute tomography. *Medical Imaging*, 7258, 2009.

[Hsi03] Jiang Hsieh. *Coputed Tomograpy: Principles, Design, Artifacts and Recent Advancement.* SPIE - The International Society for Optical Engineering, Washington USA, 2003.

[IEC03] International Electronical Commission IEC. Medical electrical equipment - characteristics of digital x-ray imaging devices, 2003.

[Ill05] H. Illers. Development of a standardised technique for the measurement of the detective quantum efficiency of digital x-ray imaging systems. *Ph.D. Thesis*, Technical university of Munich, 2005.

[JLG+15] R. Jiang, G. Li, N. Gu, G. Chen, and S. Luo. A wire scanning based method for geometric calibration of high resolution ct system. *Proc.of SPIE*, 9412, 2015.

[JN04] Barrett JF and Keat N. Artifacts in ct: recognition and avoidance. *Pubmed*, 2004.

[KR05] KUKA-Roboter. Software,kr c2 / kr c3,configuration, 2005.

[KS01] Avinash C. Kak and Malcolm Slaney. Principles of computerized tomographic imaging. *SIAM*, page 177–178, 2001.

[KST+13] M. Klaften, A. Schegerer, O. Tischenko, M. Hrabe de Angelis, and C. Hoeschen. A new design for micro-ct scanner. *Spriner*, pages 135–166, 2013.

[KTE+01] M. Karolczak, U. Taubenreuther, K. Engelke, A. Lutz, S. Schaller, and W. A. Kalender. Practical approach to misalignment correction in a single-circle orbit cone-beam tomography. 2001.

[MA09] R. Maini and H. Aggarwal. Study and comparison of various image edge detection techniques. *International Journal of Image Processing (IJIP)*, 3, 2009.

[MCN09] C. Mennessier, R. Clackdoyle, and F. Noo. Direct determination of geometric alignement parameteres for cone-beam scanners. *Phys Med Biol.*, 54(6):1633–1660, 2009.

[MGY13] Y. Meng, Hui Gong, and Xiaoquan Yang. Online geometric calibration of cone-beam computed tomography for arbitrary imaging objects. *IEEE Trans Med Imaging*, 2013.

[NCM+00] F. Noo, R. Clackdoyle, C. Mennessier, T. A. White, and T. J. Roney. Analytic method based on identification of ellipse parameters for scanner calibration in cone-beam tomography. *Phys. Med. Biol.*, 54:489–508, 2000.

[OI19] Oxford-Instruments. Nova 96000 series 90kv water-cooled microfocus x-ray source, technical sheet, 2019.

[PBGM08] D. Panetta, N. Belcari, A. Del. Guerra, and S. Moehrs. An optimization-based method for geometrical calibration in cone-beam ct without dedicated phantoms. *Phys. Med. Biol.*, 53:3841, 2008.

[SHZH06] Yi Sun, Ying Hou, Fengyong Zhao, and Jiasheng Hu. A calibration method for misaligned scanner geometry in cone-beam computed tomography. *Elsevier*, 39:499–513, 2006.

[SkKM+18] N. Saeidnezhad, k. Kumar, B H. Mueller, O. Tischenko, and C. Hoeschen. Assessment of image quality parameters of a novel micro-ct system compared to a conventional ct geometry. *SPIE Medical Imaging*, 2018.

[TnH17] O. Tischenko, N. Saeid nezhad, and C. Hoeschen. Novel method to calibrate ct scanners with a conic probe body. *Proc. of SPIE*, 10132, 2017.

[TNH19] Oleg Tischenko, Nazila Saeid Nezhad, and Christoph Hoeschen. A method of determining geometry of cone beam ct scanner. *Biomedical Physics Engineering Express*, 2019.

[TSXH10] O. Tischenko, A. Schegerer, Y. Xu, and C. Hoeschen. Properties of a parameterization of radon projection by the reconstruction on circular disk. *Proc.of SPIE*, 7622, 2010.

[Wik19] Contributors Wikipedia. *CT scan*. Wikipedia, The Free Encyclopedia, 2019.

[XTH07a] Y. Xu, O. Tischenko, and C. Hoeschen. Approximation and reconstruction from attenuated radon projections. *SIAM*, (45):108–132, 2007.

[XTH07b] Y. Xu, O. Tischenko, and C. Hoeschen. Image reconstruction by oped algorithm with averaging. *Numerical Algorithms*, 45:179–193, 2007.

[YKMB06] K. Yang, A. L. C. Kwan, D. F. Miller, and J. M. Boone. A geometric calibration method for cone beam ct systems. *Med Phys.*, 33(6):1695–1706, 2006.

[ZHZH15] J. Zhao, Xiaodong Hu, Jing Zo, and Xiaotang Hu. Geometric parameters estimation and calibration in cone-beam micro-ct. *Sensors*, 15:22811–22825, 2015.